A multi-physics, multi-scale and finite strain crystal plasticity-based model for pseudoelastic NiTi shape memory alloy

Xiaofei Ju, Ziad Moumni, Yahui Zhang, Fengguo Zhang, Jihong Zhu, Zhe Chen, Weihong Zhang

A multi-physics, multi-scale and finite strain crystal plasticity-based model for pseudoelastic NiTi shape memory alloy.

Xiaofei Ju[a], Ziad Moumni[a,b,*], Yahui Zhang[b,*], Fengguo Zhang[c], Jihong Zhu[b], Zhe Chen[c], Weihong Zhang[b]

[a] *IMSIA, CNRS, EDF,CEA,ENSTA-Paris Institut Polytechnique de Paris, 91120 Palaiseau, France*
[b] *State IJR Center of Aerospace Design and Additive Manufacturing, Northwestern Polytechnical University, 710072 Xi'an, China*
[c] *School of Materials Science and Engineering, Shanghai Jiao Tong University, Shanghai, 200240, PR China*

Abstract

A crystal plasticity-based constitutive model is developed to describe the thermomechanical behavior of pseudoelastic NiTi single crystal. The model includes, for the first time in the literature, all inelastic mechanisms influencing the fatigue behavior of NiTi SMAs in a finite strain framework: martensite transformation, deformation slip in austenite at high-temperature, deformation twinning in martensite at large strain, transformation-induced plasticity (TRIP) as well as thermomechanical coupling. Furthermore, new internal variables and evolution laws are introduced in the monocycle model (referred as basic model in the remainder of the paper) to reproduce the main features of anisotropic cyclic deformation of pseudoelastic NiTi single crystal. The numerical implementation of the constitutive model is performed in the CAST3M (2019) finite element software through a user-defined UMAT subroutine. A series of simulations were performed to verify the basic and generalized cyclic models under various conditions. Moreover, the robustness of the model is attested by comparing the simulation results with the reported data of the pseudoelastic NiTi single crystal. The effect of crystallographic orientation and anisotropic cyclic deformation behavior are revealed and shown to be quantitatively in a good agreement with experimental results. Finally, the evolution of dislocation density and stored energy is discussed from the perspective of fatigue analysis of SMAs.

Key words: NiTi SMA, finite strain, pseudoelasticity, crystal plasticity, twinning, TRIP,

thermomechanical coupling, cyclic deformation

1. Introduction

Pseudoelastic shape memory alloys (SMAs) have the ability of accommodating large recoverable inelastic strains due to the occurrence of a stress induced solid-solid martensitic phase transformation (Auricchio et al., 2007). Owing to this specific property, SMAs, especially NiTi based SMAs, become promising materials in a wide range of industrial fields (Jani et al., 2014). In many of these applications, NiTi SMAs are often subjected to large cyclic deformations (Petrini and Bertini, 2020; Petrini and Migliavacca, 2011). Accordingly, a thorough study of their cyclic behaviour is the basis for a further fatigue analysis necessary for a material and structural optimization of SMAs' components.

From experimental point of view, lots of effort has been deployed in investigating the cyclic deformation behavior of pseudoelastic NiTi SMAs considering single crystals (Gall and Maier, 2002; Sehitoglu et al., 2001b) and polycrystallines (Brinson et al., 2004; Delville et al., 2011; Kang et al., 2009; Miyazaki et al., 1986; Morin et al., 2011; Wang et al., 2008a; Zhang et al., 2017, 2019b; Zheng et al., 2017). The main characteristics of the cyclic response of pseudoelastic NiTi SMAs are: (1) accumulation of the residual strain, (2) drop of the transformation start stress, (3) increase of the transformation hardening, (4) decrease of the hysteresis loop area, (5) dependence on the loading rate. The increment of the residual strain mainly originates from two sources: plastic deformation and residual martensite (Kan and Kang, 2010). Plastic deformation is attributed to the slip in austenite at high temperature (Chowdhury and Sehitoglu, 2017; Shaw and Kyriakides, 1995), deformation twinning in martensite at large strain (McKelvey and Ritchie, 2000; Wang et al., 2008a) and Transformation induced plasticity (TRIP) at A-M (Austenite-Martensite) interfaces (Norfleet et al., 2009; Paranjape et al., 2017). TRIP is a key mechanism in the fatigue issue of SMAs and will be discussed in the next section. The accumulation of inelastic deformation induces internal

*Corresponding author.
Email addresses: ziad.moumni@ensta-paris.fr (Ziad Moumni), zhang.yahui@nwpu.edu.cn (Yahui Zhang)

stresses, which assists the martensite transformation resulting in a drop of the transformation start stress (Xiao et al., 2018; Zaki and Moumni, 2007). Moreover, the dislocation density increases due to the inelastic deformation, which "hinders" the martensite formation and makes the transformation slope steeper (Zhang et al., 2016). With the increment of residual strain and transformation hardening, the stress hysteresis loop decreases. Furthermore, the rate dependence of SMAs is attributed to the temperature variation resulting from the mechanical dissipation, phase transformation latent heat and heat exchanges with the surroundings (Van Humbeeck and Delaey, 1981), which affects the phase transformation and impacts the mechanical response of SMAs (Shaw and Kyriakides, 1995). Such strong rate dependence in SMAs, termed as thermomechanical coupling, is an important feature of their cyclic deformation and severely influences the corresponding fatigue behavior (Grabe and Bruhns, 2008; He and Sun, 2010; Morin et al., 2011; Zhang et al., 2017).

From simulation point of view, a vast literature of constitutive phenomenological and micromechanical-based models have been proposed. Most of the phenomenological models (Auricchio et al., 2007; Lagoudas et al., 2012; Petrini and Bertini, 2020; Zaki and Moumni, 2007) are isotropic and are constructed based on macroscopic variables. The lack of physical basis limits their predictive capabilities, especially in the case of thermomechanical response of initially textured SMAs. In order to address this issue, many micromechanical-based constitutive models have been developed. Among them, crystal plasticity-based models are widely used by modeling plasticity in terms of crystallographic slip at grain scale (Roters et al., 2010). In crystal plasticity models, the inelasticity is considered through crystallographic orientation relationships and microstructure information can be also included. As a result, crystal plasticity models provide more physics background for fatigue analysis than phenomenological models do.

The crystal plasticity framework has been modified to incorporate the martensite transformation, reorientation and detwinning of twinned martensite (Gall and Sehitoglu, 1999; Lim and McDowell, 2002; Thamburaja, 2005). Subsequently, in order to describe the plastic deformation at high temperature or at larger imposed strains, dislocation slip in austenite (Manchiraju and Anderson, 2010; Yu et al., 2012) or both slip and deformation twinning in

martensite (Wang et al., 2008b) are incorporated in the constitutive models. More recently, Dhala et al. (2019); Yu et al. (2014a) extended the model by considering phase transformation and plasticity triggered in both austenite slip and martensite twinning. Furthermore, TRIP is introduced into the models through friction slip systems at A-M interfaces (Xiao et al., 2018; Yu et al., 2014c) or slip systems in austenite matrix (Yu et al., 2015a).

A summary of micromechanical constitutive models considering the deformation behavior of pseudoelastic NiTi SMAs is listed in Table 1. This summary reveals that the majority of the micromechancial models are based on small strain theory rather than finite strain theory. Despite the fact that devices may be subjected to large deformations in practical applications, the cyclic behavior of pseudoelastic NiTi under large strain (Wang et al., 2008a) is not reproduced in these papers. To date, a micromechanical model considering martensite transformation, deformation slip in austenite at high temperature, deformation twinning in martensite at large strain, TRIP accompanied with phase transformation, thermomechanical coupling effect and cyclic loading in the framework of finite deformation theory has not been reported in literature.

Accordingly, in this work, a three-dimensional thermomechanically coupled and crystal plasticity-based constitutive model is constructed to describe the anisotropic cyclic response of pseudoelastic NiTi single crystal under various loading conditions. For the first time in the literature, all the aforementioned mechanisms influencing the fatigue behavior of NiTi SMAs are considered comprehensively in the present model. For clarity, a single crystal based model considering monocyclic deformation will be first constructed (referred as basic model in the remainder of the paper) and then extended to cyclic loading conditions by introducing new internal variables and evolution laws.

It is worth noting that the present paper is a first step towards a multi-scale fatigue analysis of NiTi SMAs from simulation point of view. To this end, a brief introduction to the fatigue phenomena in SMAs and its link with the present model is given below.

Experimental-based fatigue criteria based on macro-scale parameters have been proposed for fatigue analysis of SMAs (Maletta et al., 2012; Moumni et al., 2005; Song et al., 2015). However, these criteria are empirically obtained from mechanical responses and are unable

to predict the thermomechanical coupling effect on the fatigue of SMAs components. Hence, a multi-scale and multiphysics analysis, addressing the intrinsic physical mechanisms related with fatigue, is worthwhile. Based on the experimental works at micro-scale or meso-scale, the importance of cyclic plastic deformation, cyclic phase transformation and their interaction with the microstructural damage has been revealed (Gloanec et al., 2013; Kato and Sasaki, 2013; Mao et al., 2010; Niendorf et al., 2011; Polatidis et al., 2015; Rahim et al., 2013; Sedmák et al., 2015). However, the accumulated slip, microstructure-sensitive stress and dislocation density are necessary but not sufficient to drive crack nucleation (Chen et al., 2018). To this end, Zhang et al. (2016) considered the stored energy in the analysis of fatigue in SMAs. During cyclic loading, part of the hysteresis work is dissipated into heat, while the remainder is stored in the materials and remains after the removal of external loads, namely the stored energy (Hodowany et al., 2000). This elastic stored energy is associated with the strain field of the generated dislocations which modifies the internal energy and causes microstructural changes, such as defects (Borbély et al., 2000). It links with fatigue issue at microscale and is often used as an indicator for fatigue in elastoplastic materials (Wan et al., 2014; Warren and Wei, 2010). The situation is more complicated in the fatigue issue of SMAs since the fatigue lifetime is not directly controlled by dissipated energy at the stabilized cycles due to the thermomechanical coupling effect (Zhang et al., 2019b). In other words, the dissipated energy-based criterion fails for SMAs when loading rates change and a more relevant fatigue indicator, eg. stored energy, is required. However, in the domain of SMAs, the stored energy is not yet widely considered in the fatigue analysis, except the theoretical work of Zhang et al. (2016, 2019c). To this end, the evolution of dislocation density and corresponding stored energy is discussed in relation with the present cyclic model for further future fatigue analysis of SMAs.

The paper is organized as follows. Section 2 presents the theoretical derivations of the constitutive models. Section 3 is dedicated to the numerical implementation of the models. Section 4 introduces the identification procedure of their material parameters. Section 5 and Section 6 give the numerical simulations and validations of both basic and generalized cyclic models, respectively. Section 7 draws the conclusions and prospects.

Table 1

Summary of micromechanical constitutive models.

Models	Features						
	Finite strain theory	A	B	C	D	E	F
Thamburaja and Anand (2001)	✓	✓					
Lim and McDowell (2002)		✓				✓	
Anand and Gurtin (2003)	✓	✓				✓	
Thamburaja (2005)	✓	✓					
Wang et al. (2008b)		✓		✓			
Manchiraju and Anderson (2010)	✓	✓	✓				
Richards et al. (2013)		✓	✓				✓
Mirzaeifar et al. (2013)		✓				✓	
Yu et al. (2013, 2015c)		✓			✓		✓
Yu et al. (2014a)		✓	✓	✓			✓
Yu et al. (2014b)		✓			✓		✓
Yu et al. (2014c)		✓			✓	✓	✓
Yu et al. (2015a)		✓	✓		✓		✓
Paranjape et al. (2016)	✓	✓	✓				
Xiao et al. (2018)		✓			✓	✓	✓
Paranjape et al. (2018)	✓	✓					
Yu et al. (2018)		✓				✓	
Dhala et al. (2019)	✓	✓	✓	✓			
Xie et al. (2019)		✓	✓		✓		✓
Xie et al. (2020)		✓	✓		✓	✓	✓
Ebrahimi et al. (2020)		✓			✓		✓
Hossain and Baxevanis (2021)	✓	✓	✓		✓	✓	
Xu et al. (2021)		✓	✓	✓	✓	✓	✓
Present work	✓	✓	✓	✓	✓	✓	✓

Notes: A: phase transformation; B: deformation slip in austenite; C: deformation twinning in martensite; D: TRIP; E: thermomechanical coupling effect; F: cyclic loading (cycling up to the shakedown (stabilized) state).

2. Constitutive model

In this section, a crystal plasticity-based constitutive model considering the major underlying physical mechanisms is firstly developed for pseudoelastic NiTi, referred as the basic model. Then modifications are introduced to the basic model in order to predict the cyclic deformation behavior. The extended model is referred as generalized cyclic model. In the

present work, a single crystal of NiTi SMA is taken as a representative volume element (RVE) and the inelastic deformation is defined as an average over the RVE.

2.1. Kinematics

The local decomposition of the deformation gradient $\boldsymbol{F}$ is multiplicatively decomposed into elastic part $\boldsymbol{F}_e$ and inelastic part $\boldsymbol{F}_{inel}$.

$$\boldsymbol{F} = \boldsymbol{F}_e \boldsymbol{F}_{inel} \tag{1}$$

Using polar decomposition, the elastic part of the deformation gradient $\boldsymbol{F}_e$ is given as $\boldsymbol{F}_e = \boldsymbol{R}_e \boldsymbol{U}_e$. Accordingly, the elastic Green strain is expressed as $\boldsymbol{E}_e = \frac{1}{2}(\boldsymbol{U}_e{}^2 - \boldsymbol{I})$.

The effective anisotropic elastic moduli $\mathbb{C}(t)$ is defined by the rule of mixture approach:

$$\mathbb{C} = (1-\xi)\mathbb{C}_A + \xi\mathbb{C}_M, \qquad \xi = \sum_{i=1}^{24} \xi^{(i)} \quad (\xi^{(i)} \in [0,1] \quad \text{and} \quad \xi \in [0,1]) \tag{2}$$

Where $\mathbb{C}_A$ and $\mathbb{C}_M$ are anisotropic elastic moduli of austenite and marteniste phases, respectively. From the crystallography point of view, different theories have been developed to account for the martensite phase transformation such as the phenomenological theory of martensite transformation, the Lattice deformation theory and the energy minimization theory (Matsumoto et al., 1987; Sehitoglu et al., 2000). In the present work, 24 different martensite correspondence variant pairs (CVPs) are adopted by selecting <011> Type II twin as the invariant shear mode as suggested by a variety of researchers (Dhala et al., 2019; Manchiraju and Anderson, 2010; Thamburaja and Anand, 2001). A CVP is a formal term for a martensite plate containing two twin-related martensite variants. Each CVP is described by a unique transformation direction $\boldsymbol{b}_0{}^{(i)}$ and a habit plane normal $\boldsymbol{d}_0{}^{(i)}$, referred as a transformation system. ξ is the total martensite volume fraction, which is the sum of volume fractions of all the transformation systems.

Using Hooke's law, the second Piola-Kirchoff stress $\boldsymbol{T}$ is written as $\boldsymbol{T} = \mathbb{C} : \boldsymbol{E}_e$. Thus, the Cauchy stress $\boldsymbol{\sigma}$ is given in function of $\boldsymbol{T}$ by:

$$\boldsymbol{\sigma} = \frac{1}{det(\boldsymbol{F}_e)} \boldsymbol{F}_e \boldsymbol{T} \boldsymbol{F}_e^T \tag{3}$$

The velocity gradient $\boldsymbol{L}$ is defined as $\boldsymbol{L} = \dot{\boldsymbol{F}}\boldsymbol{F}^{-1}$ and can be decomposed as:

$$\boldsymbol{L} = \dot{\boldsymbol{F}}_e\boldsymbol{F}_e{}^{-1} + \boldsymbol{F}_e(\dot{\boldsymbol{F}}_{inel}\boldsymbol{F}_{inel}{}^{-1})\boldsymbol{F}_e{}^{-1} = \boldsymbol{L}_e + \boldsymbol{F}_e\boldsymbol{L}_{inel}\boldsymbol{F}_e{}^{-1} \tag{4}$$

where $\boldsymbol{L}_e$ and $\boldsymbol{L}_{inel}$ are elastic and inelastic part of the velocity gradient, respectively. In the present work, $\boldsymbol{L}_{inel}$ is approximated by the summation of contributions from the following mechanisms: (1) plasticity in austenite due to dislocation slip, (2) martensite transformation, (3) TRIP due to the local high stress at A-M interfaces, (4) plasticity in martensite due to deformation twinning.

$$\boldsymbol{L}_{inel} \approx \boldsymbol{L}_p^A + \boldsymbol{L}_{tr} + \boldsymbol{L}_{trip} + \boldsymbol{L}_p^M \tag{5}$$

These contributions to the inelastic velocity gradient are described as follows.

2.1.1. Plastic deformation

The plastic deformation in the present model includes three parts: deformation slip in austenite, deformation twinning in martensite and TRIP due to phase transformation.

(1) Plasticity in austenite

The plastic deformation in austenite phase is due to the accumulation of slip effect in all activated slip systems. As reported in the literature (Chumlyakov et al., 1996; Ezaz et al., 2013; Norfleet et al., 2009), three potential slip modes of $\{1\ 1\ 0\}\langle 1\ 0\ 0\rangle$, $\{0\ 1\ 0\}\langle 1\ 0\ 0\rangle$ and $\{1\ 1\ 0\}\langle 1\ 1\ 1\rangle$ containing 24 slip systems are considered in the present model. It must be emphasized that different from face centered cubic (fcc) and hexagonal packed crystal (hcp) metals, SMAs with ordered body centered cubic (bcc) in austenite phase exhibit non-Schmid behavior (Alkan and Sehitoglu, 2017; Alkan et al., 2018). As a result, a modified Schmid factor and a generalized yield crtierion has been proposed for NiTi (Alkan and Sehitoglu, 2017; Alkan et al., 2017). It is true that the generalized yield criterion considering the non-Schmid behavior may provide a more accurate prediction of plastic yielding in B2 NiTi. However, in the present work, the yield criterion based on Schmid law has been adopted following the majority of studies of SMAs in the framework of the continuum theory (Dhala et al., 2019; Hossain and Baxevanis, 2021; Manchiraju and Anderson, 2010;

Paranjape et al., 2016; Xiao et al., 2018; Yu et al., 2014a, 2015a), in order to avoid the complexity of considering each independent component of the applied deviatoric stress tensor in the generalized yield criterion.

$$\boldsymbol{L}_p^A = (1-\xi)\sum_{\alpha=1}^{24}\dot{\gamma}_A^{(\alpha)}\boldsymbol{S}_p{}^{(\alpha)}, \qquad \text{where } \boldsymbol{S}_p{}^{(\alpha)} = \boldsymbol{m}_0{}^{(\alpha)} \otimes \boldsymbol{n}_0{}^{(\alpha)} \tag{6}$$

$(1-\xi)$ represents the volume fraction of austenite. $\boldsymbol{S}_p{}^{(\alpha)}$ is the orientation tensor of a unit slip system (α), $\boldsymbol{m}_0{}^{(\alpha)}$ and $\boldsymbol{n}_0{}^{(\alpha)}$ are the Burgers vector and normal vector to the slip plane and $\dot{\gamma}_A^{(\alpha)}$ is the slip rate of each austenite system.

(2) Plasticity in martensite

As reported by Miyazaki et al. (1981) and Karaman et al. (2005), when the applied stress is high enough, plasticity is triggered in martensite phase after complete martensite transformation. In order to analyze the plastic deformation in martensite under the framework of crystal plasticity theory, five independent slip systems are needed to be activated to accommodate a certain strain increment according to Taylor's criterion (Hosford, 1993). However, the symmetry of martensite phase in NiTi is low and only one slip system is assumed to be possible (Kudoh et al., 1985). Such low number of easy slip systems tends to promote deformation by twinning, which is observed by Nishida et al. (1998). As a result, Wang et al. (2008b) incorporated 11 twinning systems (listed by Otsuka and Ren (2005)) and one slip system in martensite. Based on their work, an approximation is made here by following the approach of (Dhala et al., 2019; Yu et al., 2014a) and only the twinning component is taken into consideration. Accordingly, the inelastic part of velocity gradient in martensite phase is then given as:

$$\boldsymbol{L}_p^M = \xi\sum_{t=1}^{11}\dot{\gamma}_{tw}^{(t)}\boldsymbol{S}_{tw}{}^{(t)}, \qquad \text{where } \boldsymbol{S}_{tw}{}^{(t)} = \boldsymbol{b}_0^{tw(t)} \otimes \boldsymbol{d}_0^{tw(t)} \tag{7}$$

$\boldsymbol{S}_{tw}{}^{(t)}$ is the orientation tensor relative to a unit twinning system (t), $\boldsymbol{b}_0^{tw(t)}$ and $\boldsymbol{d}_0^{tw(t)}$ are the unit vectors of twinning direction and normal vector to the habit plane, respectively (Yu et al., 2014a) and $\dot{\gamma}_{tw}^{(t)}$ is the shear rate of twinning system (t) and is expressed as:

$$\dot{\gamma}_{tw}^{(t)} = \gamma_T^{(t)}\dot{\xi}_{tw}^{(t)} \tag{8}$$

where $\gamma_T^{(t)}$ and $\xi_{tw}^{(t)}$ are the constant twinning shear and volume fraction of the $(t)th$ twinning system, respectively.

(3) Transformation Induced Plasticity (TRIP)

For SMAs, plastic slip accumulation occurs at an applied stress level far lower than the yield stresses of the individual phases. High dislocation density is observed near the interfaces even for thermal cyclic loaded SMAs (Kajiwara and Kikuchi, 1982; Kajiware and Owen, 1973; Pelton, 2011; Pelton et al., 2012). Based on the observation of alignment of the slip system emanating from A-M interface and martensite twinning system (Norfleet et al., 2009; Simon et al., 2010), works have been done to explain the TRIP through the investigation of twin boundary (TB) evolution within a framework of atomistic simulations (Mohammed and Sehitoglu, 2020b, 2021). According to Mohammed and Sehitoglu (2020a), the irreversible slip is associated with a dislocation reaction occurring in the presence of a barrier to the migration of the TB. While from continuum micromechanical point of view, TRIP is triggered by the higher local stress at the A-M interfaces, which is necessary to accommodate lattice and constitutive match (Heller et al., 2018; Kato and Sasaki, 2013; Zhang et al., 2019b). In summary, TRIP is still an active research area and needs more investigation. In the present work, TRIP is assumed to occur in austenite phase, which is consistent with the TEM observation in the work of Choi et al. (2021). Besides, for simplification, TRIP is assumed to obey the same criterion as plastic deformation in austenite. Thus, the inelastic velocity gradient due to TRIP can be written as:

$$\boldsymbol{L}_{trip} = (1-\xi)\sum_{\alpha=1}^{24}\dot{\gamma}_{trip}^{(\alpha)}\boldsymbol{S}_p{}^{(\alpha)} \tag{9}$$

Similar to $\dot{\gamma}_A^{(\alpha)}$ for deformation slip in austenite, $\dot{\gamma}_{trip}^{(\alpha)}$ is defined as the slip rate due to TRIP on each austenite slip system and its evolution law is discussed later.

2.1.2. Phase transformation

The transformation part of inelastic velocity gradient is given by:

$$\boldsymbol{L}_{tr} = \sum_{i=1}^{24}\dot{\xi}^{(i)}g_{tr}\boldsymbol{S}_{tr}{}^{(i)}, \qquad \text{where } \boldsymbol{S}_{tr}{}^{(i)} = \boldsymbol{b}_0{}^{(i)}\otimes\boldsymbol{d}_0{}^{(i)} \tag{10}$$

$\boldsymbol{S_{tr}}^{(i)}$ is the orientation tensor produced by a unit transformation system (i), $\boldsymbol{b}_0{}^{(i)}$ and $\boldsymbol{d}_0{}^{(i)}$ are the unit vectors of transformation direction and normal vector to the habit plane, respectively (Thamburaja and Anand, 2001) and g_{tr} is the magnitude of shearing deformation caused by the transformation.

2.2. Thermodynamics

2.2.1. Helmholtz free energy density

The Helmholtz free energy per unit reference volume is defined in the reference configuration as:

$$\psi(\boldsymbol{E}_e, \xi^{(i)}, \theta) = \psi_e + \psi_\theta + \psi_{int} + \psi_p + \psi_{trans} + \psi_{cst} \tag{11}$$

where,

$$\psi_e = \frac{1}{2}\boldsymbol{E}_e : \mathbb{C} : \boldsymbol{E}_e \tag{12}$$

$$\psi_\theta = C[(\theta - \theta_0) - \theta \ln \frac{\theta}{\theta_0}] + \mu(\theta - \theta_0)\xi \tag{13}$$

$$\dot{\psi}_{int} = -\boldsymbol{B}_{int} : (\boldsymbol{L}_{tr} + \boldsymbol{L}_{trip}) \tag{14}$$

$$\dot{\psi}_p = (1-\xi)\sum_{\alpha=1}^{24} g_A^{(\alpha)} |\dot{\gamma}_A^{(\alpha)}| + \xi \sum_{t=1}^{11} g_{tw}^{(t)} (\dot{\gamma}_{tw}^{(t)}) \tag{15}$$

$$\psi_{trans} = \frac{1}{2}G\xi^2 + \frac{1}{2}\beta g_{tr}\xi(1-\xi) \tag{16}$$

$$\psi_{cst} = -w_0(1-\xi) - \sum_{i=1}^{N_T} w_i \xi^{(i)} \tag{17}$$

ψ_e is the elastic strain energy.

ψ_θ is the chemical free energy related to phase transformation in which C is the specific heat capacity, μ is the coefficient of entropy difference and θ_0 is the equilibrium transformation temperature expressed as:

$$\theta_0 = \frac{1}{2}(\theta_{AM} + \theta_{MA}) \tag{18}$$

Where θ_{AM} and θ_{MA} are the start temperature of forward and reverse transformation, respectively.

ψ_{int} is the energy associated with the internal stress $\boldsymbol{B}_{int}$. In fact, the slip deformation accumulation leads to residual strain during cyclic deformation of NiTi SMAs (Eggeler et al., 2004; Kang et al., 2009). Such slip deformation induces the internal stress which allows easier transformation from austenite to martensite. To describe this cyclic effect on the transformation stress plateau levels, Zaki and Moumni (2007) introduced an internal stress $\boldsymbol{B}_{int}$ as an internal variable in their phenomenological model. Although the internal stress effect on monocyclic deformation is not significant, it is still taken into consideration in the present work to lay foundation for the subsequent cyclic deformation and further fatigue analysis. Based on the work of Yu et al. (2015c), $\boldsymbol{B}_{int}$ is divided into 24 components and each of them has the the same orientation tensor as that of the corresponding martensite variant:

$$\boldsymbol{B}_{int} = \sum_{i=1}^{24} \boldsymbol{B}_{int}{}^{(i)}, \qquad \boldsymbol{B}_{int}^{(i)} = \| \boldsymbol{B}_{int}^{(i)} \| \boldsymbol{S}_{tr}^{(i)} \tag{19}$$

Where $\| \boldsymbol{B}_{int}^{(i)} \|$ is the norm of $\boldsymbol{B}_{int}^{(i)}$.

ψ_p is referred to the energy of plastic deformation in austenite and martensite phases where $g_A^{(\alpha)}$ and $g_{tw}^{(t)}$ are the resistance of slip and twinning in each system, respectively. It is worthy noting that ψ_{int} and ψ_p are given in their rate form due to their dependence on the deformation history.

ψ_{trans} is the contribution of austenite and martensite interaction where G and β are the material parameters describing the extent of interactions between martensite variants and between austenite and martensite, respectively.

The last term ψ_{cst} is the potential energy due to the internal constraints where w_0 and w_i are Lagrange multipliers associated with these constraints and obeying the following equations (Moumni et al., 2008):

$$w_0 \geq 0, \quad w_0(1-\xi) = 0 \quad \text{and} \quad w_i \geq 0, \quad w_i \xi^{(i)} = 0 \tag{20}$$

2.2.2. Thermodynamic driving forces

In order to define the driving forces associated with the irreversible mechanisms, we appeal to the inequality of Clausius-Duhem:

$$\boldsymbol{P} : \dot{\boldsymbol{F}} - \dot{\psi} - \eta\dot{\theta} - \frac{\boldsymbol{q}\nabla\theta}{\theta} \geq 0 \tag{21}$$

Where η is the specific entropy per unit reference volume, $\boldsymbol{q}$ is the heat flux and $\boldsymbol{P}$ is the first Piola-Kirchoff stress ($\boldsymbol{P} = det(\boldsymbol{F})\boldsymbol{\sigma}\boldsymbol{F}^{-T}$).

Using the relations in Eq. (3) and (4), the first term of Eq. (21) turns to be:

$$\boldsymbol{P} : \dot{\boldsymbol{F}} = \boldsymbol{T} : \dot{\boldsymbol{E}}_e + \boldsymbol{F}_e^T\boldsymbol{F}_e\boldsymbol{T} : \boldsymbol{L}_{inel} \tag{22}$$

Substituting Eq. (5) and (22) into Eq. (21) gives:

$$\begin{aligned}
&(\boldsymbol{T} - \frac{\partial\psi}{\partial\boldsymbol{E}_e}) : \dot{\boldsymbol{E}}_e - (\eta + \frac{\partial\psi}{\partial\theta})\dot{\theta} + \sum_{i=1}^{24}[g_{tr}(\boldsymbol{M} : \boldsymbol{S}_{tr}{}^{(i)}) - \frac{\partial\psi}{\partial\xi^{(i)}}]\dot{\xi}^{(i)} \\
&+ (1-\xi)\sum_{\alpha=1}^{24}[(\boldsymbol{M} : \boldsymbol{S}_p{}^{(\alpha)})\dot{\gamma}_A^{(\alpha)} - g_A^{(\alpha)}|\dot{\gamma}_A^{(\alpha)}|] + \xi\sum_{t=1}^{11}(\boldsymbol{M} : \boldsymbol{S}_{tw}{}^{(t)} - g_{tw}^{(t)})\dot{\gamma}_{tw}^{(t)} \\
&+ (1-\xi)\sum_{\alpha=1}^{24}[(\boldsymbol{M} + \boldsymbol{B}_{int}) : \boldsymbol{S}_p{}^{(\alpha)}]\dot{\gamma}_{trip}^{(\alpha)} - \frac{\boldsymbol{q}\nabla\theta}{\theta} \geq 0
\end{aligned} \tag{23}$$

Where $\boldsymbol{M}$ is the Mandel stress given by: $\boldsymbol{M} = \boldsymbol{F}_e{}^T\boldsymbol{F}_e\boldsymbol{T}$

For arbitrary thermodynamic process, the inequality is guaranteed by the following equations:

$$\boldsymbol{T} = \frac{\partial\psi}{\partial\boldsymbol{E}_e} = \mathbb{C} : \boldsymbol{E}_e \tag{24}$$

$$\eta = -\frac{\partial\psi}{\partial\theta} = C\ln\frac{\theta}{\theta_0} - \mu\sum_{i=1}^{24}\xi^{(i)} \tag{25}$$

and by following inequations which ensure the non-negative intrinsic dissipation in arbitrary

evolutions:

$$\sum_{i=1}^{24}[g_{tr}(\boldsymbol{M}+\boldsymbol{B}_{int}):\boldsymbol{S}_{tr}{}^{(i)}-\frac{\partial\psi}{\partial\xi^{(i)}}]\dot{\xi}^{(i)}\geq 0 \tag{26}$$

$$((1-\xi)\sum_{\alpha=1}^{24}[(\boldsymbol{M}:\boldsymbol{S}_{p}{}^{(\alpha)})\dot{\gamma}_{A}^{(\alpha)}-g_{A}^{(\alpha)}|\dot{\gamma}_{A}^{(\alpha)}|]\geq 0 \tag{27}$$

$$\xi\sum_{t=1}^{11}(\boldsymbol{M}:\boldsymbol{S}_{tw}{}^{(t)}-g_{tw}^{(t)})\dot{\gamma}_{tw}^{(t)}\geq 0 \tag{28}$$

$$(1-\xi)\sum_{\alpha=1}^{24}[(\boldsymbol{M}+\boldsymbol{B}_{int}):\boldsymbol{S}_{p}{}^{(\alpha)}]\dot{\gamma}_{trip}^{(\alpha)}\geq 0 \tag{29}$$

$$-\frac{\boldsymbol{q}\nabla\theta}{\theta}\geq 0 \tag{30}$$

Assuming that the dissipation for each transformation system is non-negative, then Eq. (26) can be written as:

$$[g_{tr}(\boldsymbol{M}+\boldsymbol{B}_{int}):\boldsymbol{S}_{tr}{}^{(i)}-\frac{\partial\psi}{\partial\xi^{(i)}}]\dot{\xi}^{(i)}\geq 0 \tag{31}$$

The conjugate term of $\dot{\xi}^{(i)}$ in Eq. (31) is the driving force for transformation and is given by:

$$f_{tr}^{(i)}=g_{tr}(\boldsymbol{M}+\boldsymbol{B}_{int}):\boldsymbol{S}_{tr}{}^{(i)}-\frac{1}{2}\boldsymbol{E}_{e}:\Delta\mathbb{C}:\boldsymbol{E}_{e}-\mu(\theta-\theta_{0})-G\xi-\frac{1}{2}\beta g_{tr}(1-2\xi)+w_{0}-w_{i} \tag{32}$$

$\Delta\mathbb{C}=\mathbb{C}_{M}-\mathbb{C}_{A}$ is the difference of elastic tensors of martensite and austenite.

Assuming that $\text{sign}(\dot{\gamma}_{A}^{(\alpha)})=\text{sign}(\boldsymbol{M}:\boldsymbol{S}_{p}{}^{(\alpha)})$ and the dissipation for each slip system is non-negative, then Eq. (27) can be written as:

$$((1-\xi)(|\boldsymbol{M}:\boldsymbol{S}_{p}{}^{(\alpha)}|-g_{A}^{(\alpha)})\dot{\gamma}_{A}^{(\alpha)}\text{sign}(\boldsymbol{M}:\boldsymbol{S}_{p}{}^{(\alpha)})\geq 0 \tag{33}$$

The conjugate term of $\dot{\gamma}_{A}^{(\alpha)}\text{sign}(\boldsymbol{M}:\boldsymbol{S}_{p}{}^{(\alpha)})$ in Eq. (33) is the driving force for slip in austenite and is given by:

$$f_{A}^{(\alpha)}=|\boldsymbol{M}:\boldsymbol{S}_{p}{}^{(\alpha)}|-g_{A}^{(\alpha)} \tag{34}$$

Assuming the dissipation for each twinning system is non-negative, the conjugate term of $\dot{\gamma}_{tw}^{(t)}$ in Eq. (28) is the driving force for twinning in martensite, given as:

$$f_{tw}^{(t)}=(\boldsymbol{M}:\boldsymbol{S}_{tw}{}^{(t)})-g_{tw}^{(t)} \tag{35}$$

Similarly, the conjugate term of $\dot{\gamma}_{trip}^{(\alpha)}$ in Eq. (29) is the driving force for TRIP, written as:

$$f_{trip}^{(\alpha)} = (\boldsymbol{M} + \boldsymbol{B}_{int}) : \boldsymbol{S}_p{}^{(\alpha)} \tag{36}$$

The term in the left side of the Eq. (30) is the thermal dissipation.

Recall the Fourier's law: $\boldsymbol{q} = -\boldsymbol{k} \cdot \nabla\theta$. Since $\boldsymbol{k}$ is positive defined heat conductivity tensor, the thermal dissipation is non-negative.

2.2.3. Thermomechanical coupling

As commented in the introduction, thermomechanical coupling is a key feature of pseudoelastic SMAs's behavior and cannot be neglected. Thus, in this paragraph, thermomechanical coupling is taken into account in the monocyclic deformation by considering two main heat sources, the intrinsic mechanical dissipation and the latent heat, as follows.

The first law of thermodynamics is given by:

$$\dot{\boldsymbol{U}} = \boldsymbol{P} : \dot{\boldsymbol{F}} - \nabla \cdot \boldsymbol{q} \tag{37}$$

Where $\boldsymbol{U}$ is the internal energy per unit reference volume.

Considering the definition of Helmholtz free energy ($\boldsymbol{\psi} = \boldsymbol{U} - \theta\eta$), Eq. (37) can be rewritten as:

$$\theta\dot{\eta} = \boldsymbol{P} : \dot{\boldsymbol{F}} - \dot{\psi} - \dot{\theta}\eta - \nabla \cdot \boldsymbol{q} \tag{38}$$

Considering the dissipative inequality (Eq. 21) and expression of driving forces for each mechanism (Eqs. 32-36), one gets:

$$\theta\dot{\eta} = \sum_{i=1}^{24} f_{tr}^{(i)}\dot{\xi}^{(i)} + (1-\xi)\sum_{\alpha=1}^{24} f_A^{(\alpha)}\dot{\gamma}_A^{(\alpha)} + \xi\sum_{t=1}^{11} f_{tw}^{(t)}\dot{\gamma}_{tw}^{(t)} + (1-\xi)\sum_{\alpha=1}^{24} f_{trip}^{(\alpha)}\dot{\gamma}_{trip}^{(\alpha)} - \nabla \cdot \boldsymbol{q} \tag{39}$$

Substituting Eq. (25) into (39), yields the heat equilibrium equation:

$$\begin{aligned} C\dot{\theta} + \nabla \cdot \boldsymbol{q} = & \underbrace{\sum_{i=1}^{24} f_{tr}^{(i)}\dot{\xi}^{(i)} + (1-\xi)\sum_{\alpha=1}^{24} f_A^{(\alpha)}\dot{\gamma}_A^{(\alpha)} + \xi\sum_{t=1}^{11} f_{tw}^{(t)}\dot{\gamma}_{tw}^{(t)} + (1-\xi)\sum_{\alpha=1}^{24} f_{trip}^{(\alpha)}\dot{\gamma}_{trip}^{(\alpha)}}_{Mechanical\ dissipation} \\ & \underbrace{+ \theta\mu\sum_{i=1}^{24}\dot{\xi}^{(i)}}_{Latent\ heat} \end{aligned} \tag{40}$$

The first four terms in the right side of the Eq. (40) are the mechanical dissipation caused by the phase transformation, slip in austenite, twinning in martensite and TRIP due the high local stress at A-M interfaces. The last term is the transformation latent heat associated with the volume fraction of martensite.

2.3. Flow rules

2.3.1. Evolution of deformation slip in austenite

The evolution of plastic slip in austenite is given by a rate-dependent power law based on the work of Peirce et al. (1982):

$$\dot{\gamma}_A^{(\alpha)} = \dot{\gamma}_A^0 \left| \frac{\tau_A^{(\alpha)}}{g_A^{(\alpha)}} \right|^{\frac{1}{m_A}} \mathrm{sign}(\tau_A^{(\alpha)}), \qquad \text{and } \tau_A^{(\alpha)} = \boldsymbol{M} : \boldsymbol{S}_p{}^{(\alpha)} \tag{41}$$

where $\tau_A^{(\alpha)}$ is the resolved shear stress on slip system (α), $\dot{\gamma}_A^0$ is a reference slip rate and m_A is the rate sensitivity. The slip resistance $g_A^{(\alpha)}$ for each slip system evolves as:

$$\dot{g}_A^{(\alpha)} = \sum_{\beta=1}^{24} h_A^{\alpha\beta} \left| \dot{\gamma}_A^{(\beta)} \right| \tag{42}$$

$$h_A^{\alpha\beta} = h_A^0 \left[q_A + (1 - q_A)\delta^{\alpha\beta} \right] (1 - \frac{g_A^\beta}{g_A^\infty})^{a_A} \mathrm{sign}(1 - \frac{g_A^\beta}{g_A^\infty}) \tag{43}$$

$h_A^{\alpha\beta}$ is the strain hardening matrix. h_A^0, g_A^∞ and a_A are material parameters, representing the initial hardening coefficient, the saturation values of slip resistance and hardening exponent, respectively. The parameter q_A represents the ratio of latent hardening to self-hardening.

2.3.2. Evolution of twinning deformation in martensite

Similarly, a rate-dependent power law is adopted for describing the evolution of the deformation twin (Abdolvand et al., 2011; Kalidindi, 1998; Salem et al., 2005).

$$\dot{\gamma}_{tw}^{(t)} = \begin{cases} \dot{\gamma}_{tw}^0 (\frac{\tau_{tw}^{(t)}}{g_{tw}^{(t)}})^{\frac{1}{m_{tw}}}, & \tau_{tw}^{(t)} > 0 \\ 0, & \tau_{tw}^{(t)} \leq 0 \end{cases}, \qquad \text{and } \tau_{tw}^{(t)} = \boldsymbol{M} : \boldsymbol{S}_{tw}{}^{(t)} \tag{44}$$

Considering the relationship between $\dot{\gamma}_{tw}^{(t)}$ and $\dot{\xi}_{tw}^{(t)}$ (equation (8)), the evolution of deformation twin volume fraction is:

$$\dot{\xi}_{tw}^{(t)} = \begin{cases} \frac{\dot{\gamma}_{tw}^{(t)}}{\gamma_T^{(t)}}, & \tau_{tw}^{(t)} > 0 \\ 0, & \tau_{tw}^{(t)} \leq 0 \end{cases}, \qquad \text{and} \quad \xi_{tw}^{(t)} \geq 0, \qquad \sum_{t=1}^{11} \xi_{tw}^{(t)} \leq 1, \tag{45}$$

Where $\tau_{tw}^{(t)}$ is the resolved shear stress on twinning system (t), $\dot{\gamma}_{tw}^{0}$ is a reference shear rate and m_{tw} is the rate sensitivity for deformaiton twinning. $\gamma_T^{(t)}$ is the magnitude of twinning shear of (t)th twinning system. The twinning resistance $g_{tw}^{(t)}$ for each slip system evolves as:

$$\dot{g}_{tw}^{(t)} = \sum_{s=1}^{11} h_{tw}^{ts} \dot{\gamma}_{tw}^{(s)} \tag{46}$$

$$h_{tw}^{tw} = h_{tw}^{0} \left[q_{tw} + (1 - q_{tw}) \delta^{\alpha\beta} \right] (1 - \frac{g_{tw}^{\beta}}{g_{tw}^{\infty}})^{a_{tw}} \tag{47}$$

Where h_{tw}^{0} is the initial hardening coefficient, g_{tw}^{∞} is the saturation values of twinning resistance, a_{tw} is the hardening exponent and q_{tw} represents the ratio of latent hardening to self-hardening coefficient.

2.3.3. Evolution of TRIP

Since TRIP is introduced by phase transformation, the evolution of slip rate due to TRIP is assumed to be a function of the volume fraction of the product phase $\dot{\xi}^{(i)}$ (Taleb and Sidoroff, 2003; Xiao et al., 2018; Yu et al., 2013). Besides, TRIP is believed to be responsible for the accumulation of residual strain during cyclic deformation of NiTi SMA and the residual strain saturates at the stabilized cycle (shakedown state) (Morin et al., 2011). Consequently, an exponential form is proposed here based on the work of Zaki and Moumni (2007) in order to describe such accumulation and saturation process of irrecoverable strain for the following cyclic deformation study. A variable γ_{sat} is introduced in the evolution expression to represent the maximum plastic deformation resulting from TRIP. b is a time constant and controls the increasing rate of $\dot{\gamma}_{trip}^{(\alpha)}$. When considering the monocyclic deformation, the γ_{sat} is linked with the part of residual strain resulting from TRIP at the end of

unloading and b is equal to one.

$$\dot{\gamma}_{trip}^{(\alpha)} = \begin{cases} \frac{\gamma_{sat}}{b} e^{-\frac{\xi_c}{b}} \left|\dot{\xi}\right|, & f_{trip}^{(\alpha)} > 0 \\ 0, & f_{trip}^{(\alpha)} \leq 0 \end{cases} \tag{48}$$

ξ_c represents the cumulated martensite volume fraction and its evolution is written as:

$$\dot{\xi}_c = \sum_{i=1}^{24} \dot{\xi}_c^{\,(i)}, \qquad \dot{\xi}_c^{\,(i)} = \left|\dot{\xi}^{(i)}\right| \tag{49}$$

According to Eq. (36), the driving force for TRIP is related with the internal stress $\boldsymbol{B}_{int}$. Based on the work of Zaki and Moumni (2007), the evolution of $\boldsymbol{B}_{int}$ is given by:

$$\| \dot{\boldsymbol{B}}_{int}^{(i)} \| = \frac{B_{sat}}{b} e^{-\frac{\xi_c}{b}} \dot{\xi}_c \tag{50}$$

B_{sat} is a variable introduced to represent the saturation value for the internal stress during cyclic deformation. Its value can be obtained from the difference of start stresses for forward transformation of the first and stabilized cycles. For the monocyclic deformation, B_{sat} is related with the maximum value of internal stress in one cycle.

2.3.4. Evolution of transformation deformation

The transformation rate is viewed as sufficiently fast and a rate-independent transformation law is used. The driving force $f_{tr}{}^{(i)}$ for the phase transformation in each system is always bounded by a critical value $f_c{}^{(i)}$: $\left|f_{tr}^{(i)}\right| \leq f_c^{(i)}$. Thus, the transformation criteria are listed below:

$$\mathscr{F}_{AM}^{(i)} = f_{tr}^{(i)} - f_c^{(i)} = 0 \qquad \text{Forward transformation} \tag{51}$$

$$\mathscr{F}_{MA}^{(i)} = f_{tr}^{(i)} + f_c^{(i)} = 0 \qquad \text{Reverse transformation} \tag{52}$$

According to the dissipation inequality Eq. (26), the sign of $\dot{\xi}^{(i)}$ and $f_{tr}^{(i)}$ should be same. Then the phase change kinematics can be derived from relevant consistency conditions:

$$\mathscr{F}_{AM}^{(i)} = 0 \text{ and } \dot{\mathscr{F}}_{AM}^{(i)} = 0 \quad \Rightarrow \quad \dot{\xi} > 0 \quad \text{(forward transformation occurs)} \tag{53}$$

$$\mathscr{F}_{MA}^{(i)} = 0 \text{ and } \dot{\mathscr{F}}_{MA}^{(i)} = 0 \quad \Rightarrow \quad \dot{\xi} < 0 \quad \text{(reverse transformation occurs)} \tag{54}$$

2.4. Generalization to cyclic response

2.4.1. Introduction of new internal variables

The local stress field is redistributed due to the phase transformation, which inhibits the further transformation in the first transformed grain (Brinson et al., 2004). Thus, untransformed austenite (referred as UA) exists in SMAs after full transformation (Brinson et al., 2004; Zhang et al., 2019a). Similarly, the internal stress triggered by the dislocations and transformation incompatibilities will lead to the occurrence of residual martensite (referred as RM) after complete unloading (Kang et al., 2009). Both UA and RM play a key role in the degradation of the recoverable strain during cyclic loading of SMAs, and further influence the fatigue lifetime. Thus, the volume fraction of UA and RM (ξ_{ua} and ξ_{rm}, respectively) are introduced as internal variables in the generalized model.

$$\xi_{ua} = \sum_{i=1}^{24} \xi_{ua}^{(i)}, \qquad \xi_{ua}^{(i)} \in [0,1] \quad \text{and} \quad \xi_{ua} \in [0,1] \tag{55}$$

$$\xi_{rm} = \sum_{i=1}^{24} \xi_{rm}^{(i)}, \qquad \xi_{rm}^{(i)} \in [0,1] \quad \text{and} \quad \xi_{rm} \in [0,1] \tag{56}$$

The martensite volume fraction is limited within the range of $\xi^{(i)} \in [\xi_{rm}^{(i)}, 1-\xi_{ua}^{(i)}]$ and $\xi \in [\xi_{rm}, 1-\xi_{ua}]$. Thus, the potential energy ψ_{cst} due to the internal constraints will be modified as:

$$\psi_{cst} = -w_0(1-\xi_{ua}-\xi) - \sum_{i=1}^{24} w_i(\xi^{(i)} - \xi_{rm}^{(i)}) \tag{57}$$

Where the Lagrange multipliers w_0 and w_i obey the following equations:

$$w_0 \geq 0, \quad w_0(1-\xi_{ua}-\xi) = 0 \quad \text{and} \quad w_i \geq 0, \quad w_i(\xi^{(i)} - \xi_{rm}^{(i)}) = 0 \tag{58}$$

2.4.2. Modified evolution laws

(1) Modified evolution of TRIP induced deformation

Three assumptions are made related to the evolution of TRIP.

Assumption 1: *TRIP triggers once the stress-induced phase transformation occurs.*

Assumption 2: *The sign of $\dot{\gamma}_{trip}^{(\alpha)}$ is consistent with that of the driving force for TRIP.*

According to Staroselsky and Anand (1998), the dislocation slip is bi-directional. Thus, the sign of driving force $f_{trip}^{(\alpha)}$ could be positive or negative. In order to satisfy the thermodynamics compatibility (Eq. 29), the sign of $\dot{\gamma}_{trip}^{(\alpha)}$ is set as same as corresponding $f_{trip}^{(\alpha)}$.

Assumption 3: *TRIP only triggers on the slip systems which have large Schmid factor. $SF_{critical}$ is the critical value to determine the active slip systems for TRIP.*

Accordingly, the slip rate due to TRIP is rewritten as:

$$\dot{\gamma}_{trip}^{(\alpha)} = \frac{\gamma_{sat}}{b_1} e^{-\frac{\xi_c}{b_1}} \left|\dot{\xi}\right| \operatorname{sign}(f_{trip}^{(\alpha)}) \qquad \text{when} \quad SF_{plastic}^{(\alpha)} > SF_{critical} \tag{59}$$

b_1 is a time constant and controls the increasing rate of $\dot{\gamma}_{trip}^{(\alpha)}$.

In order to express the different changing rates of $\gamma_{trip}^{(\alpha)}$ and internal stress $\boldsymbol{B}_{int}$, a distinct time constant b_2 is used in the evolution law of $\boldsymbol{B}_{int}$:

$$\| \dot{\boldsymbol{B}}_{int}^{(i)} \| = \frac{B_{sat}}{b_2} e^{-\frac{\xi_c}{b_2}} \dot{\xi}_c \tag{60}$$

(2) Modified evolution of transformation deformation

As mentioned in Section 2.4.1, UA and RM are related with the internal stress attributed to the phase transformation. Thus, the evolutions of $\xi_{ua}^{(i)}$ and $\xi_{rm}^{(i)}$ are given as a function of the volume fraction of product phase $\dot{\xi}^{(i)}$.

$$\dot{\xi}_{ua}^{(i)} = \frac{\xi_{ua}^{sat}}{b_3} e^{-\frac{\xi_c}{b_3}} \left|\dot{\xi}^{(i)}\right| \tag{61}$$

$$\dot{\xi}_{rm}^{(i)} = \frac{\xi_{rm}^{sat}}{b_4} e^{-\frac{\xi_c}{b_4}} \left|\dot{\xi}^{(i)}\right| \tag{62}$$

Where ξ_{ua}^{sat} and ξ_{rm}^{sat} are the parameters representing the saturation values for volume fraction of UA and RM at stabilized cycles respectively. b_3 and b_4 are the material parameters which control the relevant evolution rate.

During cyclic loading, the slope of transformation plateau will increase and the stress hysteresis will decrease (Delville et al., 2011). In order to capture these two characteristics of SMA's cyclic behavior, the transformation hardening parameter G and critical driving force $f_c^{(i)}$ are set to evolve with the martensite volume fraction $\dot{\xi}^{(i)}$ obeying the following

equations:

$$\dot{f}_c^{(i)} = \frac{(f_{c\_sat}^{(i)} - f_{c\_0}^{(i)})}{b_5} e^{-\frac{\xi_c}{b_5}} \left|\dot{\xi}\right| \tag{63}$$

$$\dot{G} = \frac{(G^{sat} - G^0)}{b_6} e^{-\frac{\xi_c}{b_6}} \left|\dot{\xi}\right| \tag{64}$$

While $f_{c\_0}^{(i)}$ and $f_{c\_sat}^{(i)}$ represent the critical driving force for each transformation system at first and stabilized cycles, respectively. Similarly, G^0 and G^{sat} are used to describe the transformation hardening under cyclic loading. b_5 and b_6 are the constants related with evolution rates.

2.4.3. Dislocation density and corresponding stored energy

It is noted that the aim of our study is the fatigue of NiTi SMAs based on stored energy criterion. As a starting point, the evolution of dislocation density and the corresponding stored energy during cyclic deformation are discussed in this section.

The total dislocation density in the RVE is given as:

$$\rho_{tot} = (1-\xi)\rho_A + \xi \cdot \xi_{tw} \cdot \rho_M, \qquad \rho_A = \sum_{\alpha=1}^{24} \rho_A^{(\alpha)}, \quad and \quad \rho_M = \sum_{t=1}^{11} \rho_M^{(t)} \tag{65}$$

Where ρ_A and ρ_M are the dislocation densities in the austenite and martensite phases, respectively. It should be noted that, ρ_A is the sum of dislocation density of 24 slip systems attributed to both austenite slip at high temperature and TRIP. ρ_M is the sum of dislocation density of 11 twinning systems resulting from the twinning deformation at large strain. The evolution equations of $\rho_A^{(\alpha)}$ and $\rho_M^{(t)}$ are adopted based on the widely used dislocation density evolution law (Lee et al., 2010).

$$\dot{\rho}_A^{(\alpha)} = c_1\left(\sqrt{\sum_{\alpha=1}^{24} \rho_A^{(\alpha)}} - c_2\rho_A^{(\alpha)}\right)\left(|\dot{\gamma}_A^{(\alpha)}| + |\dot{\gamma}_{trip}^{(\alpha)}|\right) \tag{66}$$

$$\dot{\rho}_M^{(t)} = c_3\left(\sqrt{\sum_{t=1}^{11} \rho_M^{(t)}} - c_4\rho_M^{(t)}\right)|\dot{\gamma}_{tw}^{(t)}| \tag{67}$$

c_1, c_3 are the parameters related with dislocation generation while c_2, c_4 are the parameters controlling the annihilation process of dislocation.

According to Borbély et al. (2000), the stored energy E_{st} (per unit volume) can be estimated by the energy of dislocation and E_{st} is given in function of dislocation density ρ_{tot} by (Hazra et al., 2009; Lan et al., 2005):

$$E_{st} \approx \rho_{tot} E_{dis} \approx \frac{1}{2} \rho_{tot} G_{shear} b^2 \tag{68}$$

Where G_{shear} is the shear modulus and b is the magnitude of Burgers vector.

A summary of the model equations is given in Table 2.

3. Numerical implementation

In this section, a time-integration procedure for the constitutive relations presented above to simulate deformation of pseudoelastic NiTi single crystal is detailed. To this end, the heat transfer condition in the real experiment is firstly simplified under the assumption of uniform temperature field (Wang et al., 2017; Yin and Sun, 2012; Yin et al., 2014). Then, the constitutive model and the heat equations are implemented into the software CAST3M (2019) (Combescure et al., 1982) through user-defined subroutine UMAT. The algorithm for phase transformation part closely follows the work of Thamburaja and Anand (2001) (Appendix A). For rate-dependent plasticity parts, the numerical implementation is based on the algorithm of Li et al. (2008).

3.1. Simplification of the heat transfer condition

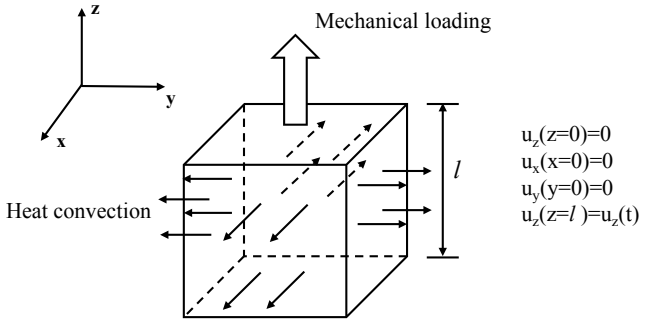

Figure 1 Thermal and mechanical boundary conditions

Table 2

Model summary of the basic and generalized cyclic model

State variables

$\boldsymbol{E}_e,\ \theta,\ \xi^{(i)},\ \dot{\gamma}_A^{(\alpha)},\ \dot{\gamma}_{tw}^{(t)},\ \dot{\gamma}_{trip}^{(\alpha)}$, (For generalized cyclic model: $\xi_{ua}^{(i)}$ and $\xi_{rm}^{(i)}$ are also included)

Main equations

$\boldsymbol{F} = \boldsymbol{F}_e\boldsymbol{F}_{inel}, \quad \boldsymbol{L} = \boldsymbol{L}_e + \boldsymbol{L}_{inel} \approx \boldsymbol{L}_e + \boldsymbol{L}_p^A + \boldsymbol{L}_{tr} + \boldsymbol{L}_{trip} + \boldsymbol{L}_p^M$

$\boldsymbol{L}_p^A = (1-\xi)\sum_{\alpha=1}^{24}\dot{\gamma}_A^{(\alpha)}\boldsymbol{S}_p{}^{(\alpha)},\ \boldsymbol{L}_p^M = \xi\sum_{t=1}^{11}\dot{\gamma}_{tw}^{(t)}\boldsymbol{S}_{tw}{}^{(t)},\ \boldsymbol{L}_{trip} = (1-\xi)\sum_{\alpha=1}^{24}\dot{\gamma}_{trip}^{(\alpha)}\boldsymbol{S}_p{}^{(\alpha)},\ \boldsymbol{L}_{tr} = \sum_{i=1}^{24}\dot{\xi}^{(i)}g_{tr}\boldsymbol{S}_{tr}{}^{(i)}$

Helmholtz free energy density

$\psi(\boldsymbol{E}_e, \xi^{(i)}, \theta) = \psi_e + \psi_\theta + \psi_{int} + \psi_p + \psi_{trans} + \psi_{cst}$

$\psi_e = \frac{1}{2}\boldsymbol{E}_e : \mathbb{C} : \boldsymbol{E}_e, \quad \psi_\theta = C[(\theta-\theta_0) - \theta\ln\frac{\theta}{\theta_0}] + \mu(\theta-\theta_0)\xi,\ \dot{\psi}_{int} = -\boldsymbol{B}_{int} : (\boldsymbol{L}_{tr} + \boldsymbol{L}_{trip})$

$\dot{\psi}_p = (1-\xi)\sum_{\alpha=1}^{24} g_A^{(\alpha)}|\dot{\gamma}_A^{(\alpha)}| + \xi\sum_{t=1}^{11} g_{tw}^{(t)}(\dot{\gamma}_{tw}^{(t)}),\ \psi_{trans} = \frac{1}{2}G\xi^2 + \frac{1}{2}\beta g_{tr}\xi(1-\xi)$

$\psi_{cst} = -w_0(1-\xi) - \sum_{i=1}^{24} w_i\xi^{(i)}$ (For generalized cyclic model: $\psi_{cst} = -w_0(1-\xi_{ua}-\xi) - \sum_{i=1}^{24} w_i(\xi^{(i)} - \xi_{rm}^{(i)})$)

Thermodynamic forces

$f_{tr}^{(i)} = g_{tr}(\boldsymbol{M} + \boldsymbol{B}_{int}) : \boldsymbol{S}_{tr}{}^{(i)} - \frac{1}{2}\boldsymbol{E}_e : \Delta\mathbb{C} : \boldsymbol{E}_e - \mu(\theta-\theta_0) - G\xi - \frac{1}{2}\beta g_{tr}(1-2\xi) + w_0 - w_i$

$f_A^{(\alpha)} = |\boldsymbol{M} : \boldsymbol{S}_p{}^{(\alpha)}| - g_A^{(\alpha)},\ f_{tw}^{(t)} = (\boldsymbol{M} : \boldsymbol{S}_{tw}{}^{(t)}) - g_{tw}^{(t)},\ f_{trip}^{(\alpha)} = (\boldsymbol{M} + \boldsymbol{B}_{int}) : \boldsymbol{S}_p{}^{(\alpha)}$

Evolution laws for plastic deformation

• Slip in austenite

$\dot{\gamma}_A^{(\alpha)} = \dot{\gamma}_A^0\left|\frac{\tau_A^{(\alpha)}}{g_A^{(\alpha)}}\right|^{\frac{1}{m_A}}\mathrm{sign}(\tau_A^{(\alpha)}),\ \dot{g}_A^{(\alpha)} = \sum_{\beta=1}^{24} h_A^{\alpha\beta}\left|\dot{\gamma}_A^{(\beta)}\right|$

• Slip in martensite

$\dot{\gamma}_{tw}^{(t)} = \dot{\gamma}_{tw}^0(\frac{\tau_{tw}^{(t)}}{g_{tw}^{(t)}})^{\frac{1}{m_{tw}}}$ if $\tau_{tw}^{(t)} > 0$, $\quad \dot{\gamma}_{tw}^{(t)} = 0$ if $\tau_{tw}^{(t)} \le 0$

$\dot{g}_{tw}^{(t)} = \sum_{s=1}^{11} h_{tw}^{ts}\dot{\gamma}_{tw}^{(s)}, \quad \dot{\xi}_{tw}^{(t)} = \frac{\dot{\gamma}_{tw}^{(t)}}{\gamma_T^{(t)}}$ $\quad (\xi_{tw}^{(t)} \ge 0$ and $\sum_{t=1}^{11}\xi_{tw}^{(t)} \le 1)$

• Slip due to TRIP

$\dot{\gamma}_{trip}^{(\alpha)} = \frac{\gamma_{sat}}{b}e^{-\frac{\xi_c}{b}}\left|\dot{\xi}\right|$ if $f_{trip}^{(\alpha)} > 0$, $\quad \dot{\gamma}_{trip}^{(\alpha)} = 0$ if $f_{trip}^{(\alpha)} \le 0$

(For generalized cyclic model: $\dot{\gamma}_{trip}^{(\alpha)} = \frac{\gamma_{sat}}{b_1}e^{-\frac{\xi_c}{b_1}}\left|\dot{\xi}\right|\mathrm{sign}(f_{trip}^{(\alpha)})$ $\quad$ when $\quad SF_{plastic}^{(\alpha)} > SF_{critical}$)

Evolution laws for phase transformation

$\mathscr{F}_{AM}^{(i)} = 0$ and $\dot{\mathscr{F}}_{AM}^{(i)} = 0 \quad \Rightarrow \dot{\xi} > 0$ forward transformation

$\mathscr{F}_{MA}^{(i)} = 0$ and $\dot{\mathscr{F}}_{MA}^{(i)} = 0 \quad \Rightarrow \dot{\xi} < 0$ reverse transformation

Internal variables related with cyclic degradation (for generalized cyclic model)

$\dot{\xi}_{ua}^{(i)} = \frac{\xi_{ua}^{sat}}{b_3}e^{-\frac{\xi_c}{b_3}}\left|\dot{\xi}^{(i)}\right|, \quad \dot{\xi}_{rm}^{(i)} = \frac{\xi_{rm}^{sat}}{b_4}e^{-\frac{\xi_c}{b_4}}\left|\dot{\xi}^{(i)}\right|, \quad \dot{f}_c^{(i)} = \frac{(f_{c\_sat}^{(i)} - f_{c\_0}^{(i)})}{b_5}e^{-\frac{\xi_c}{b_5}}\left|\dot{\xi}\right|, \quad \dot{G} = \frac{(G^{sat}-G^0)}{b_6}e^{-\frac{\xi_c}{b_6}}\left|\dot{\xi}\right|$

Evolution laws for dislocation density and stored energy

• Dislocation density: $\quad \rho_{tot} = (1-\xi)\rho_A + \xi\cdot\xi_{tw}\cdot\rho_M$

$\dot{\rho}_A^{(\alpha)} = c_1(\sqrt{\sum_{\alpha=1}^{24}\rho_A^{(\alpha)}} - c_2\rho_A^{(\alpha)})(|\dot{\gamma}_A^{(\alpha)}| + |\dot{\gamma}_{trip}^{(\alpha)}|), \quad \dot{\rho}_M^{(t)} = c_3(\sqrt{\sum_{t=1}^{11}\rho_M^{(t)}} - c_4\rho_M^{(t)})|\dot{\gamma}_{tw}^{(t)}|$

• Stored energy: $\quad E_{st} \approx \frac{1}{2}\rho_{tot}G_{shear}b^2$

The heat transfer is simplified as heat convection through the lateral surface S_{lat} to the air (see Fig.1). Then, the initial and boundary conditions of heat transfer equilibrium

equation are given by:

$$\theta(t=0) = \theta_r \qquad \forall \boldsymbol{x} \in \Omega \qquad \text{initial condition} \tag{69}$$

$$\boldsymbol{q} \cdot \boldsymbol{n} = h(\theta - \theta_r) \qquad \forall \boldsymbol{x} \in S_{lat} \qquad \text{boundary condition} \tag{70}$$

Where θ_r represents the ambient temperature, Ω is the whole domain occupied by the reference volume element with the volume V_Ω, $\boldsymbol{n}$ is the normal vector of the lateral surface S_{lat} and h is the heat exchange coefficient of ambient media.

Two assumptions are made: first, the heat conductivity of austenite is assumed to be isotropic due to its body-centered cubic crystal; second, the conductivity coefficient of austenite is assumed as same as that of martensite.

Integrating Eq. (40) over the whole domain Ω, yields:

$$C\dot{\theta}_\Omega V_\Omega + \int_\Omega \nabla \cdot \boldsymbol{q}\, d\Omega = (\dot{F}_{MD})_\Omega V_\Omega + (\dot{F}_{LT})_\Omega V_\Omega \tag{71}$$

Where $\theta_\Omega = \frac{1}{V_\Omega}\int_\Omega \theta\, d\Omega$, $(\dot{F}_{MD})_\Omega = \frac{1}{V_\Omega}\int_\Omega \dot{F}_{MD}\, d\Omega$, $(\dot{F}_{LT})_\Omega = \frac{1}{V_\Omega}\int_\Omega \dot{F}_{LT}\, d\Omega$ are the average temperature and heat sources rates in the domain Ω, respectively.

$$\dot{F}_{MD} = \sum_{i=1}^{24} f_{tr}^{(i)} \dot{\xi}^{(i)} + (1-\xi) \sum_{\alpha=1}^{24} f_A^{(\alpha)} \dot{\gamma}_A^{(\alpha)} + \xi \sum_{t=1}^{11} f_{tw}^{(t)} \dot{\gamma}_{tw}^{(t)} + (1-\xi) \sum_{\alpha=1}^{24} f_{trip}^{(\alpha)} \dot{\gamma}_{trip}^{(\alpha)} \tag{72}$$

$$\dot{F}_{LT} = \theta\mu \sum_{i=1}^{24} \dot{\xi}^{(i)} \tag{73}$$

Based on the assumption of uniform temperature field, the average temperature over the domain Ω is considered to be the same as the surface temperature θ_s, and expressed by : $\theta_\Omega = \theta_s = \theta$. Thus, considering Gauss's theory in Eq. (71), it yields:

$$C\dot{\theta} = (\dot{F}_{MD})_\Omega + (\dot{F}_{LT})_\Omega - \frac{h(\theta - \theta_r) \cdot S_\Omega}{V_\Omega} \tag{74}$$

$$(\dot{F}_{MD})_\Omega = \frac{\sum_{i=1}^n V_i \dot{F}_{MD}}{\sum_{i=1}^n V_i}, \quad (\dot{F}_{LT})_\Omega = \frac{\sum_{i=1}^n V_i \dot{F}_{LT}}{\sum_{i=1}^n V_i} \tag{75}$$

Where S_Ω is the area of surface S_{lat}. i labels the single crystals in the whole domain, n is the total number of the grains and V_i is the volume of each crystal.

3.2. Time-integration procedure

Let t, Δt and $\tau = t + \Delta t$ be the current time, the infinitesimal time increment and the new time, respectively. The objective of the algorithm is to update all variables at time τ in function of the variables at time t and the proposed new deformation gradient $\boldsymbol{F}(\tau)$. At time t, the following variables are given: (1) $\boldsymbol{F}(t)$, $\boldsymbol{F}_{inel}(t)$, $\boldsymbol{T}(t)$, $\boldsymbol{\sigma}(t)$; (2) $\xi^{(i)}(t)$, $\xi_c(t)$, $\gamma_A^{(\alpha)}(t)$, $\gamma_{tw}^{(t)}(t)$, $\gamma_{trip}^{(\alpha)}(t)$, $\tau_A^{(\alpha)}(t)$, $\tau_{tw}^{(t)}(t)$, $g_A^{(\alpha)}(t)$, $g_{tw}^{(t)}(t)$, $\boldsymbol{B}_{int}(t)$, $\theta(t)$ (For generalized cyclic model, $\xi_{ua}^{(i)}(t)$, $\xi_{rm}^{(i)}(t)$, $f_c(t)$ and $G(t)$ are also given). At time τ, the following variables are calculated: (1) $\boldsymbol{F}_{inel}(\tau)$, $\boldsymbol{T}(\tau)$, $\boldsymbol{\sigma}(\tau)$; (2) $\xi^{(i)}(\tau)$, $\xi_c(\tau)$, $\gamma_A^{(\alpha)}(\tau)$, $\gamma_{tw}^{(t)}(\tau)$, $\gamma_{trip}^{(\alpha)}(\tau)$, $\tau_A^{(\alpha)}(\tau)$, $\tau_{tw}^{(t)}(\tau)$, $g_A^{(\alpha)}(\tau)$, $g_{tw}^{(t)}(\tau)$, $\boldsymbol{B}_{int}(\tau)$, $\theta(\tau)$ (For generalized cyclic model, $\xi_{ua}^{(i)}(\tau)$, $\xi_{rm}^{(i)}(\tau)$, $f_c(\tau)$ and $G(\tau)$ are also calculated).

For the sake of clarity the algorithm is detailed in appendix A.

4. Determination of model parameters

It is worth noting that some parameters are dependent on the chemistry composition and stress state (Alkan and Sehitoglu, 2019; Alkan et al., 2017). As a result, the parameters obtained by fitting the experimental curves only apply for the relevant experimental conditions and chemistry composition.

4.1. Elastic and plastic parameters

In the present work, the approximation of $\mathbb{C}_M = \frac{1}{2}\mathbb{C}_A$ is made (Thamburaja and Anand, 2001) and the values of the elastic moduli are obtained by referring to (Brill et al., 1991).

The initial hardening coefficient (h_A^0 and h_{tw}^0) and hardening exponent (a_A and a_{tw}) affect the slope during plastic deformation while the initial slip and twinning resistance (g_A^0 and g_{tw}^0) control the yield stress of slip in austenite and deformation twinning in martensite, respectively. These parameters are chosen to match the experimental stress-strain curves. In the absence of experimental data, the strain rate sensitivity (m_A and m_{tw}), reference strain rate ($\dot{\gamma}_A^0$ and $\dot{\gamma}_{tw}^0$), latent hardening parameter (q_a and q_{tw}) and saturation value for slip and twinning resistance (g_A^∞ and g_{tw}^∞) are taken from the work of Dhala et al. (2019); Kalidindi (1998); Manchiraju and Anderson (2010). The parameters related with TRIP are adopted

based on the physical mechanisms for cyclic behavior of NiTi SMAs. Under the monocyclic loading conditions, some effects of the parameters on thermomechanical response (like the impact of B_{sat} on transformation stress plateau levels) are not revealed. As a result, the parameters related with TRIP in the basic model are estimated based on the work of (Yu et al., 2014c). For the generalized cyclic model, these parameters will be discussed in next subsection with the transformation related parameters since they are closely linked with phase transformation.

4.2. Transformation related parameters

Some approximations are made to determine the transformation parameters. First, all transformation systems have the same critical driving force: $f_c^{(i)} = f_c$. Second, the hardening resulting from the interactions between austenite and martensite is ignored: $\beta = 0$. Third, the contribution from elastic strain of different phases to the driving force for transformation is neglected: $\frac{1}{2}\boldsymbol{E}_e : \Delta\mathbb{C} : \boldsymbol{E}_e = 0$. The calibration of the transformation related parameters for the basic and generalized cyclic model is discussed separately in the following subsections.

4.2.1. For basic model considering monocyclic deformation

As mentioned above (Eq. (18), θ_0 is specified by θ_{AM} and θ_{MA} from DSC measurements. In order to determine the value for critical driving force $f_c^{(i)}$ and stress-temperature coefficient μ, the hardening interactions between martensite variants and the effect of internal stress are ignored. As a result, the driving force for each transformation system is simplified as:

$$f_{tr}^{(i)} = g_{tr}\tau_{tr}^{(i)} - \mu(\theta - \theta_0), \qquad \text{with} \quad \tau_{tr}^{(i)} = \boldsymbol{M} : \boldsymbol{S}_{tr}^{(i)} \tag{76}$$

Using the definition of $\boldsymbol{\sigma}$ (Eq. (3)), it has $\tau_{tr}^{(i)} = det(\boldsymbol{F}_e)\boldsymbol{\sigma} : \boldsymbol{S}_{tr}^{(i)} \approx \boldsymbol{\sigma} : \boldsymbol{S}_{tr}^{(i)}$.

Due to the existence of crystal orientations, the local crystal coordinate system might not be always consistent with the global ones. Set $\boldsymbol{a}$ as a unit vector in the crystal coordinate system, which is along the loading axis in the global system. Then the largest Schmid factor for transformation SF_{max} can be written as:

$$SF_{max} = max[(\boldsymbol{a} \otimes \boldsymbol{a}) : \boldsymbol{S}_{tr}^{(i)}] \tag{77}$$

Accordingly, the consistency conditions for phase transformation are given by:

$$f_{tr}^{(i)} = g_{tr}\sigma_{AM} \cdot SF_{max} - \mu(\theta - \theta_0) = f_c \qquad \text{Forward transformation} \tag{78}$$

$$f_{tr}^{(i)} = g_{tr}\sigma_{MA} \cdot SF_{max} - \mu(\theta - \theta_0) = -f_c \qquad \text{Reverse transformation} \tag{79}$$

Where σ_{AM} and σ_{MA} are the start stresses for forward and reverse transformation, respectively.

Considering Eq. (78) and (79), it is deduced that:

$$f_c = \frac{1}{2} g_{tr} \cdot SF_{max}(\sigma_{AM} - \sigma_{MA}) \tag{80}$$

$$\mu = \frac{1}{2(\theta - \theta_0)} g_{tr} \cdot SF_{max}(\sigma_{AM} + \sigma_{MA}) \tag{81}$$

4.2.2. For generalized model considering cyclic deformation

In order to decouple the effect of f_c and μ on the start stress of forward transformation and hysteresis width, θ_0 is written as (Lagoudas and Entchev, 2004; Yu et al., 2014a): $\theta_0 = M_s + \frac{f_c}{\mu}$. M_s is the start temperature of martensite transformation. Thus, the driving force $f_{tr}^{(i)}$ in Eq. (32) can be rewritten as:

$$f_{tr}^{(i)} = g_{tr}(\boldsymbol{M} + \boldsymbol{B}_{int}) : \boldsymbol{S}_{tr}{}^{(i)} - \mu(\theta - M_s) - G\xi + f_c \tag{82}$$

Fig. 2 shows the illustration for determining the parameters related with transformation. The solid and dash line represent the stress-strain curve of the first and stabilized cycle, respectively. The parameters $\{\mu,\ B_{sat},\ f_{c\_0},\ f_{c\_sat},\ G^0,\ G^{sat}\}$ could be derived from the critical points at the curves and the final forms are given as follows. The detailed derivation

process is listed in appendix B.

$$\mu = \frac{g_{tr}\boldsymbol{\sigma}_1^1 : \boldsymbol{S}_{tr}^{(i)}}{\theta - M_s} = \frac{g_{tr}\sigma_1^1 \cdot SF_{tr}^{max}}{\theta - M_s} \tag{83}$$

$$f_{c\_0} = \frac{1}{2} g_{tr}(\boldsymbol{\sigma}_2^1 - \boldsymbol{\sigma}_3^1) : \boldsymbol{S}_{tr}{}^{(i)} = \frac{1}{2} g_{tr}(\sigma_2^1 - \sigma_3^1) \cdot SF_{tr}^{max} \tag{84}$$

$$f_{c\_sat} = \frac{1}{2} g_{tr}(\boldsymbol{\sigma}_2^{sat} - \boldsymbol{\sigma}_3^{sat}) : \boldsymbol{S}_{tr}{}^{(i)} = \frac{1}{2} g_{tr}(\sigma_2^{sat} - \sigma_3^{sat}) \cdot SF_{tr}^{max} \tag{85}$$

$$B_{sat} = \frac{(\boldsymbol{\sigma}_1^1 - \boldsymbol{\sigma}_1^{sat}) : \boldsymbol{S}_{tr}{}^{(i)}}{(\sum_{i=1}^{24} \boldsymbol{S}_{tr}{}^{(i)}) : \boldsymbol{S}_{tr}{}^{(i)}} = \frac{(\sigma_1^1 - \sigma_1^{sat}) \cdot SF_{tr}^{max}}{(\sum_{i=1}^{24} \boldsymbol{S}_{tr}{}^{(i)}) : \boldsymbol{S}_{tr}{}^{(i)}} \tag{86}$$

$$G^0 = \frac{g_{tr}(\boldsymbol{\sigma}_2^1 - \boldsymbol{\sigma}_1^1) : \boldsymbol{S}_{tr}{}^{(i)} + g_{tr}\boldsymbol{B}_{int}\big|_{at\ \boldsymbol{\sigma}_2^1} : \boldsymbol{S}_{tr}{}^{(i)}}{\xi\big|_{at\ \boldsymbol{\sigma}_2^1}} \approx \frac{g_{tr}(\sigma_2^1 - \sigma_1^1) \cdot SF_{tr}^{max}}{\xi\big|_{at\ \boldsymbol{\sigma}_2^1}} \tag{87}$$

$$G^{sat} = \frac{g_{tr}(\boldsymbol{\sigma}_2^{sat} - \boldsymbol{\sigma}_1^{sat}) : \boldsymbol{S}_{tr}{}^{(i)}}{\xi\big|_{sat}} = \frac{g_{tr}(\sigma_2^{sat} - \sigma_1^{sat}) \cdot SF_{tr}^{max}}{\xi\big|_{sat}} \tag{88}$$

$$\xi\big|_{at\ \boldsymbol{\sigma}_2^1} = \frac{E_{global}^{tr}|_{at\ \boldsymbol{\sigma}_2^1}}{g_{tr} \cdot SF_{tr}^{max}} \tag{89}$$

$$\xi\big|_{sat} = \frac{E_{global}^{tr}|_{sat}}{g_{tr} \cdot SF_{tr}^{max}} \tag{90}$$

The relevant evolution rate controlling parameters $\{b_2, b_5 \text{ and } b_6\}$ are obtained by fitting

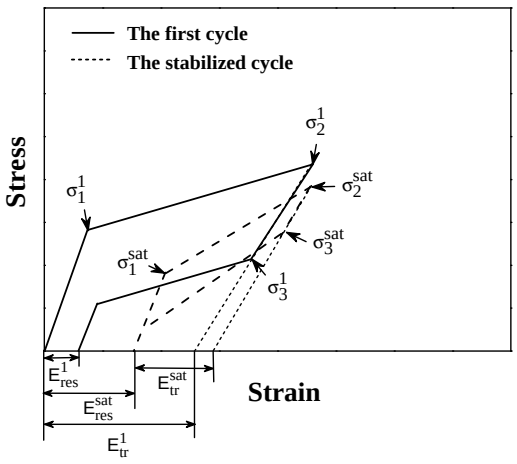

Figure 2 Illustration for determing the material paramters

the evolution curves of corresponding parameters during cyclic loading.

As mentioned in the introduction part, the increment of residual strain in the cyclic deformation curves is attributed to the accumulation of plastic deformation and residual

martensite. However, it is difficult to determine the percentage of contributions of each mechanism to the residual strain from the experimental data. Besides, the portion could evolve during the cyclic deformation (Yu et al., 2014b). Thus, in the present work, only generalized forms of the γ_{sat} and ξ_{rm}^{sat} are given:

$$\xi_{rm}^{sat} = \frac{\phi E_{global}^{res}|_{sat}}{g_{tr} \sum_{i \in \mathscr{A}} SF_{tr}^{(i)}} \tag{91}$$

$$\gamma_{sat} = \frac{(1-\phi) E_{global}^{res}|_{sat}}{\sum_{\alpha \in \mathscr{B}} SF_{plastic}^{(\alpha)}} \tag{92}$$

Where ϕ and $(1-\phi)$ represent the percentage of contribution on residual strain from RM and TRIP, respectively. It satisfies $\phi \in [0,1]$. $E_{global}^{res}|_{sat}$ is the global residual strain in the stabilized cycle. The set $\mathscr{A}$ and $\mathscr{B}$ refer to the sets containing all the active transformation systems and slip systems ($SF_{plastic}^{(\alpha)} > SF_{critical}$), respectively. The choice of ϕ and $SF_{critical}$ are dependent on the specific situation of the experimental data and a trial-and-error method is needed for determination by fitting the experimental curves.

It should be noted that the UA refers to the untransformed austenite after full transformation other than the austenite existing in incomplete phase transformation case (as shown in Fig. 2). For the incomplete transformation cases, the effect of UA is neglected and ξ_{ua}^{sat} is set to be zero. For the full transformation cases, according to the work of Zhang et al. (2019a), the reduction in recoverable strain after stabilized cycle is attributed to the accumulation of UA and RM. Consequently, the ξ_{ua}^{sat} can be estimated from:

$$\xi_{ua}^{sat} = \frac{(E_{tr}^{sat} - E_{tr}^{1}) - \phi E_{global}^{res}|_{sat}}{g_{tr} \sum_{i \in \mathscr{A}} SF_{tr}^{(i)}} \tag{93}$$

E_{tr}^{1} and E_{tr}^{sat} are the transformation strain in the first and stabilized cycles, respectively.

4.3. Thermomechanical coupling parameters

θ_r is the ambient temperature taken as 298 K in the present work. Heat exchange coefficient h and specific heat capacity C are taken based on the experimental conditions. Here, they are equal to 110 W $m^{-2}K^{-1}$ and 2.86 MPa/K, respectively, according to the work of Morin et al. (2011). The values of surface S_Ω and volume V_Ω are calculated according to the dimensions of the simulated body.

4.4. Dislocation density related parameters

In the initial state of pseudoelastic NiTi SMA, the material is in a complete austenite phase. Thus, the initial dislocation density ρ_0 comes from the sum of dislocation density in each austenite slip system and the initial values for dislocation density in martensite twinning system are equal to zero. Assuming that each austenite slip system has the same initial dislocation density, it gives $\rho_{A\_0}^{(\alpha)} = \rho_{A\_0} = \frac{1}{24}\rho_0$. The value of ρ_0 is set as 1×10^{14} m^{-2} referring to the work of Xiao et al. (2018). Besides, the controlling parameters in austenite slip systems and martensite twinning systems are set to be the same ($c_1 = c_3$, $c_2 = c_4$). The values for c_1 and c_2 can be determined by referring to Yu et al. (2015b).

5. Results of the monocyclic deformation using the basic model

In this section, the basic model is implemented, following the algorithm presented in the appendix A, into the software CAST3M (2019) through a user material subroutine UMAT. To this end, a solid cube with 8 nodes (CUB8) is used. The loading axis is along the Z axis of the element with the boundary condition shown in Fig. 1. A series of uniaxial tests under various loading conditions are presented. It should be mentioned that in the former subsections, a low strain rate of 3×10^{-4}s^{-1} is used and thermomechanical coupling effect is "switched off". This effect is discussed in subsection 5.4 through a series tests under different strain rates.

Table 3

Material parameters used for verification of the model.

Elastic constants
$\mathbb{C}_A^{11} = 130$ GPa, $\mathbb{C}_A^{22} = 98$ GPa, $\mathbb{C}_A^{44} = 34$ GPa, $\mathbb{C}_M = \frac{1}{2}\mathbb{C}_A$
Plastic parameters for austenite slip
$\dot{\gamma}_A^0 = 0.002$ s^{-1}, $m_A = 0.02$, $h_A^0 = 500$ MPa, $g_A^0 = 320$ MP, $g_A^\infty = 900$ MPa, $a_A = 0.125$, $q_A = 1.4$
Plastic parameters for martensite twinning
$\dot{\gamma}_{tw}^0 = 0.001$ s^{-1}, $m_{tw} = 0.02$, $h_{tw}^0 = 150$ MPa, $g_{tw}^0 = 600$ MP, $g_{tw}^\infty = 900$ MPa, $a_{tw} = 0.125$, $q_{tw} = 1.4$
Plastic parameters for TRIP
$\gamma_{sat} = 0.003$ (for simulation considering TRIP), $\gamma_{sat} = 0$ (for other simulations), $b = 1$, $B_{sat} = 500$
Phase transformation parameters
$\theta_0 = 256$ K, $G = 0$ MPa, $\beta = 0$ MPa, $g_{tr} = 0.1308$, $f_c^{(i)} = 8.003$ MPa, $\mu = 0.406$ MPa/K

5.1. Uniaxial tensile test of single crystal

In this subsection, the model is verified qualitatively to catch the different behaviors related with the pseudoelasticity of NiTi SMA. At this stage, no comparison with the experimental results is carried out. Thus, the parameters used here are taken from the literature and are listed in Table 3; Elastic constants and austenite plasticity parameters from (Manchiraju and Anderson, 2010), deformation twinning parameters from (Dhala et al., 2019), plastic parameters for TRIP from (Yu et al., 2014c) and phase transformation parameters from (Thamburaja and Anand, 2001).) It should be mentioned that the TRIP mechanism is "switched off" by setting $\gamma_{sat} = 0$ in the first 4 series simulations while investigating the inelastic deformation modes of slip and twinning. The effect of TRIP is discussed specifically in the last part of the subsection with enlarged value for parameter γ_{sat} to qualitatively reveal its physical interpretation. In the simulations, [1 1 1] orientation is chosen for the crystallographic orientation since NiTi wires exhibiting dominant [1 1 1] texture along the wire axis (Laplanche et al., 2017).

5.1.1. Pseudoelastic tensile response at 298 K

Fig. 3 shows the pseudoelasticity at 298 K and 7% strain. It can be seen that a fully forward transformation occurs with a complete reversal after unloading. No residual strain is observed which is consistent with the result shown in Fig. 3(c) and (d): local slip γ_A given by $\gamma_A = \sum_{\alpha=1}^{24} |\gamma_A^{(\alpha)}|$ and deformation twinning γ_{tw} given by $\gamma_{tw} = \sum_{t=1}^{11} |\gamma_{tw}^{(t)}|$ are inactive under this condition. The pseudoelastic strain is about 5.6%, which is less than the nearly 11% measured by Miyazaki et al. (1984) since the martensite reorientation and martensite detwinning are not considered in the present work of pseudoelastic study.

5.1.2. Temperature effect

Simulations of uniaxial tension tests at 7% strain and different temperatures are reported in Fig. 4. As shown in Fig. 4(a)-(c), the start stresses for both forward and reverse phase transformation (σ_{AM} and σ_{MA}) increase as the temperature rises. This is due to the increase of back force term $\mu(\theta - \theta_0)$ in the driving force for phase transformation (Eq. (32)), which

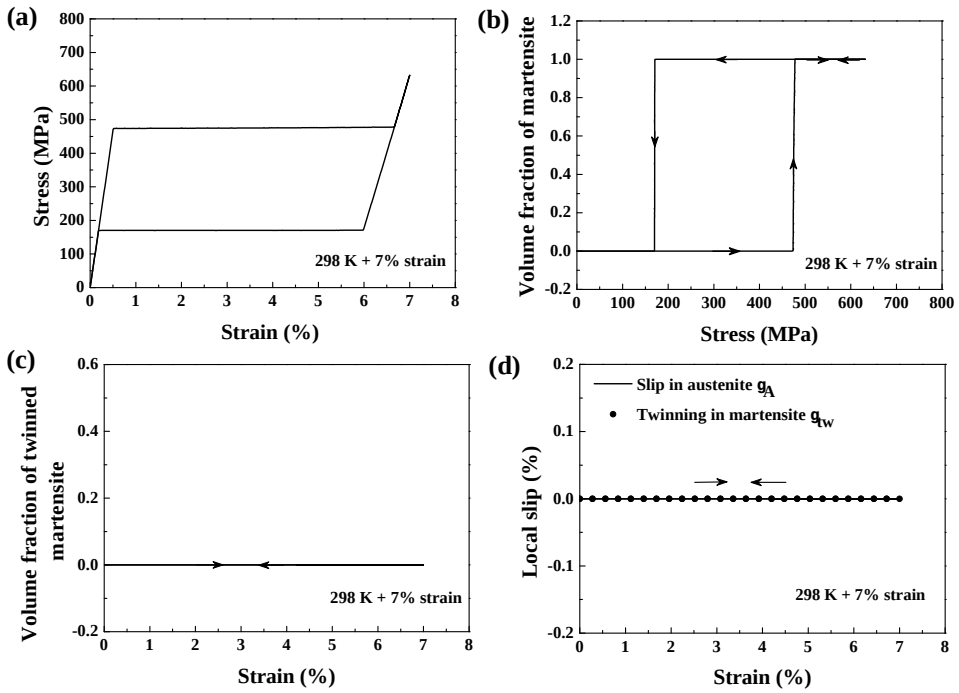

Figure 3 Simulated responses of a single crystal in uniaxial tension tested at 298 K and 7% strain (with TRIP mechanism "switched off"). (a) Macrostress-macrostrain response; (b) Evolution of martensite volume fraction with macrostress; (c) Evolution of twinned martensite volume fraction with macrostrain; (d) Evolution of local slip activity with macrostrain.

makes phase transformation occurs at higher stress. When σ_{AM} is larger than the yield stress of austenite (see Fig. 4(h)-(i)), plastic slip deformation in austenite occurs before the phase transformation. A coupling between plasticity and phase transformation is shown as the slip deformation increases monotonically during the forward phase transformation. When the temperature increases, more austenite slip is activated, which leads to the increase of the residual strain. Besides, the volume fraction of martensite at the end of forward phase transformation decreases with the elevation of the temperature (see Fig. 4(d)-(f)). Fig. 5 shows the simulated results of a single crystal tensile tested at 323 K and 7 % strain for which plasticity is "switched off" by setting extremely high initial slip resistance g_A^0 as 3200 MPa. Pure phase transformation without residual strain is observed in Fig. 5(a). Compared to Fig. 4(f) and Fig. 5(b), the forward phase transformation starts at the same stress level, but the volume fraction of phase transformation is lower in the case with plasticity than

that of the case without plasticity. This reveals the retard effect of plastic deformation on the transformation (Dhala et al., 2019).

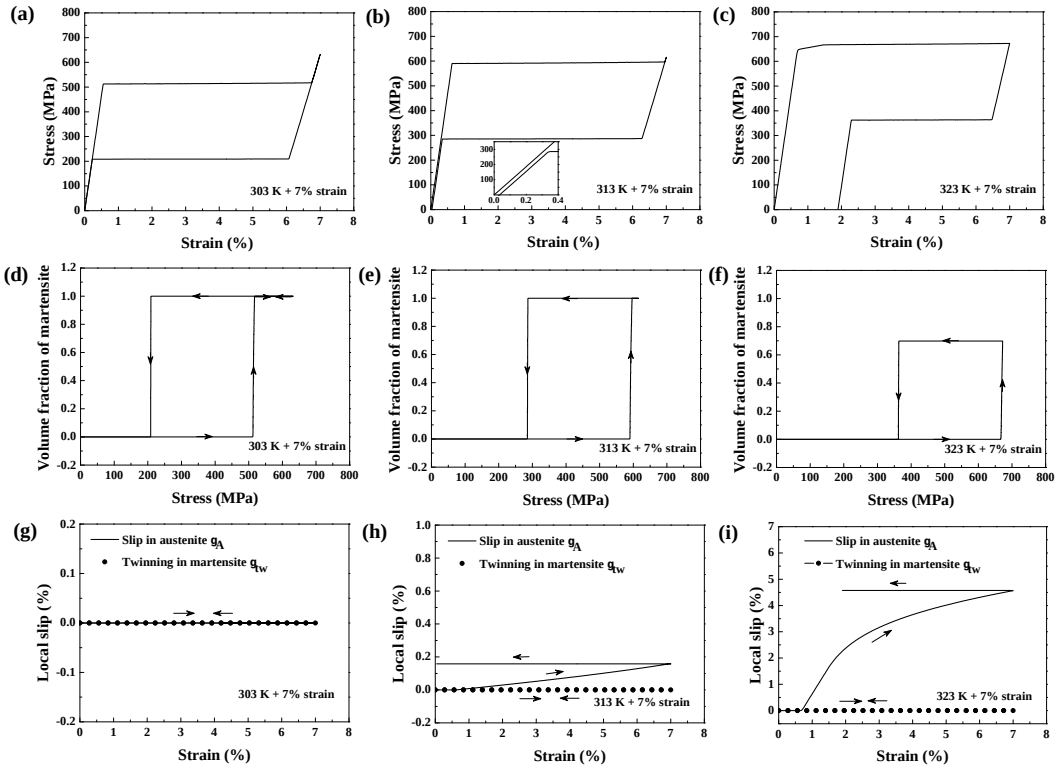

Figure 4 Simulated responses of a single crystal in uniaxial tension tested at 7% strain and at different temperatures (with TRIP mechanism "switched off"). (a), (b) and (c) are the macrostress-macrostrain responses at 303 K, 313 K and 323 K, respectively; (d), (e) and (f) are the evolutions of martensite volume fraction with macrostress at 303 K, 313 K and 323 K, respectively; (g), (h) and (i) are the evolution of local deformation activity with macrostrain at 303 K, 313 K and 323 K, respectively.

5.1.3. Strain effect

Fig. 6 shows the responses of uniaxial tension at 298 K under different imposed strains. The residual strain increases with the maximum imposed strains. The plastic deformation occurs after the phase transformation plateau at a very high stress. According to Fig. 6(j)-(l), the plastic deformation is attributed to the deformation twinning in martensite γ_{tw} while slip in austenite γ_A remains 0. Consistent with the twinning deformation results, the volume fraction of twinned martensite increases with the increase of strain amplitude (Fig.

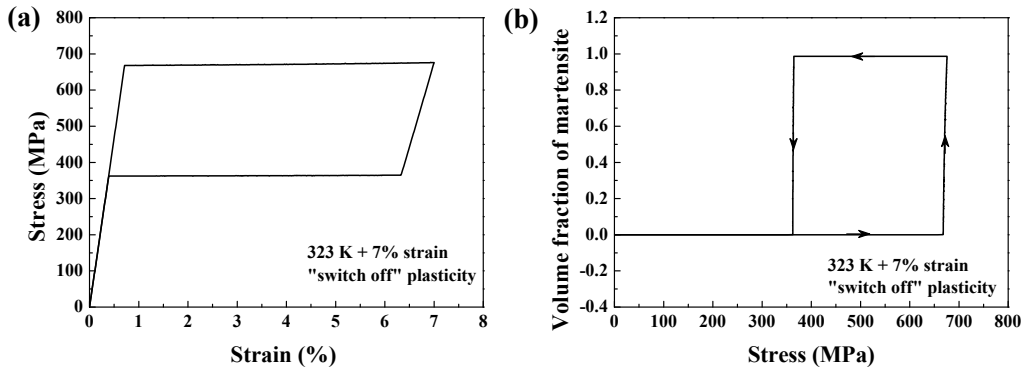

Figure 5 Simulated responses of a single crystal in uniaxial tension tested at 323 K and 7% strain with plasticity is "switched off".

6(g)-(i)). The existence of twinned martensite restraints the reverse phase transformation and leads to a residual martensite at the end of unloading (see Fig. 6(d)-(f)). This result is in good agreement with the previous studies (Dhala et al., 2019; Wang et al., 2008b). Part of the martensite structure is highly deformed at large strains and it cannot fully transform back to austenite (Sehitoglu et al., 2000). Different from the results of plastic deformation in austenite, the stress-strain curve of reverse transformation is also affected by the deformation twinning. The width of the reverse transformation plateau becomes smaller. Besides, the transformation continues after the end of the stress plateau, which is consistent with the report in Sehitoglu et al. (2001a).

5.1.4. Pseudoelastic tensile response at high temperature and large strain

Fig. 7 shows the simulation test at 323 K and 15 %, in which case, both slip and deformation twinning are activated. Due to the large strain amplitude, a complete forward transformation occurs. Besides, no residual martensite is left, compared with the case in Fig. 6(c). Since the high temperature increases the reverse start stress σ_{MA}, martensite can fully transform back to austenite.

5.1.5. Pseudoelastic tensile response considering TRIP

Fig. 8 shows the simulation test at 298 K and 7% strain, which considers TRIP mechanism. Compared with the pure pseudoelastic transformation case in Fig. 3, residual strain

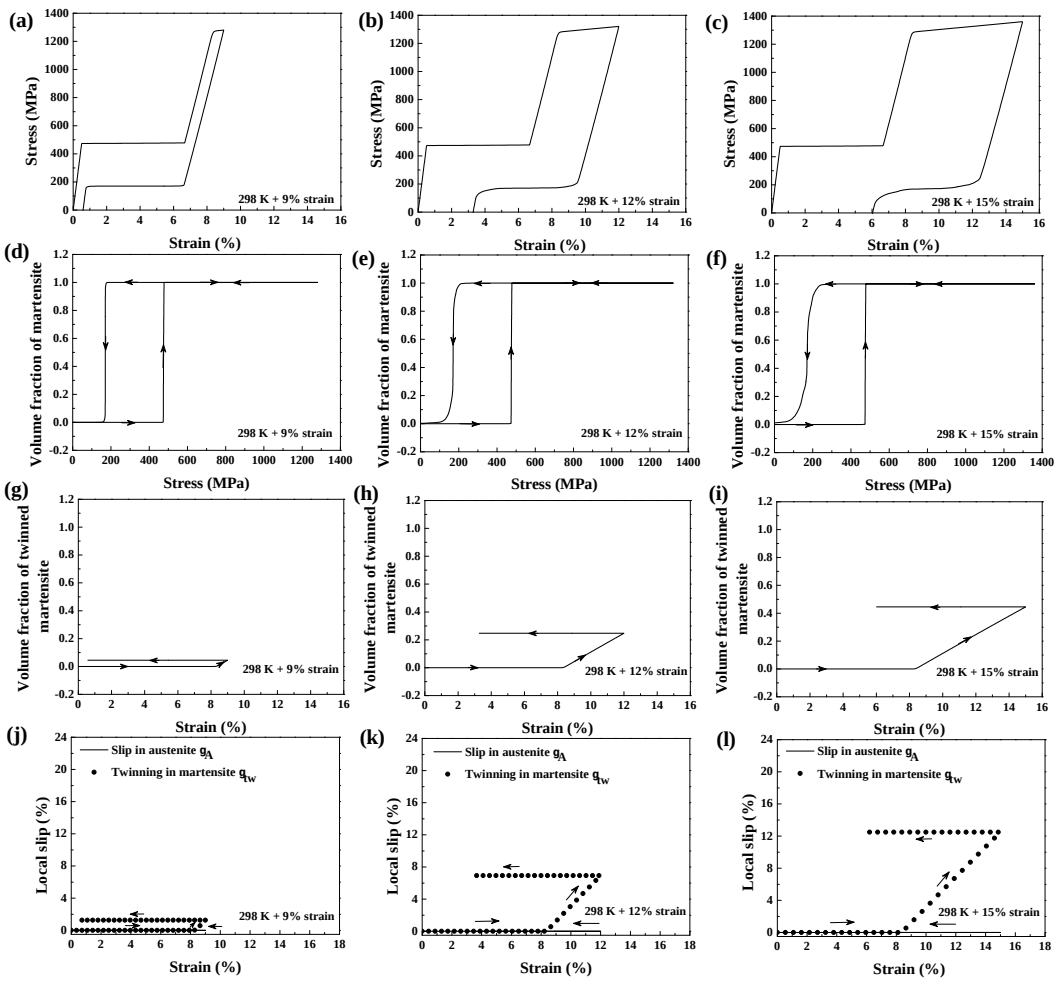

Figure 6 Simulated responses of a single crystal in uniaxial tension tested at 298 K and at different maximum strain (with TRIP mechanism "switched off"). (a), (b) and (c) are the macrostress-macrostrain responses at 9%, 12% and 15%, respectively; (d), (e) and (f) are the evolutions of martensite volume fraction with macrostress at 9%, 12% and 15%, respectively; (g), (h) and (i) are the evolution of twinned martensite volume fraction with macrostrain at 9%, 12% and 15%, respectively; (j), (k) and (l) are the evolution of local deformation activity with macrostrain at 9%, 12% and 15%, respectively.

occurs and the phase transformation becomes incomplete due to the introduction of TRIP (Fig. 8(a) and (b)). Since the local slip γ_A and γ_{tw} are inactivated (Fig. 8(c)), the plastic deformation is only attributed to the TRIP given by $\gamma_{trip} = \sum_{\alpha=1}^{24} |\gamma_{trip}^{(\alpha)}|$ (Fig. 8(d)). It is shown that the local slip of TRIP occurs when forward phase transformation starts and remains unchanged when reverse phase transformation finishes. Besides, the slip of TRIP accumulates monotonically during phase transformation. Fig. 9 shows the simulation test

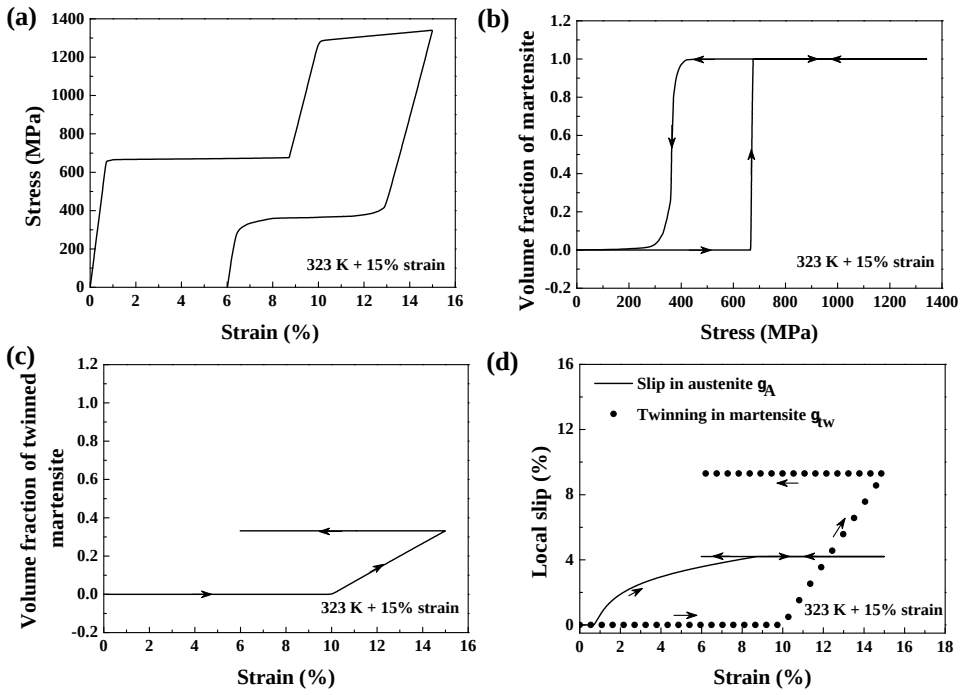

Figure 7 Simulated responses of a single crystal in uniaxial tension tested at 323 K and 15% strain (with TRIP mechanism "switched off"). (a) Macrostress-macrostrain response; (b) Evolution of martensite volume fraction with macrostress; (c) Evolution of twinned martensite volume fraction with macrostrain; (d) Evolution of local deformation activity with macrostrain.

at 323 K considering TRIP mechanism. It can be seen that both conventional slip in austenite and TRIP are activated at the high testing temperature (Fig. 9(b)) and they can be distinguished from simulation point of view by referring to γ_A and γ_{trip}, respectively.

5.2. Uniaxial compresssion test of single crystal

The simulation results of a uniaxial compression test at 298 K and 7% strain are shown in Fig. 10. The parameters are given in Table. 3. Compared with Fig. 3, a clear tension-compression asymmetry is revealed. The absolute value of start stress for forward and reverse transformation (σ_{AM} and σ_{MA}) are higher in compression test than those in tension test. Besides, plastic deformation in austenite is activated in compression case. Such asymmetry origins in the crystallography. According to Eq. (77), the largest Schmid factor SF_{max} for phase transformation is related to the unit vector of loading axis. When the loading direction changes, the SF_{max} changes, and the relevant activated transformation systems

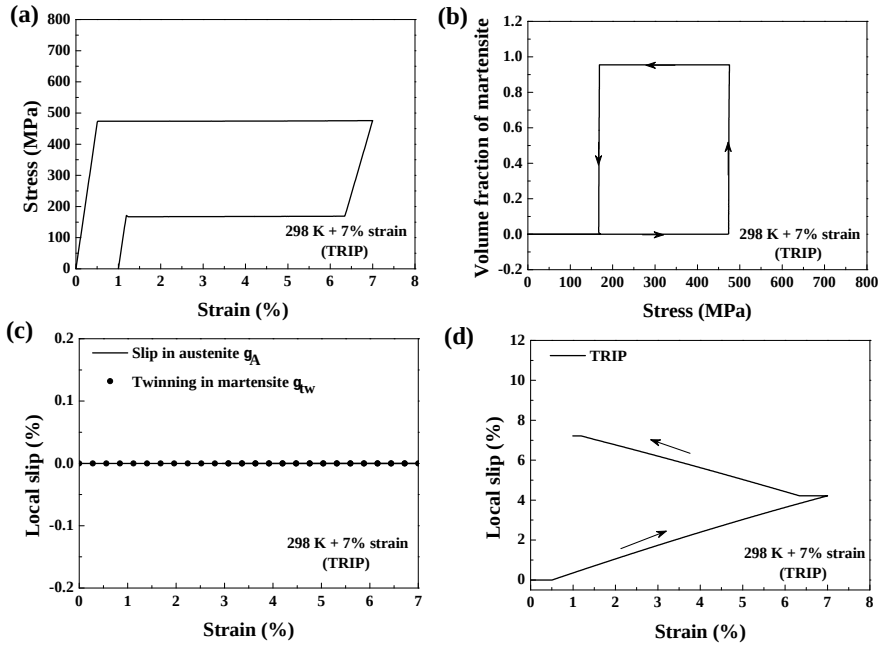

Figure 8 Simulated responses of a single crystal in uniaxial tension tested at 298 K and 7% strain which considers TRIP. (a) Macrostress-macrostrain response; (b) Evolution of martensite volume fraction with macrostress; (c) Evolution of local deformation activity with macrostrain; (d) Evolution of TRIP deformation activity with macrostrain.

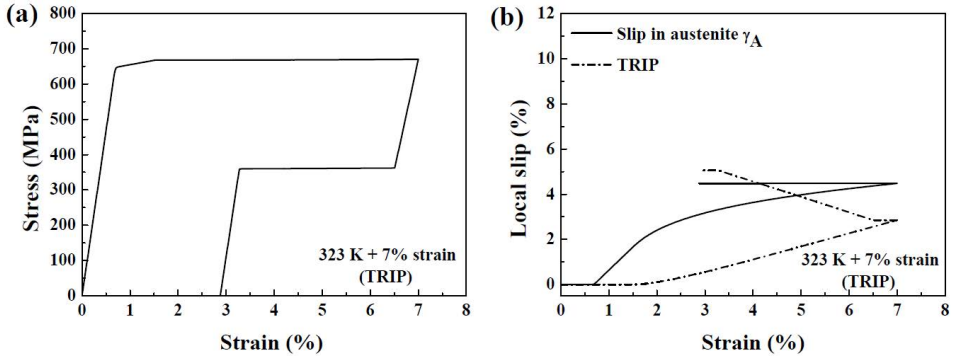

Figure 9 Simulated responses of a single crystal in uniaxial tension tested at 323 K and 7% strain which considers TRIP. (a) Macrostress-macrostrain response; (b) Evolution of local slip with macrostrain.

will change consequently. Assuming the critical driving force for phase transformation is the same under tension and compression cases, then the start stress for phase transformation will change in order to satisfy the consistency condition (Eq. (78) and (79)). This explains why the absolute value of σ_{AM} in compression test is different from that in tensile test. Since

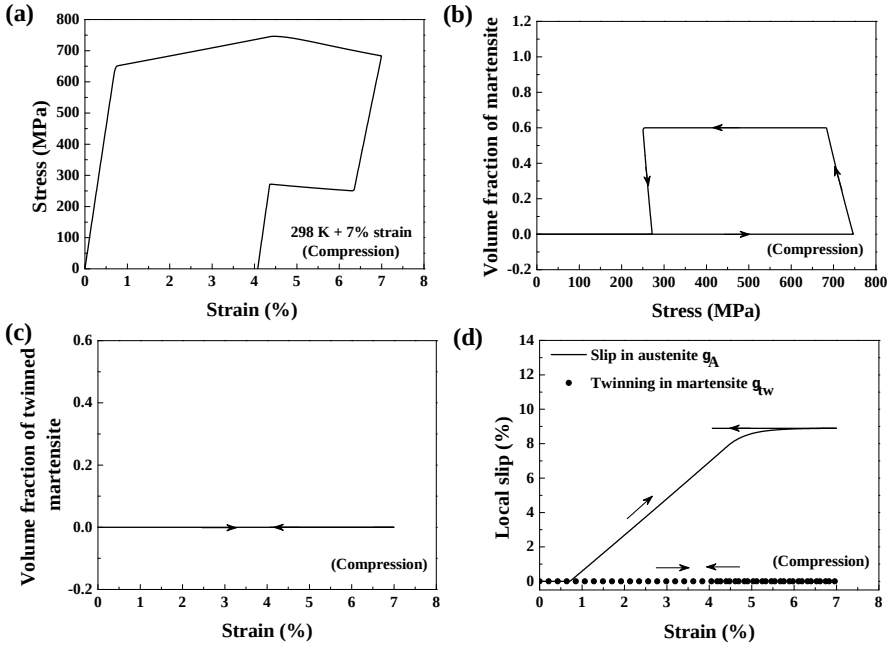

Figure 10 Simulated responses of a single crystal in uniaxial compression tested at 298 K and 7% strain. (a) Macrostress-macrostrain response; (b) Evolution of martensite volume fraction with macrostress; (c) Evolution of twinned martensite volume fraction with macrostrain; (d) Evolution of local deformation activity with macrostrain. (Here, the absolute values of macrostress and macrostrain are used)

the σ_{AM} is high in compression case, the plastic slip in austenite occurs before the forward phase transformation and results in a residual strain after unloading.

5.3. Effect of crystal orientations

The simulations of uniaxial compression tests are carried out on a single crystal at 298 K and along different crystallographic directions of [2 2 1], [2 1 0], [1 2 3], [1 0 0], [2 1 1] and [1 1 1]. According to the experimental results of Gall et al. (2002), predominantly plastic deformation is observed in [1 1 1] orientation while [2 1 0] orientation exhibits almost perfect pseudoelasticity. Thus, the [1 1 1] experimental response is used for fitting the plasticity parameters and the phase transformation parameters are calibrated according to stress-strain curve of [2 1 0]. The calibrated parameters are listed in Table 4. The comparison of simulated and experimental results are plotted in Fig. 11, using dash-dot lines and solid lines, respectively. It is seen that the mechanical responses from simulations are in good

Table 4

Material parameters calibrated for single crystal of solutionized Ti-50.9 at.%Ni SMA.

Elastic constants
$\mathbb{C}_A^{11} = 130$ GPa, $\mathbb{C}_A^{22} = 98$ GPa, $\mathbb{C}_A^{44} = 34$ GPa, $\mathbb{C}_M = \frac{1}{2}\mathbb{C}_A$
Plastic parameters for austenite slip
$\dot{\gamma}_A^0 = 0.002$ s^{-1}, $m_A = 0.02$, $h_A^0 = 1400$ MPa, $g_A^0 = 188$ MP, $g_A^\infty = 900$ MPa, $a_A = 0.125$, $q_A = 1.4$
Plastic parameters for martensite twinning
$\dot{\gamma}_{tw}^0 = 0.001$ s^{-1}, $m_{tw} = 0.02$, $h_{tw}^0 = 150$ MPa, $g_{tw}^0 = 600$ MP, $g_{tw}^\infty = 900$ MPa, $a_{tw} = 0.125$, $q_{tw} = 1.4$
Plastic parameters for TRIP
$\gamma_{sat} = 0.003$, $b = 1$, $B_{sat} = 500$
Phase transformation parameters
$\theta_0 = 257$ K, $G = 5$ MPa, $\beta = 0$ MPa, $g_{tr} = 0.1308$, $f_c^{(i)} = 10$ MPa, $\mu = 0.3654$ MPa/K

agreement with experiments, except for the orientation of [1 1 1]. Extreme plastic work hardening is shown in the experimental curves of [1 1 1] orientation, which is also failed to be captured in former works (Dhala et al., 2019; Hossain and Baxevanis, 2021; Yu et al., 2015a). As mentioned by Gall et al. (2002), the specimens were heated to 373 K after unloading and no recovered strain were measured. Thus, the residual strain in the curves are permanent plastic strain and not strain from residual martensite. This characteristic is also captured by the proposed model. The volume fraction of martensite turns back to zero after unloading. The stress-strain curves are strongly dependent on the crystallographic orientations, and the start stresses for phase transformation, the slope of transformation stage, width of hystersis loop and residual strain differ in different orientations. It should be mentioned that the experimental data used here is for solutionized NiTi single crystal. The characteristics of the mechanical responses might change for the aging treated samples since different aging treatments lead to different sizes of Ti_3Ni_4, which alter the resistances to both phase transformation and dislocation motion, and subsequently influence the transformation temperatures and the mechanical responses of NiTi single crystal (Gall et al., 2001; Gall and Maier, 2002; Miyazaki et al., 1984).

5.4. Effect of thermomechanical coupling

Fig. 12 shows the simulation results of a uniaxial tensile test at 298 K and 7% strain with different strain rates (using parameters in Table. 3). The stress-strain curves are plotted

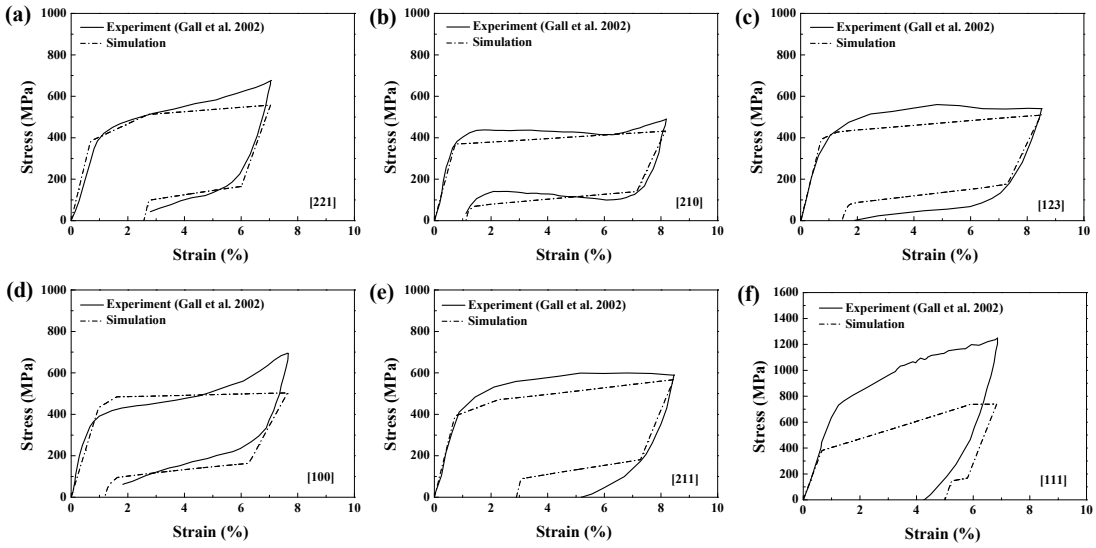

Figure 11 Simulated mechanical responses in uniaxial compression for single NiTi SMAs oriented along different directions. (a) [2 2 1]; (b) [2 1 0]; (c) [1 2 3]; (d) [1 0 0]; (e) [2 1 1]; (f) [1 1 1]. The experimental results from Gall et al. (2002) are also plotted by solid lines in the figures for comparison.

in Fig. 12(a). At a low strain rate $3 \times 10^{-4}\mathrm{s}^{-1}$, it shows pure phase transformation with horizontal plateau, similar to Fig. 3(a), indicating an isothermal response at this strain rate. With the increase of the strain rate, the phase transformation curve becomes steeper and the residual strain becomes more obvious. Fig. 12(b) shows the temperature evolution with normalized time under different strain rates. At a strain rate of $3\times10^{-4}\mathrm{s}^{-1}$, the temperature barely changes. When the strain rate is higher, the temperature increases during forward phase transformation stage and decreases during reverse phase transformation. This is due to the predominant role of latent heat compared with other heat sources. Also, the difference between maximum and initial temperature becomes more distinct when the strain rate is higher. At a large strain rate of $3 \times 10^{-1}\mathrm{s}^{-1}$, the heat convection is insufficient and the finish temperature is higher than the initial temperature. According to Eq. (32), the back force term $\mu(\theta - \theta_0)$ in the driving force increases during phase transformation due to the increase of temperature θ, similarly as kinematic hardening. As a result, a larger stress is needed to continue the phase transformation. It is consistent with the results in Fig. 12(c). To reach the same volume fraction of martensite in forward transformation, a higher stress

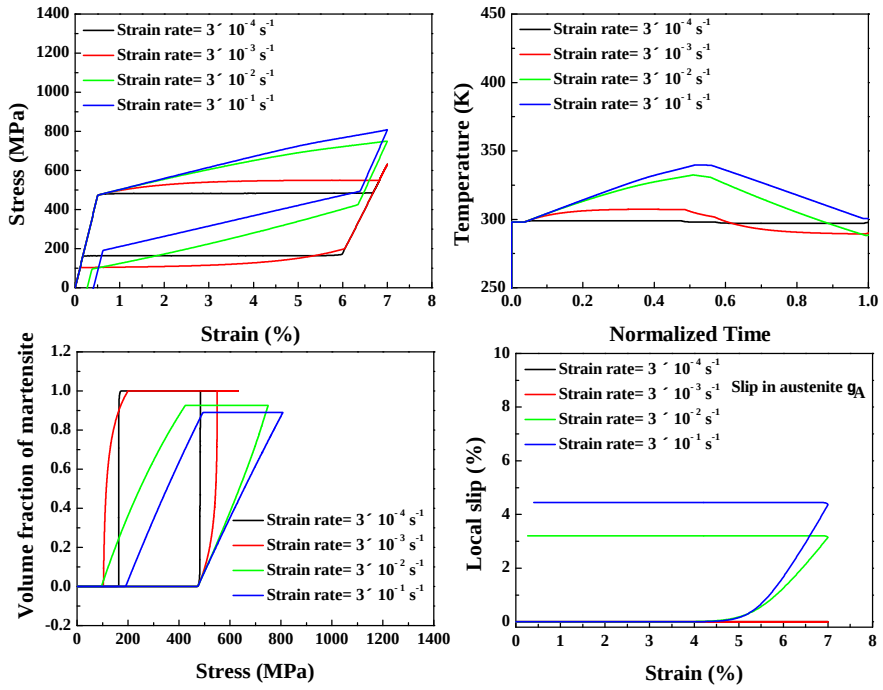

Figure 12 Simulated responses of a single crystal in uniaxial tension tested at 298 K and 7% strain with different loading rates. (a) Macrostress-macrostrain response; (b) Evolution of temperature with normalized time; (c) Evolution of martensite volume fraction with macrostress; (d) Evolution of local deformation activity with macrostrain.

is required for the curves of larger strain rates. Besides, phase transformation becomes incomplete at higher strain rates. The stress increases during forward transformation stage and when it reaches the yield stress of austenite, slip deformation is activated. In Fig. 12(d), the local slip in austenite starts around 4.5% and accumulated until the end of loading. The thermomechanical coupling strongly affects the fatigue behavior of shape memory alloys. Without involving thermomechanical coupling, the accuracy of fatigue prediction from the model will be hampered (Moumni et al., 2005). Thus, in the present work, the coupling effect is taken into account for further fatigue study.

6. Results of the cyclic deformation using the generalization cyclic model

Similar to the basic model, a solid cube CUB8 is used for testing the generalized model under the boundary condition shown in Fig. 1. This section is divided into two parts. In the first part (Section 6.1), the generalized model is calibrated to the reported data in (Gall

and Maier, 2002) and is used to reproduce the anisotropic cyclic deformation of single NiTi SMA with various crystallographic orientations. Since the experiments in (Gall and Maier, 2002) are conducted under small strain amplitudes, some of the inelastic mechanisms are not activated. Thus, in the second part (Section 6.2), a series of tests at different loading conditions are presented to comprehensively verify the generalized cyclic model.

6.1. Comparison with experimental results from literature

Table 5

Material parameters calibrated for cyclic deformation of pseudoelastic NiTi single crystal.

Elastic constants
$\mathbb{C}_A^{11} = 130$ GPa, $\mathbb{C}_A^{22} = 98$ GPa, $\mathbb{C}_A^{44} = 34$ GPa, $\mathbb{C}_M = \frac{1}{2}\mathbb{C}_A$
Plastic parameters for austenite slip
$\dot{\gamma}_A^0 = 0.002\ \mathrm{s}^{-1}$, $m_A = 0.02$, $g_A^\infty = 900$ MPa, $a_A = 0.125$, $q_A = 1.4$, $h_1 = 1200$ MPa, $h_2 = 1600$ MPa,
$h_3 = 10$ MPa, $g_A^0\big\vert_{<100>\{010\}} = 700$ MPa, $g_A^0\big\vert_{<100>\{011\}} = 350$ MPa, $g_A^0\big\vert_{<111>\{100\}} = 280$ MPa
Plastic parameters for TRIP
$\gamma_{sat} = 0.008$, $B_{sat} = 10000$, $b_1 = 0.7$, $b_2 = 1.33$
Phase transformation parameters
$M_s = 247$ K, $g_{tr} = 0.1308$, $\mu = 0.52$ MPa/K, $G^0 = 21.97$ MPa, $G^{sat} = 77.29$ MPa, $\beta = 0$ MPa,
$f_{c\_0} = 9.37$ MPa, $f_{c\_sat} = 2.63$ MPa, $\xi_{ua}^{sat} = 0$, $\xi_{rm}^{sat} = 0$, $b_3 = 1$, $b_4 = 1$, $b_5 = 2.59$, $b_6 = 1.26$

Table 6

Experimental and predicted residual strain of single NiTi SMA in different crystallographic orientations at 100th cycle ((Gall and Maier, 2002)).

	Permanent strain at 100th cycle					
Crystallographic orientations	[2 1 0]	[1 1 1]	[3 2 1]	[2 1 1]	[2 2 1]	[1 1 0]
Experiment (%)	0.98	2.42	2.39	3.19	2.19	2.35
Prediction (%)	1.09	2.30	2.28	1.71	2.46	2.36

The parameters used here are determined from the experimental data in the work of Gall and Maier (2002). The determination process are explained in appendix C and the parameters values are listed in Table 5. It should be mentioned that the simulation tests are conducted under strain control to a maximum strain of about 3% and unloaded under load control to a minimum stress of about 20 MPa according to Gall and Maier (2002). Besides, the duration of loading and unloading stage is set as 30 kinematic time as reported.

The experimental and simulation mechanical responses of NiTi single crystal in [2 1 0] orientation at different loading cycles are shown in Fig. 13 as the solid and dash-dot lines, respectively. It can be seen that the main characteristics of the cyclic deformation are captured. Fig. 14 shows the comparison of the experimental and simulation results in [1 1 1] sample. As presented by the experimental curves (solid lines), the hysteresis loop occurs in the first 4 cycles and disappears from the 16th cycle. Such evolution feature is reasonably reproduced by the proposed model as shown in dash-dot lines. The robustness of the present model is further attested by the good agreement of experimental and simulation curves in [3 2 1] orientation where parameters calibrated from [2 1 0] and [1 1 1] curves are used (Fig. 15). Fig. 16 shows the predicted evolution of the permanent strains for these three orientations. The experimental data is also given for comparison in different type of symbols. It can be seen that the evolution shapes of the predicted permanent strains are very close to those of the experimental ones. The values of the residual strains after 100 cycles in various orientations are listed in Table 6.

In addition to the three orientations mentioned above, the permanent strains at 100th cycle in three other orientations ([2 1 1], [2 2 1] and [1 1 0]) are also listed in Table 6. Except [2 1 1], the predicted permanent strains of the other orientations fit well with the experimental data. The corresponding simulated cyclic stress-strain curves are shown in Fig. 17. No experimental curves are provided here for comparison because of the absence of mechanical curves of these three orientations in the work of Gall and Maier (2002).

6.2. Model verification under various loading conditions

6.2.1. Cyclic loading at large strain amplitudes

Fig. 18 shows the the simulated cyclic responses of [1 1 1] orientated NiTi single crystal tested under large strain amplitude. The parameters used are listed in Table 7. It should be noted that the ξ_{ua}^{sat} and ξ_{rm}^{sat} are set to zero in this case for simplification. The occurrence of plastic deformation is observed after the complete martensitic transformation at large strain in Fig. 18(a). Such inelastic deformation is mainly attributed to the deformation twinning in martensite as shown in Fig. 18(c) and (d). Moreover, the curve presents a

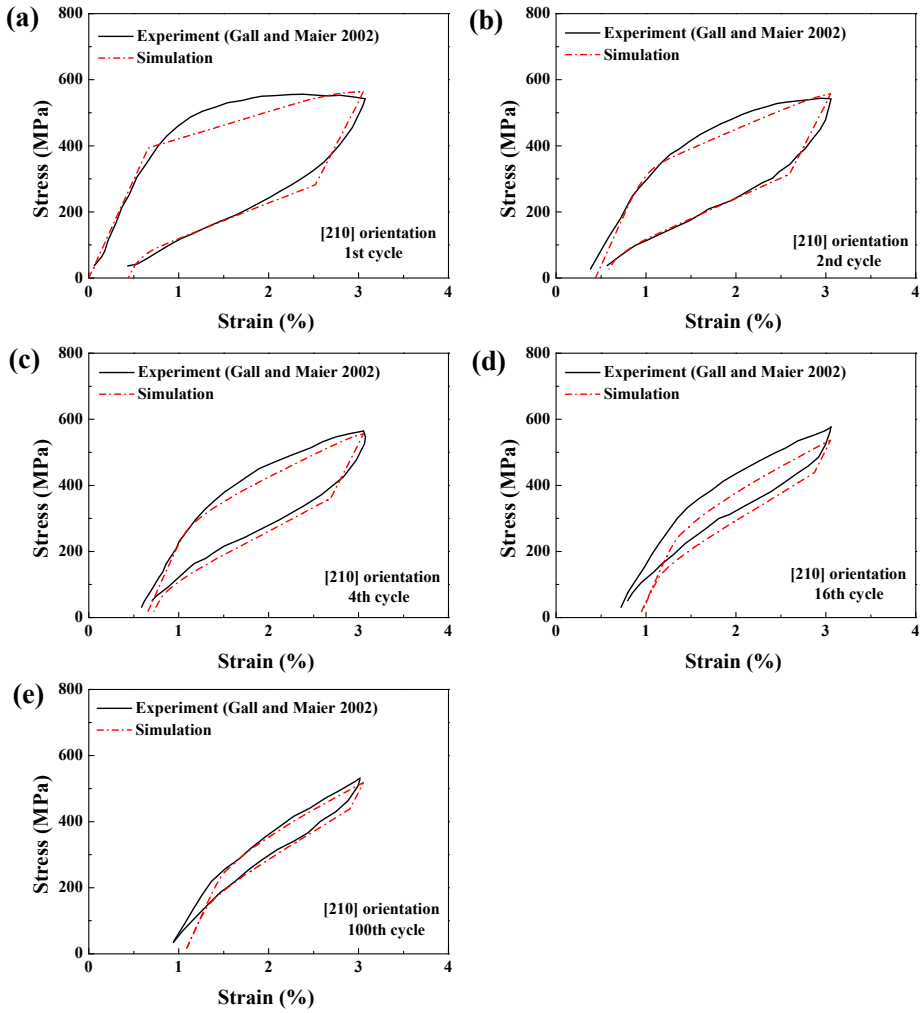

Figure 13 Simulated mechanical responses of single NiTi SMAs oriented along [2 1 0] direction at different cycles: (a) 1st cycle; (b) 2nd cycle; (c) 4th cycle; (d) 16th cycle; (e) 100th cycle. The experimental results from Gall and Maier (2002) are also plotted by solid lines in the figures for comparison (Here, the absolute values of macrostress and macrostrain are used).

pure transformation hysteresis without deformation twinning after the first cycle, which is consistent with the experimental observation of cyclic behavior of pseudoelastic NiTi under large strain (Wang et al., 2008a). The evolution of martensite volume fraction is plotted in Fig. 18(b). It can be seen that the reverse transformation is not completely finished as shown in the enlarged figure. This is due to the existence of highly deformed martensite at large strain, which can not fully transform back to austenite (Sehitoglu et al., 2000).

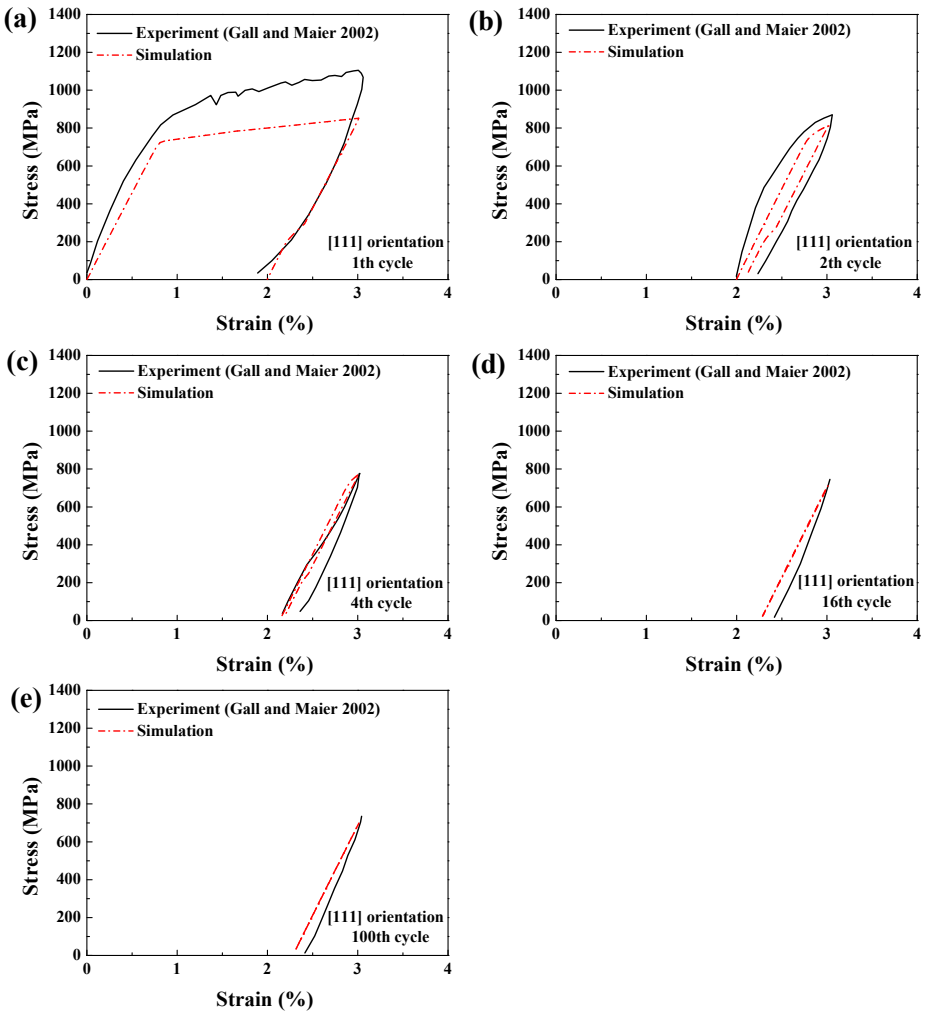

Figure 14 Simulated mechanical responses of single NiTi SMAs oriented along [1 1 1] direction at different cycles: (a) 1st cycle; (b) 2nd cycle; (c) 4th cycle; (d) 16th cycle; (e) 100th cycle. The experimental results from Gall and Maier (2002) are also plotted by solid lines in the figures for comparison (Here, the absolute values of macrostress and macrostrain are used).

6.2.2. Effect of thermomechanical coupling on cyclic deformation behavior

In order to verify the thermomechanical coupling effect on the cyclic deformation of NiTi single crystal, a simulation test is conducted in [2 1 0] orientation under the same loading condition as Section 6.1, but with a higher strain rate of 1 $\times 10^{-1}\mathrm{s}^{-1}$. The corresponding mechanical and thermal responses are shown in Fig. 19 and 20, respectively. Compared with the mechanical responses at a low strain rate of 1 $\times 10^{-3}\mathrm{s}^{-1}$ (Fig. 13), a higher peak stress and larger residual strain are observed in Fig. 19. Moreover, the start stress of forward

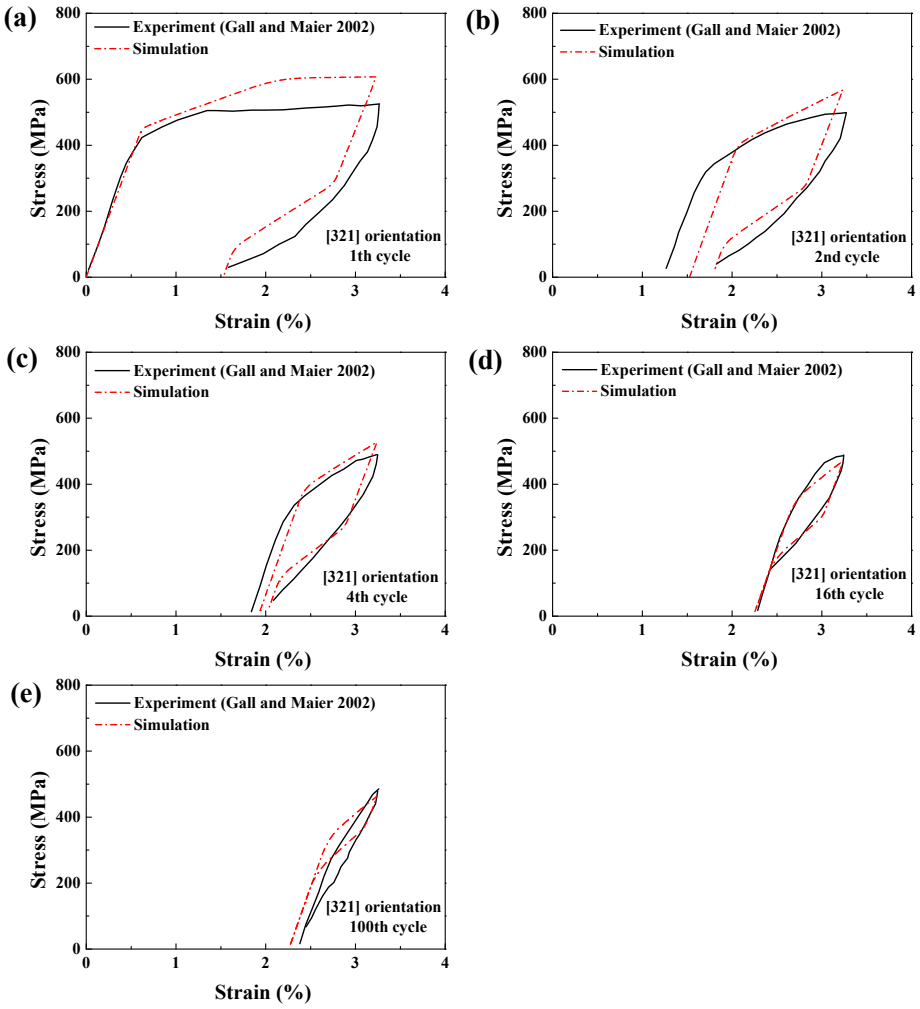

Figure 15 Simulated mechanical responses of single NiTi SMAs oriented along [3 2 1] direction at different cycles: (a) 1st cycle; (b) 2nd cycle; (c) 4th cycle; (d) 16th cycle; (e) 100th cycle. The experimental results from Gall and Maier (2002) are also plotted by solid lines in the figures for comparison (Here, the absolute values of macrostress and macrostrain are used).

transformation for each cycle is higher in the high-strain-rate test.

Fig. 20 plots the thermal responses of tests at different strain rates. The periodical temperature evolution is attributed to the mechanical dissipation and latent heat associated with phase transformation. At a low strain rate (Fig. 20(a)), the mean temperature decreases a little bit at the first five cycles and then tends to stabilize at 298 K. However, at a high strain rate (Fig. 20(b)), the mean temperature increases at the first two cycles and keeps rising to 308 K. Comparing Fig. 20(a) and (b), it can be seen that the mean

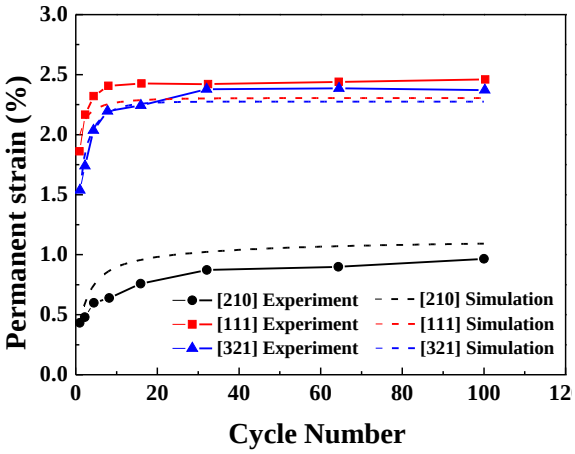

Figure 16 Experimental and predicted evolution of the permanent strains for the [2 1 0], [1 1 1] and [3 2 1] orientation samples.

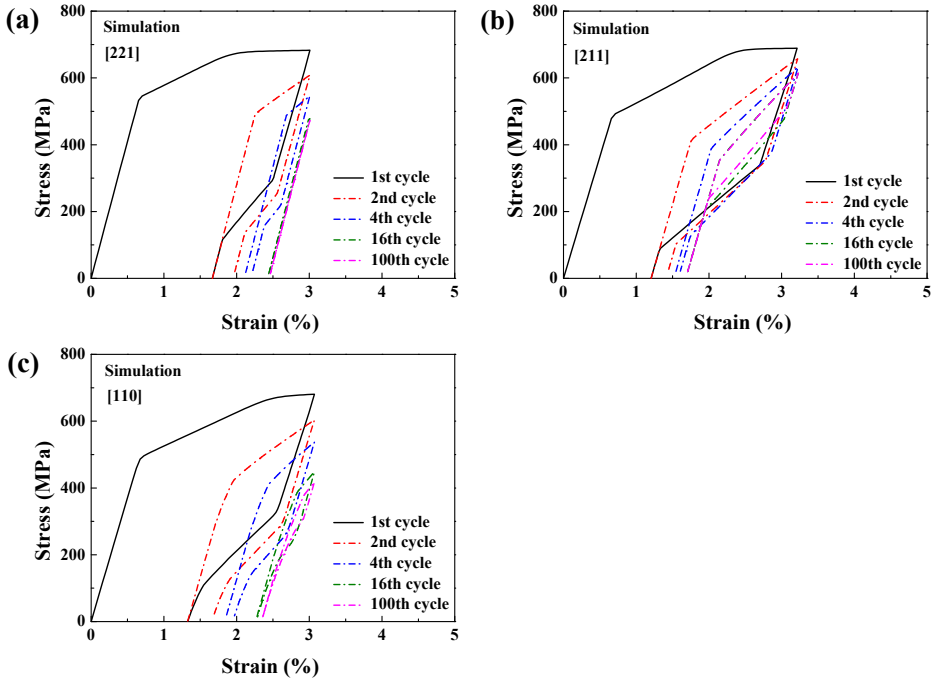

Figure 17 Simulated cyclic mechanical responses in uniaxial compression for single NiTi SMAs oriented along different directions. (a) [2 2 1]; (b) [2 1 1]; (c) [1 1 0] (Here, the absolute values of macrostress and macrostrain are used).

Table 7

Material parameters used for generalized cyclic model verification.

Plastic parameters for TRIP
$\gamma_{sat} = 0.003$ (for the large strain amplitude test), $\gamma_{sat} = 0.01$ (for the effect of UA and RM test)
$b_1 = 0.7$, $b_2 = 1.33$
Phase transformation parameters
$M_s = 251.3$ K, $g_{tr} = 0.1308$, $\mu = 0.54$ MPa/K , $G^0 = 2$ MPa, $G^{sat} = 5$ MPa, $\beta = 0$ MPa
$f_{c\_0} = 8.1$ MPa, $f_{c\_sat} = 5$ MPa, $\xi_{ua}^{sat} = 0$, $\xi_{rm}^{sat} = 0$ (for the large strain amplitude test)
$\xi_{ua}^{sat} = 0.02$, $\xi_{rm}^{sat} = 0.05$ (for the effect of UA and RM test), $b_3 = 6$, $b_4 = 6$, $b_5 = 6$, $b_6 = 6$
Dislocation density realted parameters
ρ_0=1×10^{14} m^{-2}, $c_1 = c_3 = 1.7 \times 10^8$ m^{-1}, $c_2 = c_4 = 1.9 \times 10^{-9}$ m

Notes: The values for elastic constants, plastic parameters for austenite slip and plastic parameters for martensite twinning are the same as those listed in Table 3 and not listed here for clarity.

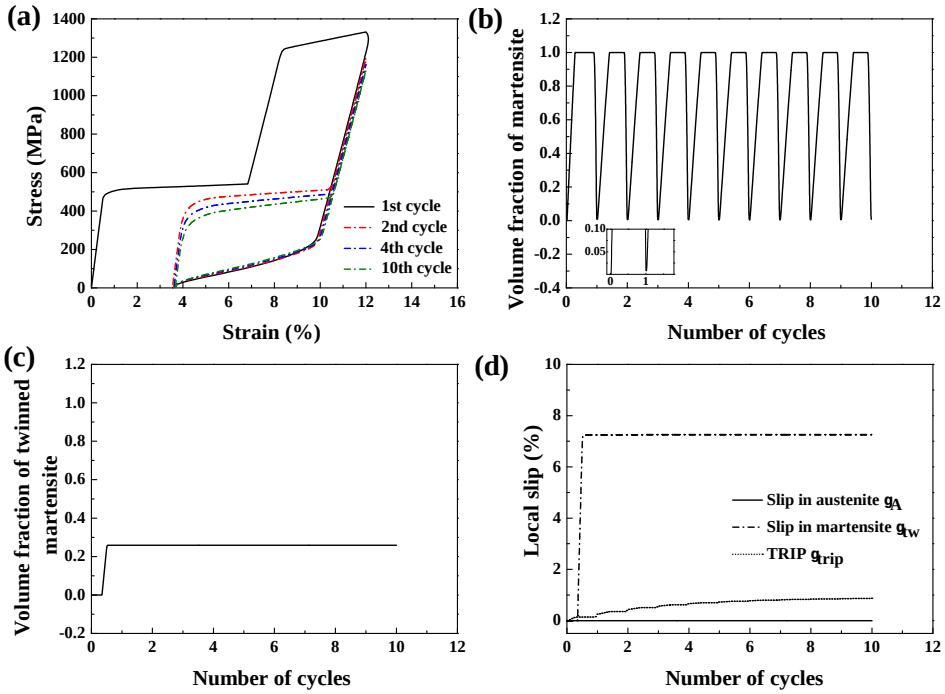

Figure 18 Simulated responses in uniaxial tension for single NiTi SMAs in [1 1 1] orientation tested at 12% strain: (a) Macrostress-macrostrain response; (b) Evolution of martensite volume fraction with loading cycles; (c) Evolution of twinned martensite volume fraction with loading cycles; (d) Evolution of local deformation activity with loading cycles.

744 temperature is higher for high strain rate, which explains the difference in transformation
745 start stresses under two different strain rates conditions.

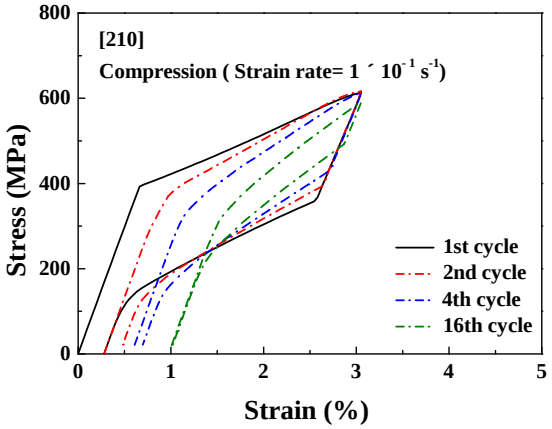

Figure 19 Simulated cyclic responses in uniaxial compression for single NiTi SMAs in [2 1 0] orientation tested at a high strain rate of $1 \times 10^{-1} s^{-1}$ (Here, the absolute values of macrostress and macrostrain are used).

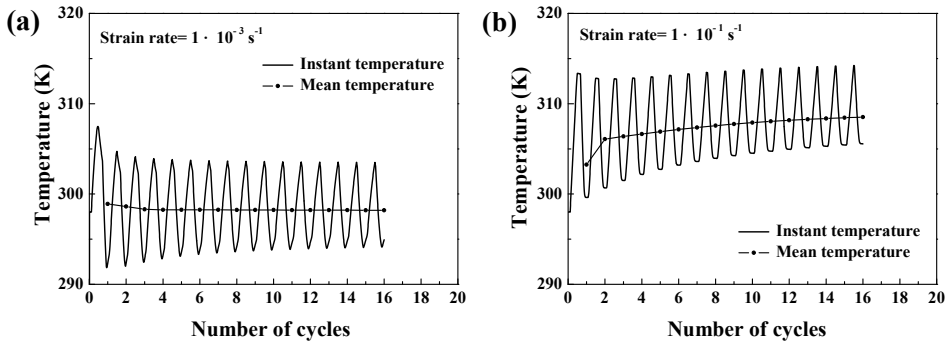

Figure 20 Simulated thermal responses of single NiTi SMAs in [2 1 0] orientation tested at different strain rates: (a) $1 \times 10^{-3} s^{-1}$; (b) $1 \times 10^{-1} s^{-1}$ (Take the mean temperature as the average of temperature in one cycle).

6.2.3. Effect of UA and RM

In this section, the single NiTi in [1 1 1] orientation experiences a cyclic tension-unloading deformation under stress control to a peak stress of 800 MPa. The peak stress is chosen to ensure the fully transformation for studying the effect of UA and RM on the mechanical responses. The parameters used are listed in Table 7. The predicted cyclic mechanical curves are plotted in Fig. 21(a). Fig. 21(b) shows the evolution of martensite volume fraction with loading cycles. It can be seen that the maximum ξ after forward transformation never reaches 1 and decreases with the increase of loading cycles, as marked by red dash lines. Besides, the minimum ξ at the end of unloading never returns back to zero and increases during the

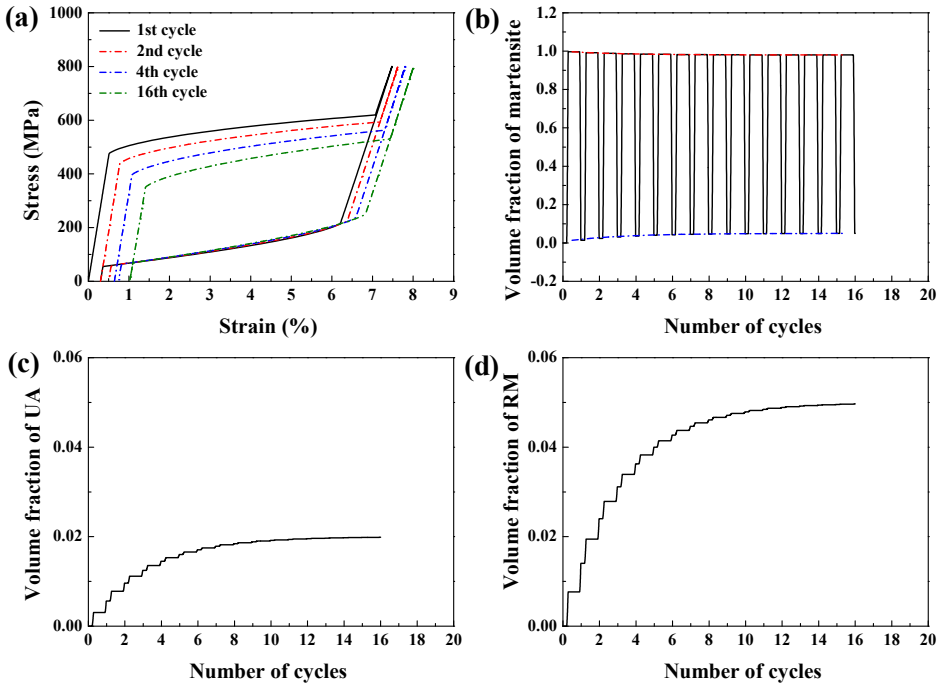

Figure 21 Simulated responses in uniaxial tension for single NiTi SMAs in [1 1 1] orientation tested under stress control to a maximum stress of 800 MPa: (a) Macrostress-macrostrain response; (b) Evolution of martensite volume fraction with loading cycles; (c) Evolution of UA volume fraction with loading cycles; (d) Evolution of RM volume fraction with loading cycles.

cyclic deformation, as marked by blue dash lines. Such incomplete phase transformation is due to the introduction of internal variables ξ_{ua} and ξ_{rm}. As shown in Fig. 21(c) and (d), the volume fraction of UA and RM increases with the loading cycles and tends to stabilized when reaching the saturation value of 0.02 and 0.05, respectively.

6.2.4. Evolution of dislocation density and corresponding stored energy

The predicted evolution curves of dislocation density and stored energy in the stress controlled test mentioned in Section 6.2.3 are shown in Fig. 22. It can be seen that the dislocation density increases at the first few cycles and barely changes after 12 cycles. Similar evolution curves are reported in the simulation work of Yu et al. (2015a) and the experimental work of Zotov et al. (2017). Fig. 22(b) shows the evolution curve of corresponding stored energy. It presents the same trend as the evolution curve of dislocation density. It should be noted that the curves here only represent the qualitative evolution characteristics due

to the lack of the experimental results. Subsequent work is needed in the experimental measurement of dislocation density and stored energy in NiTi SMAs.

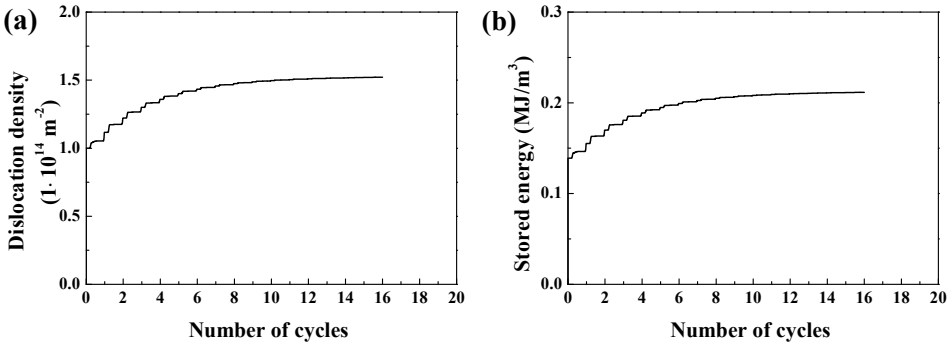

Figure 22 Simulated evolution of: (a) Dislocation density; (b) Corresponding stored energy.

7. Conclusions

A crystal plasticity-based constitutive model is developed in a finite strain framework to describe the thermomechanical behavior of pseudoelastic NiTi single cyrstal. For the first time, the model takes into account all physical mechanisms which affects the fatigue behavior of NiTi SMAs: martensite transformation, deformation slip in austenite at high temperature, deformation twinning in martensite at large strain, TRIP as well as thermomechanical coupling. Subsequently, new internal variables and evolution laws are introduced in order to reproduce the main features of anisotropic cyclic deformation of pseudoelastic NiTi single crystal. The basic and generalized cyclic constitutive models are implemented into CAST3M (2019) and verified through simulations under different temperatures, strain amplitudes, crystallographic orientations, loading directions and strain rates. The effect of temperature and strain amplitude on thermo-mechanical responses are qualitatively captured. Besides, it is worth noted that the features of cyclic performance of NiTi SMAs under large strain amplitude with deformation twinning involved are also reproduced. TRIP is observed when forward transformation starts and remains unchanged after reverse transformation finishes. Moreover, the tension-compression asymmetry in pseudoelastic response

originated from the differences of activated transformation systems in tension and compression is predicted. The features concerning the thermomechanical coupling, i.e. increase of the residual strain and transformation slope with strain rate are captured through the simulation tests under different strain rates. Furthermore, the model is verified by predicting the experimental results reported by (Gall et al., 2002) and (Gall and Maier, 2002). The characteristics of crystallographic orientation effect and anisotropic cyclic deformation behavior are well reproduced. A quantitatively good fit of the simulation and experimental data is observed since the physical mechanisms of cyclic performance are all considered. Finally, the evolution of dislocation density and stored energy is discussed in this work from the perspective of fatigue analysis of SMAs.

8. Acknowledgement

The author Xiaofei JU would like to acknowledge CSC (China Scholarship Council) for their financial support.

Appendix A : time-integration procedure

In this appendix, the numerical integration procedure is presented. Firstly, a detailed procedure is given in Table 8 and 9 for the basic model. Since the time-integration procedure for the generalized cyclic model is similar to that of the basic model with some differences, only the modified part are listed in Table 10 for the generalized cyclic model.

Appendix B : determination of transformation related parameters

The forward phase transformation starts at the point σ_1^1 for the first cycle in Fig. 2. At this point, the internal stress triggered by phase transformation is equal to zero ($\boldsymbol{B}_{int} = 0$). According to the consistency condition (Eq. (51)), the transformation condition at the point σ_1^1 can be written as:

$$g_{tr}\boldsymbol{\sigma}_1^1 : \boldsymbol{S}_{tr}{}^{(i)} - \mu(\theta - M_s) = 0 \tag{94}$$

Table 8

Time-integration procedure for the basic model

Step 1: calculate the trail Elastic Green strain $\boldsymbol{E}_e(\tau)^{trial}$

$\boldsymbol{F}_e(\tau)^{trial} = \boldsymbol{F}(\tau)\boldsymbol{F}_{inel}(t)^{-1}$, $\boldsymbol{A}(\tau)^{trial} = (\boldsymbol{F}_e(\tau)^{trial})^T\boldsymbol{F}_e(\tau)^{trial}$, $\boldsymbol{E}_e(\tau)^{trial} = \frac{1}{2}(\boldsymbol{A}(\tau)^{trial} - \boldsymbol{I})$

Step 2: calculate the effective elastic moduli $\mathbb{C}(t)$

$\mathbb{C}(t) = (1-\xi(t))\mathbb{C}_A + \xi(t)\mathbb{C}_M$

Step 3: calculate the trial second Piola-Kirchoff stress $\boldsymbol{T}(\tau)^{trial}$ and Mandel stress $\boldsymbol{M}(\tau)^{trial}$

$\boldsymbol{T}(\tau)^{trial} = \mathbb{C}(t) : \boldsymbol{E}_e(\tau)^{trial}$, $\boldsymbol{M}(\tau)^{trial} = \boldsymbol{A}(\tau)^{trial}\boldsymbol{T}(\tau)^{trial}$

Step 4: calculate the trial resolved shear stresses for slip and twinning deformation

$\tau_A{}^{(\alpha)}(\tau)^{trial} = \boldsymbol{M}(\tau)^{trial} : \boldsymbol{S}_p{}^{(\alpha)}$, $\tau_{tr}{}^{(i)}(\tau)^{trial} = (\boldsymbol{M}(\tau)^{trial} + \boldsymbol{B}_{int}(t)) : \boldsymbol{S}_{tr}{}^{(i)}$

$\tau_{tw}{}^{(t)}(\tau)^{trial} = \boldsymbol{M}(\tau)^{trial} : \boldsymbol{S}_{tw}{}^{(t)}$, $\tau_{trip}{}^{(\alpha)}(\tau)^{trial} = (\boldsymbol{M}(\tau)^{trial} + \boldsymbol{B}_{int}(t)) : \boldsymbol{S}_p{}^{(\alpha)}$

Step 5: calculate the trial driving force for each mechanism:

$f_{tr}^{(i)}(\tau)^{trial} = g_{tr}\tau_{tr}{}^{(i)}(\tau)^{trial} - \frac{1}{2}\boldsymbol{E}_e : \Delta\mathbb{C}(t) : \boldsymbol{E}_e - \mu(\theta(t)-\theta_0) - G\xi(t) - \frac{1}{2}\beta g_{tr}(1-2\xi(t))$

$f_A^{(\alpha)}(\tau)^{trial} = |\tau_A{}^{(\alpha)}(\tau)^{trial}| - g_A^{(\alpha)}(t)$, $f_{tw}^{(t)}(\tau)^{trial} = \tau_{tw}{}^{(t)}(\tau)^{trial} - g_{tw}^{(t)}(t)$, $f_{trip}^{(\alpha)}(\tau)^{trial} = \tau_{trip}{}^{(\alpha)}(\tau)^{trial}$

Step 6: calculate $\Delta\gamma_A^{(\alpha)}(\tau)$, $\Delta\gamma_{tw}^{(t)}(\tau)$, $\Delta\xi^{(i)}(\tau)$ and $\Delta\gamma_{trip}^{(\alpha)}(\tau)$. (A detailed procedure is shown afterwards.)

Step 7: renew $\xi^{(i)}(\tau)$, $\xi(\tau)$ and $\xi_c(\tau)$

$\xi^{(i)}(\tau) = \xi^{(i)}(t) + \Delta\xi^{(i)}(\tau)$, $\xi(\tau) = \sum_{i=1}^{24}\xi^{(i)}(\tau)$, $\xi_c(\tau) = \xi_c(t) + \sum_{i=1}^{24}|\Delta\xi^{(i)}(\tau)|$

Step 8: calculate the temperature change $\Delta\theta(\tau)$

$$\Delta F_{MD}(\tau) = \sum_{i=1}^{24} f_{tr}^{(i)}(\tau)^{trial}\Delta\xi^{(i)}(\tau) + (1-\xi(\tau))\sum_{\alpha=1}^{24} f_A^{(\alpha)}(\tau)^{trial}\Delta\gamma_A^{(\alpha)}(\tau) + \xi(\tau)\sum_{t=1}^{11} f_{tw}^{(t)}(\tau)^{trial}\Delta\gamma_{tw}^{(t)}(\tau) + (1-\xi(\tau))\sum_{\alpha=1}^{24} f_{trip}^{(\alpha)}(\tau)^{trial}\Delta\gamma_{trip}^{(\alpha)}(\tau)$$

$$\Delta F_{LT}(\tau) = \theta(t)\mu\sum_{i=1}^{24}\Delta\xi^{(i)}(\tau), \quad C\Delta\theta(\tau) = \frac{\sum_{i=1}^{n} V_i\Delta F_{MD}(\tau)}{\sum_{i=1}^{n} V_i} + \frac{\sum_{i=1}^{n} V_i\Delta F_{LT}(\tau)}{\sum_{i=1}^{n} V_i} - \frac{h(\theta(t)+\Delta\theta(\tau)-\theta_r)\cdot S_\Omega}{V_\Omega}$$

Step 9: calculate and normalize inelastic deformation gradient $\boldsymbol{F}_{inel}(\tau)$

$$\boldsymbol{F}_{inel}(\tau) = [1 + (1-\xi(\tau))\sum_{\alpha=1}^{24}\Delta\gamma_A^{(\alpha)}(\tau)\boldsymbol{S}_p{}^{(\alpha)} + \sum_{i=1}^{24}\Delta\xi^{(i)}(\tau)g_{tr}\boldsymbol{S}_{tr}{}^{(i)} + \xi(\tau)\sum_{t=1}^{11}\Delta\gamma_{tw}^{(t)}(\tau)\boldsymbol{S}_{tw}{}^{(t)} + (1-\xi(\tau))\sum_{\alpha=1}^{24}\Delta\gamma_{trip}^{(\alpha)}(\tau)\boldsymbol{S}_p{}^{(\alpha)}]\boldsymbol{F}_{inel}(t)$$

$$\boldsymbol{J}_{inel} = det(\boldsymbol{F}_{inel}(\tau)), \quad \boldsymbol{F}_{inel}(\tau) = \boldsymbol{J}_{inel}^{-\frac{1}{3}}\boldsymbol{F}_{inel}(\tau)$$

Step 10: update $\mathbb{C}(\tau)$

$\mathbb{C}(\tau) = (1-\xi(\tau))\mathbb{C}_A + \xi(t)\mathbb{C}_M$

Step 11: compute $\boldsymbol{F}_e(\tau)$,$\boldsymbol{T}_e(\tau)$ and $\boldsymbol{\sigma}(\tau)$

$$\boldsymbol{F}_e(\tau) = \boldsymbol{F}(\tau)\boldsymbol{F}_{inel}(\tau)^{-1}, \quad \boldsymbol{T}(\tau) = \mathbb{C}(\tau) : \boldsymbol{E}_e(\tau) = \mathbb{C}(\tau) : \frac{1}{2}(\boldsymbol{F}_e(\tau)^T\boldsymbol{F}_e(\tau) - \boldsymbol{I})$$

$$\boldsymbol{\sigma} = \frac{1}{det(\boldsymbol{F}_e(\tau))}\boldsymbol{F}_e(\tau)\boldsymbol{T}(\tau)(\boldsymbol{F}_e(\tau))^T$$

Step 12: renew a group of internal variables

$$\gamma_A^{(\alpha)}(\tau) = \gamma_A^{(\alpha)}(t) + |\Delta\gamma_A^{(\alpha)}(\tau)|, \quad \gamma_{tw}^{(t)}(\tau) = \gamma_{tw}^{(t)}(t) + |\Delta\gamma_{tw}^{(t)}(\tau)|, \quad \gamma_{trip}^{(\alpha)}(\tau) = \gamma_{trip}^{(\alpha)}(t) + |\Delta\gamma_{trip}^{(\alpha)}(\tau)|$$

$$\tau_A{}^{(\alpha)}(\tau) = \boldsymbol{F}_e(\tau)(\boldsymbol{F}_e(\tau))^T\boldsymbol{T}(\tau) : \boldsymbol{S}_p{}^{(\alpha)}, \quad \tau_{tw}{}^{(t)}(\tau) = \boldsymbol{F}_e(\tau)(\boldsymbol{F}_e(\tau))^T\boldsymbol{T}(\tau) : \boldsymbol{S}_{tw}{}^{(t)}$$

$$g_A^{(\alpha)}(\tau) = g_A^{(\alpha)}(t) + \sum_{\beta=1}^{24} h_A^{\alpha\beta}\left|\Delta\gamma_A^{(\beta)}(\tau)\right|, \quad g_{tw}^{(t)}(\tau) = g_{tw}^{(t)}(t) + \sum_{s=1}^{11} h_{tw}^{ts}\left|\Delta\gamma_{tw}^{(s)}(\tau)\right|$$

$$\boldsymbol{B}_{int}(\tau) = \boldsymbol{B}_{int}(t) + \sum_{i=1}^{24}(\frac{B_{sat}}{b}e^{-\frac{\xi_c(\tau)}{b}}\Delta\xi_c(\tau))\boldsymbol{S}_{tr}^{(i)}, \quad \theta(\tau) = \theta(t) + \Delta\theta(\tau)$$

Table 9

The detailed procedure for Step 6

- Plasticity in austenite

(1) The slip increment is approximated as:
$\Delta\gamma_A^{(\alpha)}(\tau) \approx [(1-\theta_1)\dot{\gamma}_A^{(\alpha)}(t) + \theta_1\dot{\gamma}_A^{(\alpha)}(\tau)]\Delta t$
(θ_1 is a parameter between $[0,1]$. In the present work, θ_1 is taken as 0.5.)

(2) Employing a Taylor expansion:
$\dot{\gamma}_A^{(\alpha)}(\tau) = \dot{\gamma}_A^{(\alpha)}(t) + \left.\frac{\partial\dot{\gamma}_A^{(\alpha)}}{\partial\tau_A^{(\alpha)}}\right|_t \Delta\tau_A^{(\alpha)}(\tau) + \left.\frac{\partial\dot{\gamma}_A^{(\alpha)}}{\partial g_A^{(\alpha)}}\right|_t \Delta g_A^{(\alpha)}(\tau)$

(3) The slip increment is rewritten as:
$\Delta\gamma_A^{(\alpha)}(\tau) = \Delta t(\dot{\gamma}_A^{(\alpha)}(t) + \theta_1 \left.\frac{\partial\dot{\gamma}_A^{(\alpha)}}{\partial\tau_A^{(\alpha)}}\right|_t \Delta\tau_A^{(\alpha)}(\tau) + \theta_1 \left.\frac{\partial\dot{\gamma}_A^{(\alpha)}}{\partial g_A^{(\alpha)}}\right|_t \Delta g_A^{(\alpha)}(\tau))$
Where, $\Delta\tau_A^{(\alpha)}(\tau) = \tau_A^{(\alpha)}(\tau)^{trial} - \tau_A^{(\alpha)}(t)$, $\quad \Delta g_A^{(\alpha)}(\tau) = \sum_{\beta=1}^{24} h_A^{\alpha\beta}\left|\Delta\gamma_A^{(\beta)}(\tau)\right|$

- Phase transformation

(1) Determine the set of potentially active systems $\mathscr{PA}$
  a. For forward transformation, the system belongs to $\mathscr{PA}$ if it satisfies:
  $f_{tr}^{(i)}(\tau)^{trial} - f_c^{(i)} > 0\ , \qquad \xi^{(i)}(t) \in [0,1) \qquad \text{and} \qquad \xi(t) \in [0,1)$
  b. For reverse transformation, the system belongs to $\mathscr{PA}$ if it satisfies:
  $f_{tr}^{(i)}(\tau)^{trial} + f_c^{(i)} < 0\ , \qquad \xi^{(i)}(t) \in (0,1] \qquad \text{and} \qquad \xi(t) \in (0,1]$

(2) Solve a equation set deriving from the consistency conditions: $\sum_{j\in\mathscr{PA}} A^{ij}x^j = b^i\ ,\ i \in \mathscr{PA}$
  a. For the forward phase transformation, it has:
  $A^{ij} = [{g_{tr}}^2\boldsymbol{C}_{trans}^{(j)}(\tau)^{trial} - \sum_{k=1}^{24}(\frac{B_{sat}}{b}e^{-\frac{\xi_c(t)}{b}}\boldsymbol{S}_{tr}^{(k)})] : \boldsymbol{S}_{tr}^{(i)} + G - \beta g_{tr}$
  $b^i = f_{tr}^{(i)}(\tau)^{trial} - f_c^{(i)}$
  $x^i = \Delta\xi^{(i)}(\tau) > 0$
  b. For the reverse phase transformation, it has:
  $A^{ij} = [{g_{tr}}^2\boldsymbol{C}_{trans}^{(j)}(\tau)^{trial} + \sum_{k=1}^{24}(\frac{B_{sat}}{b}e^{-\frac{\xi_c(t)}{b}}\boldsymbol{S}_{tr}^{(k)})] : \boldsymbol{S}_{tr}^{(i)} + G - \beta g_{tr}$
  $b^i = f_{tr}^{(i)}(\tau)^{trial} + f_c^{(i)}$
  $x^i = \Delta\xi^{(i)}(\tau) < 0$

(3) If the solution $\Delta\xi^{(i)}(\tau)$ is negative during forward transformation, this system is inactive and removed from $\mathscr{PA}$. A^{ij} will be recalculated. Similar conduction for reverse transformation (when $\Delta\xi^{(i)}(\tau)$ positive).

(4) Such iterative procedure is continued until all $\Delta\xi^{(i)}(\tau)$ satisfy the requirement.

- TRIP

(1) If $f_{trip}^{(\alpha)}(\tau)^{trial} > 0$, start to calculate $\Delta\gamma_{trip}^{(\alpha)}(\tau)$.
$\Delta\gamma_{trip}^{(\alpha)}(\tau) = \frac{\gamma_{sat}}{b}e^{-\frac{\xi_c(\tau)}{b}}\sum_{i=1}^{24}\left|\Delta\xi^{(i)}(\tau)\right|$

- Plasticity in martensite

The procedure is similar as that of plasticity in austenite mentioned above.

Table 10

Modifications of the time-integration procedure for generalized cyclic model

- The driving force for transformation in Step 5 is rewritten as:

  $f_{tr}^{(i)}(\tau)^{trial} = g_{tr}{\tau_{tr}}^{(i)}(\tau)^{trial} - \frac{1}{2}\boldsymbol{E}_e : \Delta\mathbb{C}(t) : \boldsymbol{E}_e - \mu(\theta(t) - M_s) - G\xi(t) - \frac{1}{2}\beta g_{tr}(1 - 2\xi(t)) + f_c^{(i)}(t)$

- Add calculation of $\Delta\xi_{ua}^{(i)}(\tau)$ and $\Delta\xi_{rm}^{(i)}(\tau)$ and renew of $\xi_{ua}^{(i)}(\tau)$ and $\xi_{rm}^{(i)}(\tau)$ between Step 7 and 8

  $\Delta\xi_{ua}^{(i)}(\tau) = \frac{\xi_{ua}^{sat}}{b_3} e^{-\frac{\xi_c(\tau)}{b_3}} \left|\Delta\xi^{(i)}(\tau)\right|, \quad \Delta\xi_{rm}^{(i)}(\tau) = \frac{\xi_{rm}^{sat}}{b_4} e^{-\frac{\xi_c(\tau)}{b_4}} \left|\Delta\xi^{(i)}(\tau)\right|$

  $\xi_{ua}^{(i)}(\tau) = \xi_{ua}^{(i)}(t) + \Delta\xi_{ua}^{(i)}(\tau), \quad \xi_{rm}^{(i)}(\tau) = \xi_{rm}^{(i)}(t) + \Delta\xi_{rm}^{(i)}(\tau)$

  $\xi_{ua}(\tau) = \sum_{i=1}^{24} \xi_{ua}^{(i)}(\tau), \quad \xi_{rm}(\tau) = \sum_{i=1}^{24} \xi_{rm}^{(i)}(\tau)$

  If $\xi_{ua}(\tau) > \xi_{ua}^{sat}$, set $\xi_{ua}(\tau) = \xi_{ua}^{sat}$. Similar conduction for $\xi_{rm}(\tau)$.

- Renew internal variables of $\boldsymbol{B}_{int}(\tau)$, $f_c(\tau)$ and $G(\tau)$ in Step 13

  $\boldsymbol{B}_{int}(\tau) = \boldsymbol{B}_{int}(t) + \sum_{i=1}^{24} (\frac{B_{sat}}{b_2} e^{-\frac{\xi_c(\tau)}{b_2}} \Delta\xi_c(\tau)) \boldsymbol{S}_{tr}^{(i)}, \quad f_c(\tau) = f_c(t) + \frac{(f_{c\_sat} - f_{c\_0})}{b_5} e^{-\frac{\xi_c(\tau)}{b_5}} \sum_{i=1}^{24} \left|\Delta\xi^{(i)}(\tau)\right|$

  $G(\tau) = G(t) + \frac{(G^{sat} - G^0)}{b_6} e^{-\frac{\xi_c(\tau)}{b_6}} \sum_{i=1}^{24} \left|\Delta\xi^{(i)}(\tau)\right|$

- If $\Delta\xi^{(i)}(\tau) > 0$ and $SF_{plastic}^{(\alpha)} > SF_{critical}$, start to calculate $\Delta\gamma_{trip}^{(\alpha)}(\tau)$.

  $\Delta\gamma_{trip}^{(\alpha)}(\tau) = \frac{\gamma_{sat}}{b_1} e^{-\frac{\xi_c(\tau)}{b_1}} \sum_{i=1}^{24} \left|\Delta\xi^{(i)}(\tau)\right| \mathrm{sign}(f_{trip}^{(\alpha)})$

Thus, the parameter μ is given as:

$$\mu = \frac{g_{tr}\boldsymbol{\sigma}_1^1 : \boldsymbol{S}_{tr}^{(i)}}{\theta - M_s} = \frac{g_{tr}\sigma_1^1 \cdot SF_{tr}^{max}}{\theta - M_s} \tag{95}$$

In the first cycle, the transformation condition at the end of forward transformation and the beginning of reverse transformation can be written as:

$$g_{tr}(\boldsymbol{\sigma}_2^1 + \boldsymbol{B}_{int}\big|_{at\ \boldsymbol{\sigma}_2^1}) : {\boldsymbol{S}_{tr}}^{(i)} - \mu(\theta - M_s) - G\big|_{at\ \boldsymbol{\sigma}_2^1}\xi\big|_{at\ \boldsymbol{\sigma}_2^1} = 0 \tag{96}$$

$$g_{tr}(\boldsymbol{\sigma}_3^1 + \boldsymbol{B}_{int}\big|_{at\ \boldsymbol{\sigma}_3^1}) : {\boldsymbol{S}_{tr}}^{(i)} - \mu(\theta - M_s) - G\big|_{at\ \boldsymbol{\sigma}_3^1}\xi\big|_{at\ \boldsymbol{\sigma}_3^1} = -2f_c\big|_{at\ \boldsymbol{\sigma}_3^1} \tag{97}$$

Since no phase transformation occurs between point σ_2^1 and σ_3^1, it holds $\boldsymbol{B}_{int}\big|_{at\ \boldsymbol{\sigma}_2^1} = \boldsymbol{B}_{int}\big|_{at\ \boldsymbol{\sigma}_3^1}$ and $\xi\big|_{at\ \boldsymbol{\sigma}_2^1} = \xi\big|_{at\ \boldsymbol{\sigma}_3^1}$. Neglecting the change of f_c at the first forward transformation and combining Eq. (96) and (97), it gives the expression for f_{c_0}:

$$f_{c\_0} \approx f_c\big|_{at\ \boldsymbol{\sigma}_3^1} = \frac{1}{2} g_{tr}(\boldsymbol{\sigma}_2^1 - \boldsymbol{\sigma}_3^1) : {\boldsymbol{S}_{tr}}^{(i)} = \frac{1}{2} g_{tr}(\sigma_2^1 - \sigma_3^1) \cdot SF_{tr}^{max} \tag{98}$$

Similarly, in the stabilized cycle, the transformation condition at the end of forward transformation and the beginning of reverse transformation can be written as:

$$g_{tr}(\boldsymbol{\sigma}_2^{sat} + \boldsymbol{B}_{int}\big|_{sat}) : \boldsymbol{S}_{tr}{}^{(i)} - \mu(\theta - M_s) - G\big|_{sat}\xi\big|_{sat} = 0 \tag{99}$$

$$g_{tr}(\boldsymbol{\sigma}_3^{sat} + \boldsymbol{B}_{int}\big|_{sat}) : \boldsymbol{S}_{tr}{}^{(i)} - \mu(\theta - M_s) - G\big|_{sat}\xi\big|_{sat} = -2f_{c\_sat} \tag{100}$$

Combining Eq. (99) and (100), it gives the expression for f_{c_sat}:

$$f_{c\_sat} = \frac{1}{2}g_{tr}(\boldsymbol{\sigma}_2^{sat} - \boldsymbol{\sigma}_3^{sat}) : \boldsymbol{S}_{tr}{}^{(i)} = \frac{1}{2}g_{tr}(\sigma_2^{sat} - \sigma_3^{sat}) \cdot SF_{tr}^{max} \tag{101}$$

The transformation condition at the beginning of forward transformation in the stabilized cycle can be written as:

$$g_{tr}(\boldsymbol{\sigma}_1^{sat} + \boldsymbol{B}_{int}\big|_{sat}) : \boldsymbol{S}_{tr}{}^{(i)} - \mu(\theta - M_s) = 0 \tag{102}$$

Combining Eq. (94) and (102), and considering the definition of $\boldsymbol{B}_{int}$ (Eq. (19)), the parameter B_{sat} can be obtained as:

$$B_{sat} = \frac{(\boldsymbol{\sigma}_1^1 - \boldsymbol{\sigma}_1^{sat}) : \boldsymbol{S}_{tr}{}^{(i)}}{(\sum_{i=1}^{24} \boldsymbol{S}_{tr}{}^{(i)}) : \boldsymbol{S}_{tr}{}^{(i)}} = \frac{(\sigma_1^1 - \sigma_1^{sat}) \cdot SF_{tr}^{max}}{(\sum_{i=1}^{24} \boldsymbol{S}_{tr}{}^{(i)}) : \boldsymbol{S}_{tr}{}^{(i)}} \tag{103}$$

The parameter G is related with the slope of transformation plateau. Thus, combining Eq. (94) and (96), it gives the expression for G^0:

$$G^0 \approx \frac{g_{tr}(\boldsymbol{\sigma}_2^1 - \boldsymbol{\sigma}_1^1) : \boldsymbol{S}_{tr}{}^{(i)} + g_{tr}\boldsymbol{B}_{int}\big|_{at\ \boldsymbol{\sigma}_2^1} : \boldsymbol{S}_{tr}{}^{(i)}}{\xi\big|_{at\ \boldsymbol{\sigma}_2^1}} \approx \frac{g_{tr}(\sigma_2^1 - \sigma_1^1) \cdot SF_{tr}^{max}}{\xi\big|_{at\ \boldsymbol{\sigma}_2^1}} \tag{104}$$

$$\xi\big|_{at\ \boldsymbol{\sigma}_2^1} = \frac{\epsilon_{local}^{tr}\big|_{at\ \boldsymbol{\sigma}_2^1}}{g_{tr}} = \frac{E_{global}^{tr}\big|_{at\ \boldsymbol{\sigma}_2^1}}{g_{tr} \cdot SF_{tr}^{max}} \tag{105}$$

Here, the change of G and $\boldsymbol{B}_{int}$ at the first forward transformation are neglected. The $\xi\big|_{at\ \boldsymbol{\sigma}_2^1}$ is the martensite volume fraction at the end of forward phase transformation in first cycle and is obtained from the global transformation strain E_{global}^{tr}.

Similarly, G^{sat} can be obtained from combining Eq. (102) and (99):

$$G^{sat} = \frac{g_{tr}(\boldsymbol{\sigma}_2^{sat} - \boldsymbol{\sigma}_1^{sat}) : \boldsymbol{S}_{tr}{}^{(i)}}{\xi\big|_{sat}} = \frac{g_{tr}(\sigma_2^{sat} - \sigma_1^{sat}) \cdot SF_{tr}^{max}}{\xi\big|_{sat}} \tag{106}$$

$$\xi\big|_{sat} = \frac{E_{global}^{tr}\big|_{sat}}{g_{tr} \cdot SF_{tr}^{max}} \tag{107}$$

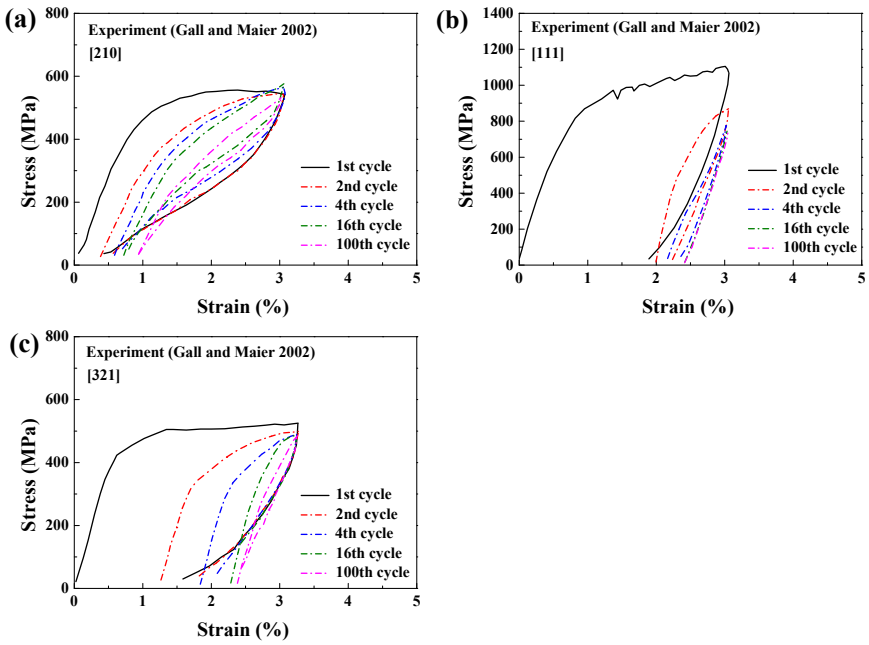

Figure 23 Cyclic mechanical responses in uniaxial compression for solutionized single NiTi SMAs oriented along different directions. (a) [2 1 0]; (b) [1 1 1]; (c) [3 2 1] (Here, the absolute values of macrostress and macrostrain are used).

Appendix C : material calibration for the work of Gall and Maier (2002)

The parameter determination process of fitting the experimental cyclic curves of solutionized NiTi single crystal reported by Gall and Maier (2002) is presented. According to the experimental results (Fig. 23), [2 1 0] orientation exhibits almost perfect pseudoelasticity while predominantly plastic deformation is observed in [1 1 1] orientation. Thus, the phase transformation related parameters are calibrated according to stress-strain curve of [2 1 0] and the [1 1 1] experimental response is used for fitting the plasticity parameters.

(1) Transformation related parameters

In the experiments of Gall and Maier (2002), the testing temperature θ and start temperature of martensite transformation M_s are 298 K and 247 K, respectively. The samples after 100 loading cycles were heated to 373 K to recover the residual strain that attributed to the residual martensite. As a result, the UA and RM are not considered in this case for simplification ($\xi_{ua}^{sat} = \xi_{rm}^{sat} = 0$). Besides, the largest Schmid factor for transformation SF_{max} in [2 1 0] orientation under uniaxial compression test is calculated to be 0.51. From Fig.

Table 11

Calculated Schmid factors for the slip systems in austenite.

Slip modes	n	Slip direction	Slip plane	Schmid factor		
				[2 1 0]	[1 1 1]	[3 2 1]
<1 0 0>{0 1 0}	1	[1 0 0]	(0 1 0)	0.40	0.33	0.14
	2	[1 0 0]	(0 0 1)	0.00	0.33	0.21
	3	[0 0 1]	(1 0 0)	0.00	0.33	0.21
	4	[0 0 1]	(0 1 0)	0.00	0.33	0.43
	5	[0 1 0]	(1 0 0)	0.40	0.33	0.14
	6	[0 1 0]	(0 0 1)	0.00	0.33	0.43
<1 0 0>{0 1 1}	7	[0 1 0]	(1 0 1)	0.28	0.47	0.40
	8	[0 1 0]	(1 0 -1)	0.28	0.00	-0.20
	9	[1 0 0]	(0 1 1)	0.28	0.47	0.25
	10	[1 0 0]	(0 1 -1)	0.28	0.00	0.05
	11	[0 0 1]	(1 1 0)	0.00	0.47	0.45
	12	[0 0 1]	(-1 1 0)	0.00	0.00	0.15
<1 1 1>{1 1 0}	13	[-1 1 1]	(1 1 0)	-0.24	0.27	0.35
	14	[1 -1 1]	(1 1 0)	0.24	0.27	0.17
	15	[-1 1 1]	(1 0 1)	-0.16	0.27	0.47
	16	[1 1 -1]	(1 0 1)	0.49	0.27	0.00
	17	[1 1 -1]	(0 1 1)	0.24	0.27	0.00
	18	[1 -1 1]	(0 1 1)	0.08	0.27	0.29
	19	[1 1 -1]	(-1 1 0)	-0.24	0.00	0.00
	20	[1 1 1]	(-1 1 0)	-0.24	0.00	0.17
	21	[1 1 1]	(-1 0 1)	-0.49	0.00	0.35
	22	[1 -1 1]	(-1 0 1)	-0.16	0.00	0.12
	23	[1 1 1]	(0 -1 1)	-0.24	0.00	0.17
	24	[-1 1 1]	(0 -1 1)	0.08	0.00	0.12

23(a), the start stress for forward transformation in the first cycle σ_1^1 is about 400 MPa. Using Eq. (83), the μ is obtained as 0.52. Similarly, $\{B_{sat},\ f_{c\_0},\ f_{c\_sat},\ G^0,\ G^{sat}\}$ can be obtained from Eq. (84-90) and the values are listed in Table 3.

(2) Plastic parameters

Since the experiments are conducted in the small strain amplitude (maximum stain is about 3%), deformation twinning is not taken into consideration under this circumstance. For uniaxial compression test in [1 1 1] orientation, the SF_{max} is 0.25. Thus, its theoretical start stress for phase transformation in the first cycle σ_1^1 is calculated to be 813 MPa according to Eq. (83). However, the inelastic deformation occurs at around 745 MPa in Fig. 23(b), far below the theoretical σ_1^1 value. As a result, it is reasonable to conclude that the plastic deformation in austenite starts at 745 MPa before the occurrence of phase

transformation at 813 MPa. Tabel 11 lists the calculated Schmid factors for the slip systems in austenite. It can be seen that the largest Schmid factor $SF_{plastic}$ for [1 1 1] orientation is 0.47 in the second slip mode <1 0 0>{0 1 1}. Thus, the initial slip resistance of second slip mode can be calculated from the critical stress of plastic deformation ($g_A^0\big|_{<100>\{011\}} = 350$ MPa). The second largest Schmid factor $SF_{plastic}$ occurs in the first slip mode <1 0 0>{0 1 0} as 0.33. Because of the smaller inter-planar distance of slipping plane in <1 0 0>{0 1 0} than that in <1 0 0>{0 1 0}, the <1 0 0>{0 1 0} slip mode has higher initial slip resistance $g_A^0\big|_{<100>\{010\}}$ (Yu et al., 2015a). Recall the strain hardening matrix $h_A^{\alpha\beta}$ for slip in austenite (Eq. 43), and assume each slip modes has distinct values of the initial hardening coefficient h_A^0 (for $\alpha \in [1,6]$, $h_A^0 = h_1$; for $\alpha \in [7,12]$, $h_A^0 = h_2$; for $\alpha \in [13,24]$, $h_A^0 = h_3$). The value of $g_A^0\big|_{<100>\{010\}}$, h_1 and h_2 are set through fitting the stress-strain curves of [1 1 1] orientation while the value of $g_A^0\big|_{<111>\{110\}}$ and h_3 are determined from the curves of [2 1 0] orientation.

Considering the plastic deformation from austenite slip mainly contributes to the residual strain in the first cycle, the residual strain in the following cyclic loading are attributed to TRIP (Yu et al., 2015a). Thus, the TRIP induced global residual strain $E^{res}_{global}|_{TRIP}$ can be estimated by the difference of residual strain at stabilized cycle and at the end first cycle, eg. ($E^{res}_{global}|_{sat} - E^{res}_{global}|_{at\ 1st\ cycle}$). From Fig. 23(a) and (c), it is seen that the $E^{res}_{global}|_{TRIP}$ in [2 1 0] orientation is about 0.56 %, almost half of that in [3 2 1] orientation (1.13 %). According to Eq. (92), it is clear that the global residual strain contributed from TRIP at stabilized cycle is dependent on the γ_{sat} and $\sum_{\alpha\in\mathscr{B}} SF^{(\alpha)}_{plastic}$. For different orientation, the difference of $E^{res}_{global}|_{TRIP}$ lies in the sum of the Schmid factors for activated slip systems since the value of γ_{sat} is the same. As a result, in order to satisfy the twice difference in $E^{res}_{global}|_{TRIP}$ of the two orientations, the $SF_{critical}$ is chosen as 0.4082 to modify the $\sum_{\alpha\in\mathscr{B}} SF^{(\alpha)}_{plastic}$.

References

Abdolvand, H., Daymond, M. R., and Mareau, C. Incorporation of twinning into a crystal plasticity finite element model: Evolution of lattice strains and texture in zircaloy-2. *International Journal of Plasticity*, 27(11):1721–1738, 2011.

Alkan, S. and Sehitoglu, H. Dislocation core effects on slip response of niti-a key to understanding shape memory. *International Journal of Plasticity*, 97:126–144, 2017.

Alkan, S. and Sehitoglu, H. Prediction of transformation stresses in niti shape memory alloy. *Acta Materialia*, 175:182–195, 2019.

Alkan, S., Wu, Y., and Sehitoglu, H. Giant non-schmid effect in niti. *Extreme Mechanics Letters*, 15:38–43, 2017.

Alkan, S., Ojha, A., and Sehitoglu, H. The complexity of non-schmid behavior in the cuznal shape memory alloy. *Journal of the Mechanics and Physics of Solids*, 114:238–257, 2018.

Anand, L. and Gurtin, M. E. Thermal effects in the superelasticity of crystalline shape-memory materials. *Journal of the Mechanics and Physics of Solids*, 51(6):1015–1058, 2003.

Auricchio, F., Reali, A., and Stefanelli, U. A three-dimensional model describing stress-induced solid phase transformation with permanent inelasticity. *International Journal of plasticity*, 23(2):207–226, 2007.

Borbély, A., Driver, J., and Ungar, T. An x-ray method for the determination of stored energies in texture components of deformed metals; application to cold worked ultra high purity iron. *Acta materialia*, 48 (8):2005–2016, 2000.

Brill, T., Mittelbach, S., Assmus, W., Mullner, M., and Luthi, B. Elastic properties of niti. *Journal of Physics: Condensed Matter*, 3(48):9621, 1991.

Brinson, L. C., Schmidt, I., and Lammering, R. Stress-induced transformation behavior of a polycrystalline niti shape memory alloy: micro and macromechanical investigations via in situ optical microscopy. *Journal of the Mechanics and Physics of Solids*, 52(7):1549–1571, 2004.

Chen, B., Jiang, J., and Dunne, F. P. Is stored energy density the primary meso-scale mechanistic driver for fatigue crack nucleation? *International Journal of Plasticity*, 101:213–229, 2018.

Choi, W. S., Pang, E. L., Ko, W.-S., Jun, H., Bong, H. J., Kirchlechner, C., Raabe, D., and Choi, P.-P. Orientation-dependent plastic deformation mechanisms and competition with stress-induced phase transformation in microscale niti. *Acta Materialia*, 208:116731, 2021.

Chowdhury, P. and Sehitoglu, H. A revisit to atomistic rationale for slip in shape memory alloys. *Progress in Materials Science*, 85:1–42, 2017.

Chumlyakov, Y. I., Surikova, N., and Korotaev, A. Orientation dependence of strength and plasticity of titanium nickelide single crystals. *Physics of metals and metallography*, 82(1):102–109, 1996.

Combescure, A., Hoffmann, A., and Pasquet, P. The castem finite element system. In *Finite Element Systems*, pages 115–125. Springer, 1982.

Delville, R., Malard, B., Pilch, J., Sittner, P., and Schryvers, D. Transmission electron microscopy investigation of dislocation slip during superelastic cycling of ni–ti wires. *International Journal of Plasticity*, 27 (2):282–297, 2011.

Dhala, S., Mishra, S., Tewari, A., and Alankar, A. Modeling of finite deformation of pseudoelastic niti shape memory alloy considering various inelasticity mechanisms. *International Journal of Plasticity*, 115: 216–237, 2019.

Ebrahimi, P., Arghavani, J., Naghdabadi, R., and McGarry, J. P. On the effect of detwinning-induced plasticity in compressive cyclic loading of niti shape memory alloys. *Mechanics of Materials*, 148:103451, 2020.

Eggeler, G., Hornbogen, E., Yawny, A., Heckmann, A., and Wagner, M. Structural and functional fatigue of niti shape memory alloys. *Materials Science and Engineering: A*, 378(1-2):24–33, 2004.

Ezaz, T., Wang, J., Sehitoglu, H., and Maier, H. Plastic deformation of niti shape memory alloys. *Acta Materialia*, 61(1):67–78, 2013.

Gall, K., Juntunen, K., Maier, H., Sehitoglu, H., and Chumlyakov, Y. I. Instrumented micro-indentation of niti shape-memory alloys. *Acta Materialia*, 49(16):3205–3217, 2001.

Gall, K. and Maier, H. Cyclic deformation mechanisms in precipitated niti shape memory alloys. *Acta Materialia*, 50(18):4643–4657, 2002.

Gall, K. and Sehitoglu, H. The role of texture in tension–compression asymmetry in polycrystalline niti. *International Journal of Plasticity*, 15(1):69–92, 1999.

Gall, K., Dunn, M. L., Liu, Y., Labossiere, P., Sehitoglu, H., and Chumlyakov, Y. I. Micro and macro deformation of single crystal niti. *J. Eng. Mater. Technol.*, 124(2):238–245, 2002.

Gloanec, A.-L., Bilotta, G., and Gerland, M. Deformation mechanisms in a tini shape memory alloy during cyclic loading. *Materials Science and Engineering: A*, 564:351–358, 2013.

Grabe, C. and Bruhns, O. T. On the viscous and strain rate dependent behavior of polycrystalline niti. *International Journal of Solids and Structures*, 45(7-8):1876–1895, 2008.

Hazra, S. S., Gazder, A. A., and Pereloma, E. V. Stored energy of a severely deformed interstitial free steel. *Materials Science and Engineering: A*, 524(1-2):158–167, 2009.

He, Y. and Sun, Q. Frequency-dependent temperature evolution in niti shape memory alloy under cyclic loading. *Smart Materials and Structures*, 19(11):115014, 2010.

Heller, L., Seiner, H., Šittner, P., Sedlák, P., Tyc, O., and Kadeřávek, L. On the plastic deformation accompanying cyclic martensitic transformation in thermomechanically loaded niti. *International Journal of Plasticity*, 111:53–71, 2018.

Hodowany, J., Ravichandran, G., Rosakis, A., and Rosakis, P. Partition of plastic work into heat and stored energy in metals. *Experimental mechanics*, 40(2):113–123, 2000.

Hosford, W. F. The mechanics of crystals and textured polycrystals. *Oxford University Press(USA), 1993,*, page 248, 1993.

Hossain, M. and Baxevanis, T. A finite strain thermomechanically-coupled constitutive model for phase

transformation and (transformation-induced) plastic deformation in niti single crystals. *International Journal of Plasticity*, page 102957, 2021.

Jani, J. M., Leary, M., Subic, A., and Gibson, M. A. A review of shape memory alloy research, applications and opportunities. *Materials & Design (1980-2015)*, 56:1078–1113, 2014.

Kajiwara, S. and Kikuchi, T. Dislocation structures produced by reverse martensitic transformation in a cu zn alloy. *Acta Metallurgica*, 30(2):589–598, 1982.

Kajiware, S. and Owen, W. Substructure of austenite formed by a partial reverse martensitic transformation in an fe-pt alloy. *Metallurgical Transactions*, 4(8):1988–1990, 1973.

Kalidindi, S. R. Incorporation of deformation twinning in crystal plasticity models. *Journal of the Mechanics and Physics of Solids*, 46(2):267–290, 1998.

Kan, Q. and Kang, G. Constitutive model for uniaxial transformation ratchetting of super-elastic niti shape memory alloy at room temperature. *International Journal of Plasticity*, 26(3):441–465, 2010.

Kang, G., Kan, Q., Qian, L., and Liu, Y. Ratchetting deformation of super-elastic and shape-memory niti alloys. *Mechanics of Materials*, 41(2):139–153, 2009.

Karaman, I., Yapici, G., Chumlyakov, Y., and Kireeva, I. Deformation twinning in difficult-to-work alloys during severe plastic deformation. *Materials Science and Engineering: A*, 410:243–247, 2005.

Kato, H. and Sasaki, K. Transformation-induced plasticity as the origin of serrated flow in an niti shape memory alloy. *International Journal of Plasticity*, 50:37–48, 2013.

Kudoh, Y., Tokonami, M., Miyazaki, S., and Otsuka, K. Crystal structure of the martensite in ti-49.2 at.% ni alloy analyzed by the single crystal x-ray diffraction method. *Acta Metallurgica*, 33(11):2049–2056, 1985.

Lagoudas, D., Hartl, D., Chemisky, Y., Machado, L., and Popov, P. Constitutive model for the numerical analysis of phase transformation in polycrystalline shape memory alloys. *International Journal of Plasticity*, 32:155–183, 2012.

Lagoudas, D. C. and Entchev, P. B. Modeling of transformation-induced plasticity and its effect on the behavior of porous shape memory alloys. part i: constitutive model for fully dense smas. *Mechanics of Materials*, 36(9):865–892, 2004.

Lan, Y., Xiao, N., Li, D., and Li, Y. Mesoscale simulation of deformed austenite decomposition into ferrite by coupling a cellular automaton method with a crystal plasticity finite element model. *Acta materialia*, 53(4):991–1003, 2005.

Laplanche, G., Birk, T., Schneider, S., Frenzel, J., and Eggeler, G. Effect of temperature and texture on the reorientation of martensite variants in niti shape memory alloys. *Acta Materialia*, 127:143–152, 2017.

Lee, M., Lim, H., Adams, B., Hirth, J., and Wagoner, R. A dislocation density-based single crystal constitutive equation. *International Journal of Plasticity*, 26(7):925–938, 2010.

Li, H., Yang, H., and Sun, Z. A robust integration algorithm for implementing rate dependent crystal plasticity into explicit finite element method. *International Journal of Plasticity*, 24(2):267–288, 2008.

Lim, T. and McDowell, D. Cyclic thermomechanical behavior of a polycrystalline pseudoelastic shape memory alloy. *Journal of the Mechanics and Physics of Solids*, 50(3):651–676, 2002.

Maletta, C., Sgambitterra, E., Furgiuele, F., Casati, R., and Tuissi, A. Fatigue of pseudoelastic niti within the stress-induced transformation regime: a modified coffin–manson approach. *Smart materials and structures*, 21(11):112001, 2012.

Manchiraju, S. and Anderson, P. M. Coupling between martensitic phase transformations and plasticity: a microstructure-based finite element model. *International Journal of Plasticity*, 26(10):1508–1526, 2010.

Mao, S., Luo, J., Zhang, Z., Wu, M., Liu, Y., and Han, X. Ebsd studies of the stress-induced b2–b19{prime} martensitic transformation in niti tubes under uniaxial tension and compression. *Acta Materialia*, 58(9): 3357–3366, 2010.

Matsumoto, O., Miyazaki, S., Otsuka, K., and Tamura, H. Crystallography of martensitic transformation in ti ni single crystals. *Acta Metallurgica*, 35(8):2137–2144, 1987.

McKelvey, A. L. and Ritchie, R. O. On the temperature dependence of the superelastic strength and the prediction of the theoretical uniaxial transformation strain in nitinol. *philosophical Magazine A*, 80(8): 1759–1768, 2000.

Mirzaeifar, R., DesRoches, R., Yavari, A., and Gall, K. A micromechanical analysis of the coupled thermo-mechanical superelastic response of textured and untextured polycrystalline niti shape memory alloys. *Acta materialia*, 61(12):4542–4558, 2013.

Miyazaki, S., Otsuka, K., and Suzuki, Y. Transformation pseudoelasticity and deformation behavior in a ti-50.6 at% ni alloy. *Scripta Metallurgica*, 15(3):287–292, 1981.

Miyazaki, S., Kimura, S., Otsuka, K., and Suzuki, Y. The habit plane and transformation strains associated with the martensitic transformation in ti-ni single crystals. *Scripta metallurgica*, 18(9):883–888, 1984.

Miyazaki, S., Imai, T., Igo, Y., and Otsuka, K. Effect of cyclic deformation on the pseudoelasticity characteristics of ti-ni alloys. *Metallurgical transactions A*, 17(1):115–120, 1986.

Mohammed, A. S. K. and Sehitoglu, H. Martensitic twin boundary migration as a source of irreversible slip in shape memory alloys. *Acta Materialia*, 186:50–67, 2020a.

Mohammed, A. S. K. and Sehitoglu, H. Modeling the interface structure of type ii twin boundary in b19′ niti from an atomistic and topological standpoint. *Acta Materialia*, 183:93–109, 2020b.

Mohammed, A. S. K. and Sehitoglu, H. Strain-sensitive topological evolution of twin interfaces. *Acta Materialia*, 208:116716, 2021.

Morin, C., Moumni, Z., and Zaki, W. Thermomechanical coupling in shape memory alloys under cyclic loadings: experimental analysis and constitutive modeling. *International Journal of Plasticity*, 27(12):

1959–1980, 2011.

Moumni, Z., Van Herpen, A., and Riberty, P. Fatigue analysis of shape memory alloys: energy approach. *Smart Materials and Structures*, 14(5):S287, 2005.

Moumni, Z., Zaki, W., and Nguyen, Q. S. Theoretical and numerical modeling of solid–solid phase change: application to the description of the thermomechanical behavior of shape memory alloys. *International Journal of Plasticity*, 24(4):614–645, 2008.

Niendorf, T., Lackmann, J., Gorny, B., and Maier, H. In situ characterization of martensite variant formation in nickel–titanium shape memory alloy under biaxial loading. *Scripta Materialia*, 65(10):915–918, 2011.

Nishida, M., Ii, S., Kitamura, K., Furukawa, T., Chiba, A., Hara, T., and Hiraga, K. New deformation twinning mode of b19 {prime} martensite in ti-ni shape memory alloy. *Scripta materialia*, 39(12), 1998.

Norfleet, D., Sarosi, P., Manchiraju, S., Wagner, M.-X., Uchic, M., Anderson, P., and Mills, M. Transformation-induced plasticity during pseudoelastic deformation in ni–ti microcrystals. *Acta Materialia*, 57(12):3549–3561, 2009.

Otsuka, K. and Ren, X. Physical metallurgy of ti–ni-based shape memory alloys. *Progress in materials science*, 50(5):511–678, 2005.

Paranjape, H. M., Manchiraju, S., and Anderson, P. M. A phase field–finite element approach to model the interaction between phase transformations and plasticity in shape memory alloys. *International Journal of Plasticity*, 80:1–18, 2016.

Paranjape, H. M., Bowers, M. L., Mills, M. J., and Anderson, P. M. Mechanisms for phase transformation induced slip in shape memory alloy micro-crystals. *Acta Materialia*, 132:444–454, 2017.

Paranjape, H. M., Paul, P. P., Amin-Ahmadi, B., Sharma, H., Dale, D., Ko, J. P., Chumlyakov, Y. I., Brinson, L. C., and Stebner, A. P. In situ, 3d characterization of the deformation mechanics of a superelastic niti shape memory alloy single crystal under multiscale constraint. *Acta Materialia*, 144: 748–757, 2018.

Peirce, D., Asaro, R., and Needleman, A. An analysis of nonuniform and localized deformation in ductile single crystals. *Acta metallurgica*, 30(6):1087–1119, 1982.

Pelton, A. Nitinol fatigue: a review of microstructures and mechanisms. *Journal of Materials Engineering and Performance*, 20(4):613–617, 2011.

Pelton, A., Huang, G., Moine, P., and Sinclair, R. Effects of thermal cycling on microstructure and properties in nitinol. *Materials Science and Engineering: A*, 532:130–138, 2012.

Petrini, L. and Bertini, A. A three-dimensional phenomenological model describing cyclic behavior of shape memory alloys. *International Journal of Plasticity*, 125:348–373, 2020.

Petrini, L. and Migliavacca, F. Biomedical applications of shape memory alloys. *Journal of Metallurgy*, 2011, 2011.

Polatidis, E., Zotov, N., Bischoff, E., and Mittemeijer, E. J. The effect of cyclic tensile loading on the stress-induced transformation mechanism in superelastic niti alloys: an in-situ x-ray diffraction study. *Scripta Materialia*, 100:59–62, 2015.

Rahim, M., Frenzel, J., Frotscher, M., Pfetzing-Micklich, J., Steegmüller, R., Wohlschlögel, M., Mughrabi, H., and Eggeler, G. Impurity levels and fatigue lives of pseudoelastic niti shape memory alloys. *Acta Materialia*, 61(10):3667–3686, 2013.

Richards, A. W., Lebensohn, R., and Bhattacharya, K. Interplay of martensitic phase transformation and plastic slip in polycrystals. *Acta Materialia*, 61(12):4384–4397, 2013.

Roters, F., Eisenlohr, P., Hantcherli, L., Tjahjanto, D. D., Bieler, T. R., and Raabe, D. Overview of constitutive laws, kinematics, homogenization and multiscale methods in crystal plasticity finite-element modeling: Theory, experiments, applications. *Acta Materialia*, 58(4):1152–1211, 2010.

Salem, A., Kalidindi, S., and Semiatin, S. Strain hardening due to deformation twinning in α-titanium: Constitutive relations and crystal-plasticity modeling. *Acta Materialia*, 53(12):3495–3502, 2005.

Sedmák, P., Šittner, P., Pilch, J., and Curfs, C. Instability of cyclic superelastic deformation of niti investigated by synchrotron x-ray diffraction. *Acta Materialia*, 94:257–270, 2015.

Sehitoglu, H., Jun, J., Zhang, X., Karaman, I., Chumlyakov, Y., Maier, H., and Gall, K. Shape memory and pseudoelastic behavior of 51.5% ni–ti single crystals in solutionized and overaged state. *Acta Materialia*, 49(17):3609–3620, 2001a.

Sehitoglu, H., Karaman, I., Anderson, R., Zhang, X., Gall, K., Maier, H., and Chumlyakov, Y. Compressive response of niti single crystals. *Acta Materialia*, 48(13):3311–3326, 2000.

Sehitoglu, H., Anderson, R., Karaman, I., Gall, K., and Chumlyakov, Y. Cyclic deformation behavior of single crystal niti. *Materials Science and Engineering: A*, 314(1-2):67–74, 2001b.

Shaw, J. A. and Kyriakides, S. Thermomechanical aspects of niti. *Journal of the Mechanics and Physics of Solids*, 43(8):1243–1281, 1995.

Simon, T., Kröger, A., Somsen, C., Dlouhy, A., and Eggeler, G. On the multiplication of dislocations during martensitic transformations in niti shape memory alloys. *Acta Materialia*, 58(5):1850–1860, 2010.

Song, D., Kang, G., Kan, Q., Yu, C., and Zhang, C. Damage-based life prediction model for uniaxial low-cycle stress fatigue of super-elastic niti shape memory alloy microtubes. *Smart Materials and Structures*, 24(8):085007, 2015.

Staroselsky, A. and Anand, L. Inelastic deformation of polycrystalline face centered cubic materials by slip and twinning. *Journal of the Mechanics and Physics of Solids*, 46(4):671–696, 1998.

Taleb, L. and Sidoroff, F. A micromechanical modeling of the greenwood–johnson mechanism in transformation induced plasticity. *International Journal of Plasticity*, 19(10):1821–1842, 2003.

Thamburaja, P. Constitutive equations for martensitic reorientation and detwinning in shape-memory alloys.

Journal of the Mechanics and Physics of Solids, 53(4):825–856, 2005.

Thamburaja, P. and Anand, L. Polycrystalline shape-memory materials: effect of crystallographic texture. *Journal of the Mechanics and Physics of Solids*, 49(4):709–737, 2001.

Van Humbeeck, J. and Delaey, L. The influence of strain-rate, amplitude and temperature on the hysteresis of a pseudoelastic cu-zn-al single crystal. *Le Journal de Physique Colloques*, 42(C5):C5–1007, 1981.

Wan, V., MacLachlan, D., and Dunne, F. A stored energy criterion for fatigue crack nucleation in polycrystals. *International Journal of Fatigue*, 68:90–102, 2014.

Wang, J., Moumni, Z., and Zhang, W. A thermomechanically coupled finite-strain constitutive model for cyclic pseudoelasticity of polycrystalline shape memory alloys. *International Journal of Plasticity*, 97: 194–221, 2017.

Wang, X., Xu, B., and Yue, Z. Phase transformation behavior of pseudoelastic niti shape memory alloys under large strain. *Journal of Alloys and Compounds*, 463(1-2):417–422, 2008a.

Wang, X., Xu, B., and Yue, Z. Micromechanical modelling of the effect of plastic deformation on the mechanical behaviour in pseudoelastic shape memory alloys. *International Journal of Plasticity*, 24(8): 1307–1332, 2008b.

Warren, J. and Wei, D. A microscopic stored energy approach to generalize fatigue life stress ratios. *International Journal of Fatigue*, 32(11):1853–1861, 2010.

Xiao, Y., Zeng, P., and Lei, L. Micromechanical modeling on thermomechanical coupling of cyclically deformed superelastic niti shape memory alloy. *International Journal of Plasticity*, 107:164–188, 2018.

Xie, X., Kang, G., Kan, Q., Yu, C., and Peng, Q. Phase field modeling to transformation induced plasticity in super-elastic niti shape memory alloy single crystal. *Modelling and Simulation in Materials Science and Engineering*, 27(4):045001, 2019.

Xie, X., Kang, G., Kan, Q., and Yu, C. Phase-field theory based finite element simulation on thermomechanical cyclic deformation of polycrystalline super-elastic niti shape memory alloy. *Computational Materials Science*, 184:109899, 2020.

Xu, B., Yu, C., and Kang, G. Phase field study on the microscopic mechanism of grain size dependent cyclic degradation of super-elasticity and shape memory effect in nano-polycrystalline niti alloys. *International Journal of Plasticity*, 145:103075, 2021.

Yin, H. and Sun, Q. Temperature variation in niti shape memory alloy during cyclic phase transition. *Journal of materials engineering and performance*, 21(12):2505–2508, 2012.

Yin, H., He, Y., and Sun, Q. Effect of deformation frequency on temperature and stress oscillations in cyclic phase transition of niti shape memory alloy. *Journal of the Mechanics and Physics of Solids*, 67:100–128, 2014.

Yu, C., Kang, G., Song, D., and Kan, Q. Micromechanical constitutive model considering plasticity for

super-elastic niti shape memory alloy. *Computational Materials Science*, 56:1–5, 2012.

Yu, C., Kang, G., Kan, Q., and Song, D. A micromechanical constitutive model based on crystal plasticity for thermo-mechanical cyclic deformation of niti shape memory alloys. *International Journal of Plasticity*, 44:161–191, 2013.

Yu, C., Kang, G., and Kan, Q. Crystal plasticity based constitutive model of niti shape memory alloy considering different mechanisms of inelastic deformation. *International Journal of Plasticity*, 54:132–162, 2014a.

Yu, C., Kang, G., and Kan, Q. A physical mechanism based constitutive model for temperature-dependent transformation ratchetting of niti shape memory alloy: One-dimensional model. *Mechanics of Materials*, 78:1–10, 2014b.

Yu, C., Kang, G., and Kan, Q. Study on the rate-dependent cyclic deformation of super-elastic niti shape memory alloy based on a new crystal plasticity constitutive model. *International Journal of Solids and Structures*, 51(25-26):4386–4405, 2014c.

Yu, C., Kang, G., and Kan, Q. A micromechanical constitutive model for anisotropic cyclic deformation of super-elastic niti shape memory alloy single crystals. *Journal of the Mechanics and Physics of Solids*, 82: 97–136, 2015a.

Yu, C., Kang, G., Kan, Q., and Zhu, Y. Rate-dependent cyclic deformation of super-elastic niti shape memory alloy: thermo-mechanical coupled and physical mechanism-based constitutive model. *International Journal of Plasticity*, 72:60–90, 2015b.

Yu, C., Kang, G., Song, D., and Kan, Q. Effect of martensite reorientation and reorientation-induced plasticity on multiaxial transformation ratchetting of super-elastic niti shape memory alloy: new consideration in constitutive model. *International Journal of Plasticity*, 67:69–101, 2015c.

Yu, C., Kang, G., and Kan, Q. A micromechanical constitutive model for grain size dependent thermo-mechanically coupled inelastic deformation of super-elastic niti shape memory alloy. *International Journal of Plasticity*, 105:99–127, 2018.

Zaki, W. and Moumni, Z. A 3d model of the cyclic thermomechanical behavior of shape memory alloys. *Journal of the Mechanics and Physics of Solids*, 55(11):2427–2454, 2007.

Zhang, Y., Zhu, J., Moumni, Z., Van Herpen, A., and Zhang, W. Energy-based fatigue model for shape memory alloys including thermomechanical coupling. *Smart Materials and Structures*, 25(3):035042, 2016.

Zhang, Y., You, Y., Moumni, Z., Anlas, G., Zhu, J., and Zhang, W. Experimental and theoretical investigation of the frequency effect on low cycle fatigue of shape memory alloys. *International Journal of Plasticity*, 90:1–30, 2017.

Zhang, Y., Li, W., Moumni, Z., Zhu, J., Zhang, W., and Zhong, S.-Y. Degradation of the recoverable strain during stress controlled full transformation cycling in niti shape memory alloys. *Scripta Materialia*, 162:

68–71, 2019a.

Zhang, Y., Moumni, Z., You, Y., Zhang, W., Zhu, J., and Anlas, G. Multiscale trip-based investigation of low-cycle fatigue of polycrystalline niti shape memory alloys. *International Journal of Plasticity*, 115: 307–329, 2019b.

Zhang, Y., You, Y., Moumni, Z., Anlas, G., Zhu, J., and Zhang, W. Stored-energy-based fatigue criterion for shape memory alloys. *Smart Materials and Structures*, 28(6):065027, 2019c.

Zheng, L., He, Y., and Moumni, Z. Investigation on fatigue behaviors of niti polycrystalline strips under stress-controlled tension via in-situ macro-band observation. *International Journal of Plasticity*, 90:116–145, 2017.

Zotov, N., Pfund, M., Polatidis, E., Mark, A. F., and Mittemeijer, E. J. Change of transformation mechanism during pseudoelastic cycling of niti shape memory alloys. *Materials Science and Engineering: A*, 682: 178–191, 2017.

Highlights

September 20, 2021

1. A crystal plasticity-based constitutive model which, for the first time in the literature, takes into account all physical mechanisms liable to impact the fatigue behavior of pseudoelastic SMA is developed.

2. Characteristics related with monocyclic deformation of single crystal NiTi SMA are addressed within the finite strain framework and the numerical implementation is performed in CAST3M (2019) finite element software.

3. The model is generalized to predict the large cyclic deformation of NiTi SMAs.

4. The model is able to qualitatively capture all the features associated with pseudoelastic NiTi SMA.

5. The model is quantitatively validated against the experimental mechanical responses reported in the literature.

AUTHORSHIP STATEMENT

Manuscript title: A multi-physics, multi-scale and finite strain crystal plasticity-based model for pseudoelastic NiTi shape memory alloy

Conception and design of study: Ziad Moumni, Xiaofei JU
Acquisition of data: Xiaofei Ju, Fengguo Zhang, Zhe Chen
Analysis and interpretation of data: Xiaofei Ju, Ziad Moumni, Yahui Zhang

Drafting the manuscript: Xiaofei Ju, Ziad Moumni, Yahui Zhang
Revising the manuscript critically for important intellectual content: Ziad Moumni, Yahui Zhang, Jihong Zhu, Weihong Zhang

Approval of the version of the manuscript to be published : Xiaofei Ju, Ziad Moumni, Yahui Zhang, Fengguo Zhang , Jihong Zhu, , Zhe Chen and Weihong Zhang

Signature of the corresponding author on behalf of all the authors
Ziad Moumni

Z.Moumni

21/09/2021

Declaration of interests

The authors declare that they have no known competing financial interests or personal relationships that could have appeared to influence the work reported in this paper.